

A SPIN ON COOPERATIVITY

HIGH-RESOLUTION RHEO-MRI OF STRUCTURED FLUIDS



KLAUDIA MILC

Propositions

1. Flow cooperativity causes microstructural changes in thixotropic fluids.
(this thesis)
2. Implementation of stress measurements in rheo-MRI setups is necessary to improve accuracy in the quantification of cooperativity lengths.
(this thesis)
3. Investment of time and money into the development of predominantly high-field medical MRI scanners limits the progress of medical MRI.
4. The practice of publishing predominantly positive results leads to additional build-up of stress in academia.
5. Promoting co-living among all age groups is a solution to loneliness and the housing shortage.
6. Disruptive civil disobedience actions are necessary to achieve climate justice.

Propositions belonging to the thesis, entitled

A spin on cooperativity: high-resolution rheo-MRI of structured fluids

Klaudia Milc, Wageningen, 8 December 2023

A spin on cooperativity

High-resolution rheo-MRI of structured fluids

Klaudia Milc

Thesis committee**Promotor:**

Prof. Dr J. P. M. van Duynhoven
Special Professor, Magnetic Resonance in Relation to Food
Wageningen University & Research

Co-promotors:

Dr C. Terenzi
Assistant professor, Biophysics
Wageningen University & Research

Dr J. A. Dijkman
Associate professor, Physical Chemistry & Soft Matter
Wageningen University & Research
Van der Waals-Zeeman Institute
University of Amsterdam

Other members:

Dr L. Sagis, Wageningen University & Research
Prof. Dr A. Sederman, University of Cambridge, United Kingdom
Dr G. Ovarlez, Université de Bordeaux, France
Dr L. Pel, Eindhoven University of Technology

This research was conducted under the auspices of VLAG Graduate School (Biobased, Biomolecular, Chemical, Food, and Nutrition Sciences)

A spin on cooperativity

High-resolution rheo-MRI of structured fluids

Klaudia Milc

Thesis

submitted in fulfilment of the requirements for the degree of doctor

at Wageningen University

by the authority of the Rector Magnificus,

Prof. Dr A.P.J. Mol,

in the presence of the

Thesis Committee appointed by the Academic Board

to be defended in public

on Friday 8 December 2023

at 4 p.m. in Omnia

Klaudia Milc

A spin on cooperativity: high resolution rheo-MRI of structured fluids

174 pages

PhD thesis, Wageningen University, Wageningen, the Netherlands (2023)

With references, with summaries in English and Polish

ISBN: 978-94-6447-925-6

DOI: <https://doi.org/10.18174/639936>

Contents

	Page
Chapter 1	7
Introduction	
Chapter 2	37
Validation of temperature-controlled rheo-MRI measurements in a sub-mm gap Couette geometry	
Chapter 3	57
Quantifying cooperative flow of fat crystal dispersions	
Chapter 4	83
Capillary flow-MRI: quantifying micron-scale cooperativity in complex dispersions	
Chapter 5	109
Herschel-Bulkley flow of micronized fat crystal dispersions: effect of shear history	
Chapter 6	131
General discussion	
Chapter 7	157
Summary	
Acknowledgements, about the author, list of publications	165

CHAPTER

1

Introduction



1.1. Flow of simple and complex fluids

Flow of fluids through confinements of various sizes is all around us, and lies at the basis of many fundamental research experiments and industrial processes. For instance, in soft matter studies, flow occurs in microfluidic devices during production of foams and emulsions with bubbles and droplets of well-defined polydispersity¹ or during studies of inter-particle interactions in particulate fluids.² In typical bulk rheology measurements, fluids flow in geometries with gap sizes within a sub-mm range³ whereas, when mimicking industrial processes, such as plant-based meat analogue production, geometries with larger flow gap sizes are used.⁴ In industrial processing and customer use of foods, cosmetics or paints, fluids such as emulsions, gels, and fat dispersions are pumped through pipes during manufacturing or are spread into μm -scale layers. As another important example, in the oil industry, crude oils flow through rock pores of varying sizes and, thereafter, are transported via pipelines under varying conditions of temperature and pressure.⁵

To correctly interpret and understand the results of bulk rheology, and to ensure good control over the industrial processes and rational design of commercial products, the flow behavior of the involved fluids and the related governing mechanisms must be well understood. This task is relatively easy for simple, Newtonian fluids such as dilute solutions. However, for non-Newtonian fluids, often possessing a complex microstructure, flow prediction becomes non-trivial. On the one hand, droplets in emulsions, bubbles in foams or 3D colloidal networks in gels and fat dispersions, give the fluids the desirable physical properties and functionality, such as texture for foods, or good spreadability for paints and cosmetics. On the other hand, the fluids' microstructure can cause temporal and spatial flow instabilities. For instance, emulsions, foams, gels, and fat dispersions are prone to, *e.g.*, shear banding⁶⁻⁸, whereby the fluid flows with distinct apparent viscosities under a given shear rate, and may even exhibit stagnant regions. Additionally, complex fluids often exhibit fluctuating velocities within a thin region adjacent to the confining walls, with magnitudes different from the velocity of the wall itself, a phenomenon known as wall slip.^{9,10} Notably, the link between flow and microstructure is a two-way street for some fluids: flow itself can lead to microstructural changes such as droplet coalescence, recrystallization or network destruction.¹¹

Prediction and understanding of flow in sub-mm confinements, commonly present in rheological measurements, in food or organ 3D printing, or in spreading of paints

into thin coatings, poses additional challenges. In these processes, the size of the flow confinement often exceeds the mean size of the microstructure by up to two orders of magnitude. In such conditions, flow can become cooperative, meaning that the microstructural components of the flowing fluid, such as bubbles or droplets, flow in a collective manner.¹² In such flow regime, flow of particles at one site induces flow in neighboring zones, resulting in local shear rates being dependent not only on local stress values, but also on the gradient of stresses. Flow cooperativity may significantly alter the macroscopic flow behavior of the fluid, resulting in material fluidization, velocity enhancement, and spatially and/or temporally dependent viscosities.^{12,13} However, as the dependence of flow cooperativity on microstructural properties is still not well understood, cooperativity effects currently cannot be predicted and often remain unaccounted for in research involving flow, *e.g.*, global rheological measurements or in industrial applications. One of the underlying reasons is the challenging experimental conditions necessary for studies of cooperativity. As the effects manifest themselves only in strong confinements, experimental setups able to provide access to spatially-resolved flow in sub-mm geometries are needed. To date, most experimental studies have been conducted in microchannels coupled with optical techniques, giving insight into cooperative flow of model, optically-transparent fluids.¹⁴⁻¹⁷ However, these experimental approaches preclude studies of the many soft structured fluids, with intrinsic optically-opaque properties. A powerful alternative technique that does not suffer from such limitation, is Magnetic Resonance Imaging (MRI) velocimetry.¹⁸ So far, however, MRI velocimetry measurements have been possible only in mm-sized flow gaps,^{11,19-22} which are insufficient for imposing strong confinement on most soft particulate fluids with particles in the order of a few μm .^{14,23-26}

The aim of this thesis is two-fold. Firstly, the development of sub-mm rotational and microcapillary rheo-MRI setups is targeted, to enable studies of strongly confined flow in a wide range of fluids using various flow geometries and incorporating temperature-control capability. Secondly, the developed experimental setups are used to study and quantify cooperativity effects in real-life, complex fluids. Finally, gathering the results obtained throughout the thesis work and those so far reported in the literature, an attempt is made to link emerging trends in flow cooperativity with the microstructural properties of the examined complex fluids.

In the subsequent parts of this introduction, the mechanisms governing the flow of simple and complex fluids are described, as a foundation for a detailed description

of cooperativity and current quantification methods (section 1.2). In section 1.3, common velocimetric imaging methods are reviewed, with rheo-MRI emerging as a powerful and versatile technique for studying strongly confined flow in real-life fluids. The current technical limitations of rheo-MRI are identified, as a target for methodological development during this thesis work. Finally, in section 1.4, the complex fluids examined throughout this thesis work to study the cooperativity-microstructure interplay are described.

1.2. Flow behavior of simple and complex fluids

1.2.1. Quantification of global flow

Correctly predicting the flow behavior of a fluid is crucial for aiding the rational design of product formulations and the related processing conditions, including applied pressures and temperatures. Yet, the fluid's response to an application of normal or shear stress can be very diverse, with some fluids (water, honey, milk) flowing homogeneously as soon as any stress is applied and others (whipped cream, hand cream, butter) behaving as solids or exhibiting flow heterogeneities unless subjected to high enough stresses. Rheology, the go-to branch of science for studies of deformation under stress, helps in classifying the fluids according to their flow behavior. In conventional, global rheology this is typically done by imposing a shear rate, $\dot{\gamma}$, on a fluid, and by measuring the resulting shear stress, σ , exerted by the fluid on the rotating element of the flow geometry. By measuring σ under a range of $\dot{\gamma}$ values, the relation between the two can be established in the form of a constitutive equation, and plotted as a global flow curve.³ It should be noted that the knowledge of the constitutive equation for a given fluid does not yield an understanding of the microstructural origin of the observed flow behavior. In Fig. 1.1a flow curves of commonly encountered types of fluids are plotted, with Fig. 1.1b showing the respective viscosities, η , as a function of $\dot{\gamma}$. The simplest flow behavior, with a linear stress response is exhibited by Newtonian fluids, in which case all flow properties can be predicted solely on the basis of η . This contrasts with non-Newtonian fluids, whose η can be a function of multiple parameters including $\dot{\gamma}$ and/or time. A special case of non-Newtonian behavior is presented by yield stress fluids (YSFs), which in fact behave as fluids only if the applied σ exceeds a characteristic threshold stress value, referred to as the yield stress, σ_y . For $\sigma < \sigma_y$ the material has solid-like properties, as η tends to infinity. Whereas the presence of yield stress can be determined relatively easily, accurate quantification, and identification of its

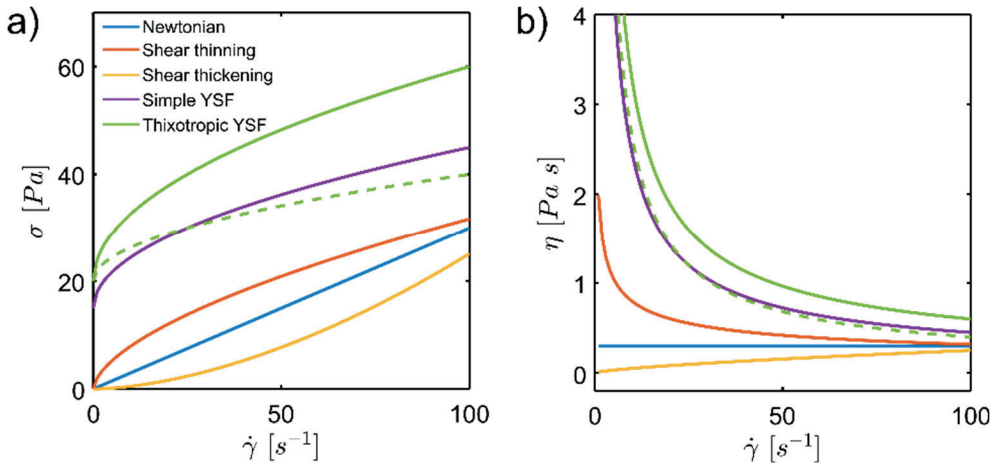


Figure 1.1: Plots of stress (a) and viscosity (b) as a function of the applied shear rate, for fluids with different flow properties. For the thixotropic YSF a ramp-down (solid line) and a ramp-up (dashed line) is shown, with a characteristic hysteresis loop between the two curves.

microstructural origin is much more challenging, and is a subject of continuous research. In general terms, the emergence of yield stress is ascribed to microstructural organization by which a collection of particles loses its ability to flow.²⁷ An example of such dynamical arrest can be observed in concentrated emulsions, where jammed droplets are trapped by their neighbors. As a result, under conditions of $\sigma < \sigma_y$, an elastic deformation is observed. Most emulsions belong to a group of simple YSFs, with constant σ_y and η dependent only on the shear rate. On the other hand, for thixotropic YSFs, η is dependent not only on $\dot{\gamma}$, but also on shear history, as imposed flow conditions lead to reversible modifications of the microstructure, such as network destruction.^{20,28}

The solid-/liquid-like rheological properties of simple and thixotropic YSFs may be desirable in formulation and manufacturing of commercial products, as such fluids can flow, *e.g.*, during transportation in pipes and also hold specific 3D shapes after extrusion. However, YSFs, especially with thixotropic properties have a notoriously complex flow behavior, as the solid and liquid phases can coexist within flow geometries with spatially inhomogeneous stresses, such as in pipes or capillaries. This can lead to clogging or phase separation, compromising production efficiency in an industrial setting. It can also result in an incorrect interpretation of experimental results, if, as commonly done, homogeneous flow is assumed. This can in some cases be prevented by reliably predicting the flow behavior, allowing for the choice of

suitable flow geometries or applied pressures. One of the models commonly used for describing and predicting the flow of YSFs is the Herschel-Bulkley (HB) model:

$$\sigma = \sigma_y + K\dot{\gamma}^n, \quad (1.1)$$

where K is a proportionality constant with the units of $\text{Pa} \cdot \text{s}^{1/n}$ and n is a dimensionless power law index.²⁹ The HB model can successfully capture and predict the macroscopic flow behavior of simple YSFs. However, due to its phenomenological character, its application to modelling the flow of thixotropic YSFs is limited. The limitation has triggered the development of dedicated models, with the simplest example being a modification of the HB equation:

$$\sigma = \sigma_y(\lambda) + \eta(\lambda)\dot{\gamma}, \quad (1.2)$$

where both σ_y and η are a function of a structure parameter, λ , defined as a measure of the degree of bonding or aggregation within the structure.^{30,31} The evolution of the microstructure is thus captured by $d\lambda/dt$, described by a kinetic equation, with contributions from the rates of structure formation and degradation. The model has been used to capture the thixotropic flow behavior of, *e.g.*, extensively stirred Carbopol²⁸ and acid milk microgels.³² Other, more elaborate models are available, which can account for multiple structural parameters, viscoelasticity or ageing.³³

1.2.2. Local flow and cooperativity

Both HB and thixotropic models describe the flow of YSFs from the macroscopic, phenomenological perspective, providing no insight into how flow occurs at the microscopic level. Understanding of the latter becomes an important requirement if deviations of the experimental results from theoretical predictions are observed. Significant efforts have thus been made to elucidate the way in which the microstructure responds locally to applied stresses below and above the yield stress. One of the approaches which has proven successful in modelling the flow of YSFs is based on the Soft Glassy Rheology (SGR) model.³⁴ According to this framework, applied shear leads to a buildup of stress within the microstructure, which can undergo a reversible elastic deformation or an irreversible plastic rearrangement, the latter occurring once the local value of stress overcomes the microscopic yield stress.³⁴⁻³⁷ It has thus been shown that such irreversible microstructural displacements are a key mechanism of flow in YSFs, with macroscopic flow occurring

only if sufficient number of plastic rearrangements happen. Importantly, such flow mechanism intrinsically introduces spatial flow inhomogeneities as the spatial rearrangements are not uniformly distributed within the fluid.

Surprisingly, in conditions of strong flow confinement where the size of the flow gap is not more than 10^2 times larger than the characteristic size of the fluid's microstructure, flow can be observed even under stress values below the yield stress of the material. It is currently believed that this effect is caused by the non-local, cooperative character of the plastic rearrangements. In strongly confined flow, plastic rearrangements in a flowing region can induce long-ranged stress modulations over a finite distance, creating zones where further rearrangements are more likely to happen (Fig. 1.2a). In such a way, local plastic events fluidize the material over a distance on the order of magnitude of the flow gap size resulting, microscopically, in the suppression of the local yield stress and, macroscopically, in enhanced velocities and inhomogeneous viscosities (Fig. 1.2b).

Cooperativity as the mechanism governing strongly confined flow of soft particulate fluids has been first demonstrated in concentrated emulsions by Goyon *et al.*^{12,15} Since then, flow cooperativity has been studied in a range of materials and

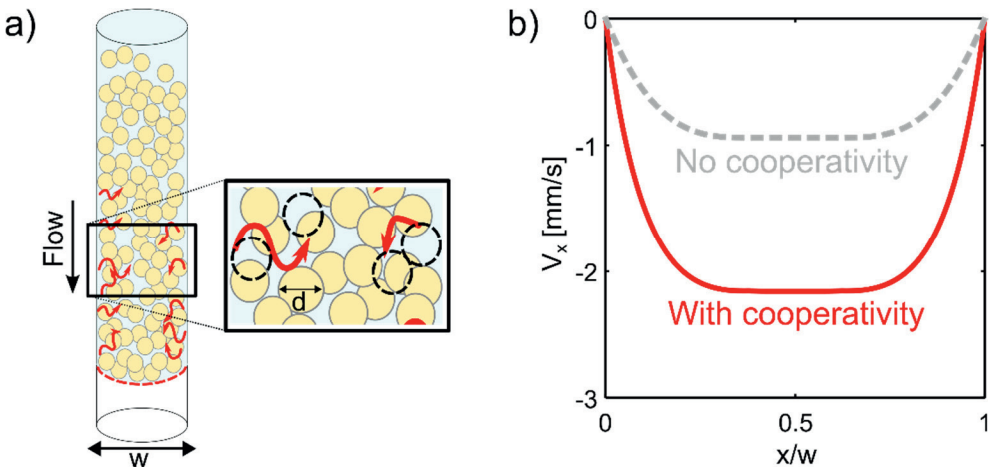


Figure 1.2: a) Schematic representation of flow cooperativity for a particulate fluid with a characteristic microstructural length, d , flowing in a microcapillary with diameter w . The fluid is strongly confined, such that $w \leq 10^2 \cdot d$. Red arrows and dashed circles represent the stress redistribution and plastic rearrangements, respectively. b) Calculated velocity profiles as a function of the normalized radial position, x , for flow in a capillary in the presence (red line) or absence (grey dashed line) of cooperativity.

geometries, including confined flow of concentrated emulsions in microchannels with controlled surface roughness,^{38,39} polymer microgels,^{14,40} acid milk gels,³² citrus fiber cellulose dispersions^{13,24} and granular materials such as sand and mustard seeds.⁴¹⁻⁴³ Authors of these studies found that strong confinement itself might be insufficient to trigger flow cooperativity, and that particle concentration and anisotropy, as well as wall roughness, constitute equally important factors. Importantly, the presence of cooperativity effects in such a broad range of materials with distinct microstructural properties suggests an underlying universal effect.

1.2.3. Modelling and quantification of flow cooperativity

The discovery of cooperative flow triggered the development of theoretical frameworks, including the microscopic origin of flow in YSFs and its intrinsic spatial heterogeneity. Examples of such models include SGR developed by Sollich *et al.*,^{34,44} Shear Transformation Zones proposed by Falk *et al.*,⁴⁵ the non-local model by Pouliquen *et al.*,⁴⁶ and the fluidity model by Bocquet *et al.*⁴⁷ Detailed description of each approach is beyond the scope of this thesis. The underlying common characteristic between all the models is the dependence of local flow not only on local stresses, but also on the gradient of stresses, *i.e.* on flow in the neighboring zones. Aside from these gradient-based approaches, other numerical models have also proven successful in their ability to predict flow fields in strongly confined flowing fluids, including the lattice Boltzmann methods.^{2,48,49}

Fluidity model. Out of all the aforementioned modelling approaches, one that lends itself particularly well to a comparison with experimental data is the fluidity model, based on the microscopic approach of the kinetic elastoplastic (KEP) model.⁴⁷ The model is based on the concept of fluidity, defined as the local rate of plastic rearrangements. On a macroscopic scale, fluidity is the ratio between shear rate and shear stress, namely $f = \dot{\gamma}/\sigma$, and has the units of inverse viscosity. For non-confined flow, where the local behavior is dictated solely by the local shear rates and stresses, fluidity takes up its bulk definition, according to:

$$f_{bulk} = \dot{\gamma}_{bulk}(x) / \sigma(x), \quad (1.3)$$

where $\dot{\gamma}_{bulk}$ is the shear rate exhibited by the sample, governed by the constitutive equation. In contrast, for strongly confined flow, the local fluidity, $f(x)$ is predicted to also depend on the spatial gradients of stresses and shear rates, as the local flow

is coupled to flow at the neighboring sites via cooperativity. As such, $f(x)$ deviates from its bulk value according to a diffusion equation of the form:

$$f(x) = f_{bulk} + \xi^2 \frac{\partial^2 f(x)}{\partial x^2}, \quad (1.4)$$

where ξ is the cooperativity length, defining the distance over which plastic events influence the neighboring particles.^{12,15} The introduction of this characteristic length scale ξ effectively makes the model sensitive to the finite size of the microstructure, despite its phenomenological character. The quantity ξ can be obtained by fitting spatially-resolved velocimetry data with the solution of Eq. 1.4 for specific flow conditions accounting for, *e.g.*, geometry shape or stress distribution.

The solution of Eq. 1.4 requires two boundary conditions (BCs), the form of which depends on the flow geometry.^{13,15,42} For geometries with symmetrical flow fields, such as rectangular or cylindrical microcapillaries, the first BC can be derived from the symmetry condition, *i.e.* $\partial f / \partial x = 0$, while the second BC is determined by the fluidity at the walls, f_w . For geometries with non-symmetrical flow fields, such as a Couette cell (CC), cone-plate (CP) or more complex geometries with, *e.g.*, patterned surfaces, BCs are derived from f_w at both confining walls. Notably, the quantification of cooperativity lengths with the fluidity model requires the knowledge of bulk flow properties to reliably calculate f_{bulk} . This is often a non-trivial task, especially for real-life YSFs with thixotropic properties.^{28,50} In this case, the simplest form of Eq. 1.4 where f_{bulk} is derived from the HB model should be modified to take into account the rich dynamics of thixotropic YSFs.^{8,32}

An interesting evidence that emerged in experimental and theoretical studies of flow cooperativity is the dependence of ξ on stress. Many theoretical frameworks, including KEP and related models for granular materials,^{41,51} predict that ξ depends on the distance of the applied stress to the yield stress, and is commonly defined as:

$$\xi(\sigma) = \frac{m}{\sqrt{|\sigma - \sigma_y|}} d, \quad (1.5)$$

where m is a dimensionless constant defined as the non-local amplitude, characterizing flow cooperativity. Yet, majority of experimental studies model the

data with stress-independent ξ , despite the presence of significant stress variation in commonly used flow geometries.^{15,40}

1.3. Experimental setups for studies of strongly confined flow

For quantification of cooperativity effects, experimental methods able to access spatially-resolved flow information in strong confinements are needed. As a result of the former requirement, conventional rheology becomes unsuitable, because it provides only global flow information and assumes uniform flow of the sample. Despite the availability of a range of methods able to probe local flow behavior, currently none of them is well suited for studies of cooperativity in both model and real-life materials. The list below summarizes the requirements for velocimetric techniques and its coupled flow geometry, for studies of flow cooperativity.

Velocimetric technique:

- **Access to local flow information in optically-opaque fluids**, necessary to study cooperativity effects in real-life, soft structured materials, most of which possess inherently strongly scattering properties.
- **Access to local velocities with spatial resolution of at least 10% of the gap size**, necessary for reliable quantification of ξ with the fluidity model.

Coupled flow geometry:

- **Possibility to scale the confinement size within sub-mm range**, which is the strongly-confined flow regime for complex dispersions with particle sizes in the range sub- μm to tens of μm .
- **Possibility to modify wall surface properties**, important to understand the relationship between ξ , surface roughness, and wall slip.

The methods most commonly used for velocimetry studies include Particle Imaging Velocimetry (PIV),⁵² rotational rheo-MRI,¹⁸ rheo-ultrasound velocity profiling (rheo-UVP),^{53,54} and Optical Coherence Tomography (OCT).^{55,56} In Table 1.1, these methods are compared with respect to the outlined properties, in addition to the overarching requirement of spatially-resolved velocity information. Regarding the access to sufficient spatial resolution, approximate values for each technique are listed, with the theoretical, smallest attainable confinement size included, assuming a minimum of 10 pixels across the flow gap. Global rheology, despite not being a velocimetric technique, is also included in the comparison as reference for flow studies.

Table 1.1: Comparison of the available experimental methods for studies of flow in complex fluids, in terms of the necessary characteristics for studies of cooperativity. The colors of the cells classify the method as suitable (green), unsuitable (red) or limited (orange), with respect to the criterion. For the latter, the explanation of the limitation is provided. For global rheology, the prerequisite of providing access to local flow is not met, hence consideration of the remaining categories is not applicable (grey). Assuming a requirement of at least 10 pixels across the flow gap, and given the available spatial resolutions, indicative smallest attainable confinement size, w_{min} is listed.

Method	Velocimetry measurements				Coupled flow geometry	
	Access to local flow information	Suitability for optically-opaque fluids	Res. [$\mu\text{m}/\text{pixel}$]	w_{min} [μm]	Possibility to scale the confinement size within sub-mm range	Possibility to modify surface properties
Global rheology						
PIV			1	10		
Rotational rheo-MRI			5-10	50 – 100	Only in CP; in CCs, limited to ≥ 0.5 mm due to the challenge in aligning the concentric cylinders	Only using MRI compatible materials
Rheo-UVP	Only 1D profile of vel. perpendicular to the walls	May require tracer particles	10	100	Fluid-wall interface can cause disturbances	
OCT	Only 1D profile of vel. perpendicular to the walls	Penetration depth depends on the sample	3	30		

So far, PIV has been the most suitable technique for studies of flow cooperativity, as reflected in the prevalence of this technique in literature studies within the field. The main advantages offered by PIV are the availability of scalable flow geometries and high spatial resolution, enabling studies of flow in confinement sizes down to ~ 10 μm . However, the method is inherently limited to optically-transparent fluids and, thus far, has only been used for studies of cooperativity in transparent gels and model emulsions.^{14,15,17} Among the other potential techniques, rotational rheo-MRI stands out as the most versatile technique without inherent limitations in terms of applicability to studies of cooperativity. MRI enables measurements of flow in up to three spatial dimensions, without limitations on the direction of the main velocity component. Additionally, it gives access to the local chemical composition of the fluid and other fluids' properties, as discussed in details in the following section. Notably, both rheo-UVP and OCT have also been successfully used in studies of local flow behavior in optically-opaque materials. Hence, they could both be considered as potential complementary techniques for cooperativity studies.⁵⁷ In particular, OCT, despite its limitation on the penetration depth in some materials, is able to provide high-resolution velocimetry data within regions close to the walls, which could be helpful in understanding wall fluidity and cooperativity effects triggered by wall roughness.⁵⁵

1.3.1. Rotational rheo-MRI velocimetry

Thanks to the versatility of MRI velocimetry, a step forward in studies of cooperativity in optically-opaque, real-life fluids has already been made using rotational rheo-MRI.¹⁸ However, the current technical limitations of the latter technique, outlined in Table 1.1, restrict its applicability to materials with mm-sized particles. Before diving into the details of the rotational rheo-MRI setup and the origin of its technical limitations, the principles behind MRI velocimetry are briefly outlined. In the following sections vectorial quantities are marked with bold font.

Principles of Nuclear Magnetic Resonance (NMR) and MRI-velocimetry. MRI is based on the ability of nuclei with non-null magnetic moment vector to interact with an applied external magnetic field, \mathbf{B}_0 . Out of all the NMR-active nuclei, most MRI applications, including the work of this thesis, are based on the nuclei of ^1H , as they are highly abundant, present in most materials, and have relatively simple NMR properties.⁵⁸

The NMR phenomenon is based on the tendency of the magnetic dipole moment vector of the ^1H nuclei to align itself with \mathbf{B}_0 . The sum of all the individual,

microscopic magnetic moments is referred to as the net longitudinal equilibrium magnetization, \mathbf{M}_0 , which can be manipulated via short radiofrequency (r.f.) pulses carefully arranged in a so-called NMR pulse sequence.⁵⁹ In the simplest experiment, a 90° r.f. pulse rotates \mathbf{M}_0 away from the equilibrium, by convention along a z – axis, towards the transverse x – y plane. The magnetization vector starts precessing around the \mathbf{B}_0 field with a Larmor frequency, according to $\omega_0 = \gamma \mathbf{B}_0$, where γ is the nucleus-specific gyromagnetic ratio. The precession is then detected as a magnetic field oscillating at the Larmor frequency. In reality, the precession frequency will not depend simply on \mathbf{B}_0 , but on the effective magnetic field, with additional contributions from magnetic field inhomogeneities and the electron density around the nucleus. The latter gives rise to the chemical shift information, and is the basis of NMR spectroscopy. In MRI, the magnetic field is purposefully made to vary with position, by passing electrical current through so-called gradient coils. The resulting magnetic field becomes spatially-dependent, and varies typically in a linear fashion according to $\mathbf{B}(\mathbf{r}) = \mathbf{B}_0 + \mathbf{G} \cdot \mathbf{r}$, where \mathbf{G} is a vector describing the applied magnetic field gradient, defined as $\partial \mathbf{B} / \partial \mathbf{r}$, and \mathbf{r} is the position of the nuclei in the sample.⁶⁰ Under the action of the applied magnetic field gradients, nuclei begin to precess with position-dependent frequency and acquire a position-dependent phase up to time t :

$$\varphi(\mathbf{r}, t) = \gamma \int_0^t \mathbf{G}(t') \mathbf{r}(t') dt', \quad (1.6)$$

where t' is the duration of the gradient. With the intensity of the signal at position \mathbf{r} being proportional to spin density, $\rho(\mathbf{r})$, the detected complex time-domain signal can be thus described as:

$$S(t) = \int \rho(\mathbf{r}) \exp(-i\varphi(\mathbf{r}, t)) d\mathbf{r}. \quad (1.7)$$

In MRI experiments the signal is acquired as a function of the so-called k -space, defined as $\mathbf{k}(t) = \gamma / 2\pi \int_0^t \mathbf{G}(t') dt'$, which gives:

$$S(\mathbf{k}) = \int \rho(\mathbf{r}) \exp(-i2\pi \mathbf{k} \mathbf{r}) d\mathbf{r}, \quad (1.8)$$

where $S(\mathbf{k})$ is a Fourier pair with respect to $\rho(\mathbf{r})$. Thus, the n -dimensional signal, $S(\mathbf{k})$, can be Fourier-transformed to yield a n -dimensional spatial dataset.

From Eqs. 1.6 – 1.8 it can be seen that field gradients are, besides the r.f. pulses, another important component of an MRI pulse sequence. To better understand the role that both these components play in an MRI experiment, the fate of the bulk magnetization is followed during a spin echo (SE) MRI pulse sequence (Fig. 1.3), as one of the most commonly used sequences for imaging. A typical MRI experiment does not detect the signal from the whole volume of the sample but only from a thin slice, achieved by the concomitant application of a so-called ‘soft’ 90° r.f. excitation pulse, and a slice-selective gradient, G_{slice} (Fig. 1.3, box A). ‘Soft’ r.f. pulses are low-power, long-duration pulses that typically affect spins in a much narrower frequency bandwidth than the so-called ‘hard’ r.f. pulses, enabling, *e.g.*, excitation of only the spins precessing with specific frequencies, *i.e.*, within the chosen slice.⁵⁹ The subsequent application of a frequency-encoding or read gradient, G_{read} (Fig. 1.3, box B), results in the precession of spins with spatially-dependent frequencies, thus allowing for spatial encoding along the chosen read direction. As this causes dephasing of the signal and a decay of M_0 , before signal acquisition a 180° r.f. pulse (Fig. 1.3, box C) is used to invert the magnetic moments. The signal is then refocused

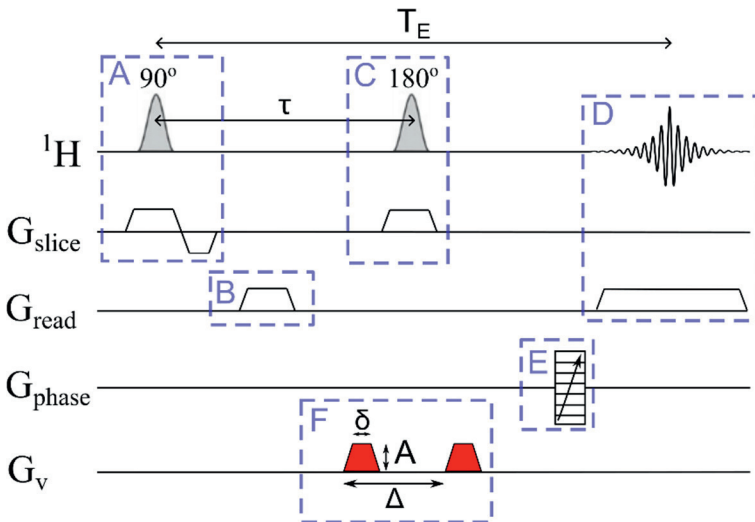


Figure 1.3: Scheme of a 2D Pulsed Field Gradient Spin Echo (PFG-SE) pulse sequence, used for velocimetry measurements. The applied magnetic field gradients along the slice and read directions are represented as empty trapezoids. Stepping through the gradient amplitudes in the phase encoding direction is represented with a stepped column, with an arrow. The velocity encoding gradients in an arbitrary direction are shown as red trapezoids. Shaded bell shapes represent the soft r.f. pulses with the respective angles marked. Durations τ and T_E represent the time between the 90° and the 180° r.f. pulses and the echo time, respectively.

into a spin echo by the second G_{read} (Fig. 1.3, box D), with the signal reaching the maximum intensity at the echo time, T_E , equal to twice the duration between the 90° and 180° r.f. pulses, namely 2τ . For 2- and 3D images the use of additional, incremented phase-encoding gradients, G_{phase} , is necessary (Fig. 1.3, box E).⁶⁰ Importantly, the phase $\varphi(\mathbf{r}, t)$ of the detected signal is sensitive not only to the position of the spins, but also to their displacement. Hence, spatially-resolved velocimetry measurements can be carried out by adding a velocity encoding gradients, G_v , as a pair of short gradient pulses (Fig. 1.3, box F). The final phase of the signal is thus the result of the action of all applied gradients for position and velocity encoding. The resulting pulse sequence is commonly referred to as a Pulsed Field Gradient SE (PFG-SE). In the simple case of a 1D PFG-SE, where a constant G_{read} is applied along the z -axis, and the G_v is applied along the y -axis, the accumulated phase can be written as:

$$\varphi(z, t) = \gamma \left[G_z t z + G_v \int_0^t y(t') dt' \right], \quad (1.9)$$

where $y(t')$ describes motion of the spins, according to $y_0 + v_0 t + 1/2 a_0 t^2 + \dots$. These terms respectively represent the initial position, y_0 , constant velocity, v_0 , constant acceleration, a_0 , and higher order motion, with only the first two being typically quantified with MRI.⁶¹ For the static spins, the application of the two G_v will yield no net phase accumulation, resulting in refocusing of the signal. For the spins flowing with a constant v_0 the action of the second gradient cannot refocus the action of the first, as the spins have moved during the observation time Δ . This results in spatially-dependent phase accumulation $\varphi(z)$. By solving the integral in Eq. 1.9, the phase can be then related to local velocities according to:

$$v(z) = \frac{\varphi(z)}{\gamma A \delta \Delta}, \quad (1.10)$$

where A and δ are respectively the amplitude and duration of G_v , as shown in Fig. 1.3.

Rotational rheo-MRI setup. A typical rotational rheo-MRI velocimetry setup^{18,62} (Fig. 1.4) can be used to study flow in two geometries: a CC or a CP, wherein the sample of interest is sheared between the outer static and the inner rotating wall. The rotating parts, namely the bob in the CC or the cone in the CP, are connected with the motor, located on top of the magnet, via a long drive shaft, with length, $l_{DS} \approx 1$ m. The motor drives the rotation and controls the shear applied to the sample. The

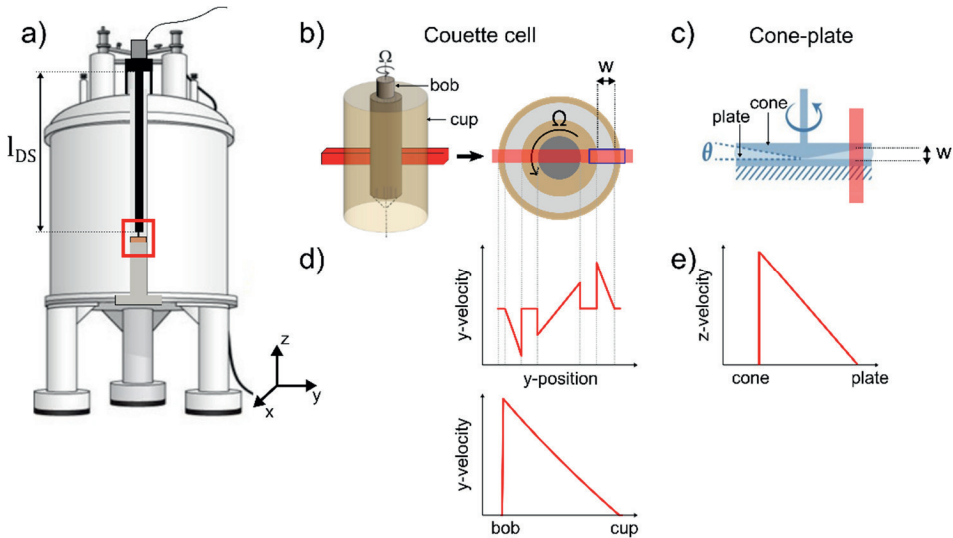


Figure 1.4: a) Scheme of the rotational rheo-MRI setup, with drive shaft length marked as l_{DS} , and the flow geometry fixed in the sensitive region of the probe, marked with a red rectangle. b, c) Commonly used geometries in rotational rheo-MRI, namely CC and CP, with gap size, w .¹⁸ Red shaded rectangles represent the typical location and orientation of a slice where a 1D velocity profile is measured. d, e) Illustrative velocity profiles of a Newtonian fluid flowing in a CC and CP respectively. The top profile in d) results from the excitation of the slice marked with the shaded, red rectangle in b), whereas the bottom profile results from the excitation of the signal from solely within the gap.

resulting flow of the sample can be measured as a 2D velocity map or a 1D velocity profile in a chosen location or slice of the geometry. The typical location and orientation of slices in CC and CP geometries are shown in Fig. 1.4b and 1.4c, respectively, alongside the resulting, illustrative velocity profiles of a Newtonian fluid. Notably, in the case of the CC, the slice length can be reduced from 25 mm to ~ 10 mm to capture the flow information only from one side of the gap with respect to the bob, which allows for improvement of the available spatial resolution by up to 40%. The rotational rheo-MRI setup offers access to shear rates in the range $\sim 0.1 - 50 \text{ s}^{-1}$ with the possibility to measure velocities ranging from $\sim 0.1 \text{ mm/s}$ up to tens of cm/s, with the spatial resolution of $\sim 10 \mu\text{m}/\text{pixel}$.

One of the main differences between the two geometries and a big consideration for experimental design is the distribution of stress applied to the sample across the shear gap. In the CP, the stress variation is within 1% for angles $\theta < 6^{\circ}$ ³ whereas, for

the CC, stress is proportional to $1/r^2$, with the stress variation increasing quadratically with increasing gap size. In the case of a CC where $w \leq 0.1$ mm, the stress can be approximated as constant. Yet, CCs with such small gap sizes are practically unattainable due to the challenging alignment of the respective centers of the bob and the cup, necessary to avoid off-axis rotation. As a consequence, even in classical global rheology CCs with gap sizes of ~ 0.5 mm are typically used.³

Narrow gap CCs offer the best experimental conditions for studies of flow cooperativity. Firstly, the narrow gap ensures narrow stress distribution, resulting in velocity profiles of most fluids being close to linear. This allows for an easy identification of cooperative or thixotropic properties from the curvature of the velocity profiles. Secondly, the uniform gap size along the entire slice thickness grants good control over the degree of flow confinement. Wide gap CCs offer access to, *e.g.*, sample's yield stress properties by providing insight into shear banding (Fig. 1.5). However, in this CC, cooperativity can be partly masked by stress distribution effect, as the latter also yields curved velocity profiles. While the CP offers the most uniform stress conditions, its non-uniform gap size has two drawbacks. Firstly, flow confinement is position-dependent, which can lead to a coexistence of confined and non-confined flow regimes. Secondly, finite slice thickness, selected in an MRI

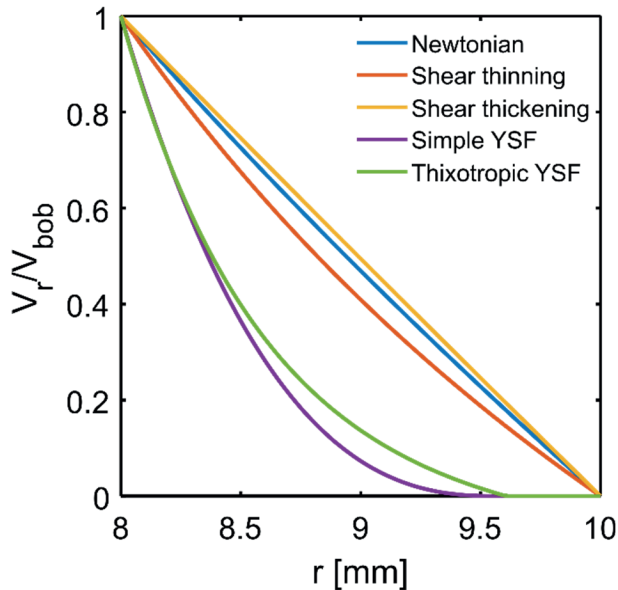


Figure 1.5: Calculated radial velocity profiles, V_r , normalized to the velocity at the bob, V_{bob} of fluids with different rheological properties, plotted as a function of the radial position, r in the gap for a CC with a gap size of 2 mm.

measurement inherently yields uncertainty on the gap size. Both these factors make accurate quantification of cooperativity effects in the CP challenging, in spite of the benefit of uniform stress.

Aside from the access to spatio-temporal flow inhomogeneities, spatially-resolved velocity profiles provide the so-called local flow curves. In contrast to the traditional global flow curves, where spatial flow homogeneity across the gap is assumed, local flow curves reflect the true behavior of the sample, without assumptions on the flow behavior or effective shear rate homogeneity. Local flow curves are derived by calculating the local shear rates, $\dot{\gamma}(r)$, from the slopes of the measured velocity profiles according to $\dot{\gamma}(r) = r \frac{\partial(v_r/r)}{\partial r}$. The corresponding local stresses for the CC geometry can be calculated as $\sigma(r) = T/2\pi Hr^2$, where T is the torque exerted by the fluid on the rotating bob, measured with a rheometer, and H is the height of the bob.

Rotational rheo-MRI/NMR also offers the possibility to study the effect of temperature on flow, the microstructure or even molecular level phenomena. A temperature-control element can be integrated within the walls of the CC or the CP in the form of channels through which a heating fluid, *e.g.*, water or air can flow. Such approach, specifically using nitrogen gas for controlling the temperature, was pioneered by Laryea *et al.*⁶³ for rheo-NMR spectroscopy studies of temperature-sensitive free radical polymerization. However, so far temperature-control has not been explored in rheo-MRI velocimetry measurements, and is in fact one of the targeted developments during this thesis work.

Finally, it should be noted that measurements other than velocimetry can be carried out during a rheo-MRI experiment. Examples include localized or bulk spectroscopy,⁶⁴ providing molecular level information, multinuclear NMR experiments,⁶⁵ enabling studies of, *e.g.*, alignment, or relaxometry, yielding access to local viscosity and concentration gradients¹¹.

Given all the advantages offered by rotational rheo-MRI and its versatility, the technique has been widely used in the field of soft matter to detect and quantify spatial flow instabilities. In the past two decades, rotational rheo-MRI studies have provided evidences for a wide range of phenomena, listed below.

- a) Difference in the physical origin of shear bands in simple and thixotropic YSFs.^{66,67} For the former class of fluids, the transition between the liquid and

solid phase was shown to be gradual, and originating from stress values across the gap approaching σ_y . For thixotropic YSFs, the transition between the two phases is abrupt, as can be seen from the discontinuity in the slope of the velocity profile in Fig. 1.5. Such clear separation of bands originates from the microstructural adaptation to shear, forming coexisting phases that flow with different shear rates.⁸

- b) Flow-induced structural alignment of fluids with anisotropic particles such as wormlike micelles and liquid crystals. For wormlike micelles, the alignment manifests itself as shear bands whose temporal stability, thickness and dependence on flow geometry has been studied with rotational rheo-MRI velocimetry.^{21,22,68} For liquid crystals, the alignment has been studied and quantified via the quadrupolar splitting in ^2H NMR spectra of the deuterated solvent.^{69,70}
- c) Shear-induced network degradation and ageing in fat crystal dispersions (FCDs)²⁰ and waxy oil suspensions.^{71,72} These studies revealed the underlying microscopic origin of thixotropy in these materials, providing the respective industries with guidelines for the formulation of FCDs and applied pressures for the waxy oil suspensions.
- d) Shear-induced particle migration in emulsions and granular materials, pinpointing particle density variations as a source of spatial dependence of viscosity in those materials.^{11,73}
- e) Wall slip in a broad range of fluids, allowing for direct quantification of the slip velocity and for studies of the dependence of wall slip on microstructural properties.^{74,75}

This non-exhaustive list of research areas demonstrates the rich history of rotational rheo-MRI in soft matter topics and its role as a springboard towards an improved understanding of the physical origin of the fluids' rheological properties. It comes, thus, as no surprise that rotational rheo-MRI has been already exploited in studies and quantification of cooperativity in flow of real-life, optically-opaque fluids.^{13,24,32} However, the technical limitations, namely the availability of CCs with gaps limited to a range 1 - 4 mm has restricted the studies of cooperativity to materials with mm-sized particles. Notably, the CP geometry, with the radially decreasing gap size, has been used for cooperative studies in materials with $\sim\mu\text{m}$ sized particles. However, the non-uniform gap size of the CP renders it impossible to impose a uniform flow confinement degree on the fluid.

A microcapillary rheo-MRI setup is an alternative approach to rotational rheo-MRI in MRI velocimetry studies. The setup offers easier scalability of the flow confinement size within mm- and sub-mm range, down to $\sim 50 \mu\text{m}$ for MRI applications, as commercially available microcapillaries can be employed. The uniform size of the flow gap in the direction of the excited slice provides good control over the flow confinement degree, while the small cross sections of the capillaries enable using small Field of View (FOV) values, and, thus, offer improved spatial and temporal resolutions as compared to rotational rheo-MRI setups. On the other hand, the presence of 100% stress variation within the gap of a microcapillary, the small sample volumes, the challenges in the alignment with the B_0 field within the spectrometer, and the mechanical stability can be expected to play a role in the experimental setting and need to be taken into consideration in development of such a setup.

1.4. Impact of microstructure on cooperativity

The new rotational and microcapillary rheo-MRI developments presented in this thesis are first validated with Newtonian fluids, to assess the mechanical stability of the flow geometries, temporal stability of flow and flow quantification methods. Following such validations, the platforms are applied to study the dependence of flow cooperativity on microstructural parameters, for which YSFs with modifiable microstructures are required. Below fluids studied during this thesis work are described.

1.4.1. Carbopol

Carbopol is a microgel composed of cross-linked polyacrylic acid particles, which form soft, sub- μm to μm -sized blobs once swelled with water (Fig. 1.6a).^{28,76} Due to the dramatic expansion of up to 10 times the original particle size as a result of swelling, they become jammed, giving rise to yield stress properties. Carbopol is arguably one of the most commonly used model fluids in studies of flow, yielding and thixotropy, as well as an important industrial thickening agent.^{28,77} Strongly confined flow of Carbopol has been shown to exhibit blob-size dependent cooperativity effects.¹⁴ Thus in this thesis work, Carbopol with small particles of $\sim 2 \mu\text{m}$ is used as a reference for studying cooperativity in capillaries with the smallest radius.

1.4.2. FCDs

FCDs are dispersions of solid fat in liquid oil and are used in production of an array of fat-based food products, such as chocolate and margarine.⁷⁸ In most FCDs, solid fat

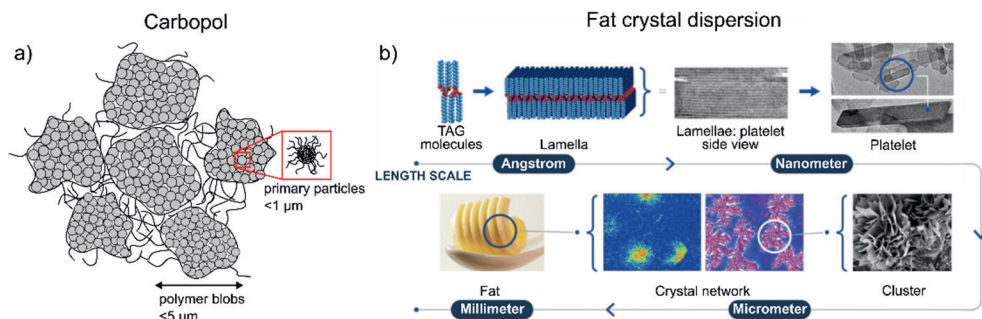


Figure 1.6: Schemes representing a) the microstructure of Carbopol microgel, composed of swelled polymer blobs and b) the hierarchy of the fat crystal aggregate network of the FCDs. Schemes are reproduced from Oelschlaeger et al.⁷⁶ and Marangoni et al.⁸⁰, respectively.

is present in the form of crystalline nanoplatelets, which are in turn aggregated into μm -sized structures (Fig. 1.6b).^{79,80} The exact morphology of the multi length scale structure, including the crystalline form, platelet thickness, and sizes of the aggregates is highly dependent on the sample preparation conditions and can be controlled by varying, *e.g.*, the crystallization rate, crystallization temperature or the applied shear.^{78,81} As a result, FCDs are a suitable, real-life system for probing the dependence of cooperativity on microstructural parameters, such as crystal aggregate sizes and polydispersity, both controlled by varying the crystallization rate. Furthermore, these studies are industrially relevant, as the influence of the microstructure on flow of FCDs is still not well understood, resulting in the lack of comprehensive theoretical models for flow predictions.

Another processing route, offering control over the microstructure, involves spraying the solid fat blend to form crystalline nanoplatelets, termed micronized fat crystals (MFCs), which are subsequently dispersed in a continuous phase.⁸² The decoupling of crystallization and microstructure formation steps offers an enhanced control over the microstructure, yet, the obtained products are highly sensitive to shear history and ageing.²⁰ In the final part of this thesis, strongly confined flow of MFCs as a function of shear time is characterized.

1.5. Thesis outline

The topics covered in the subsequent chapters are schematically illustrated in Fig. 1.7. **Chapters 2** and **4** describe the technical flow-MRI developments achieved during the thesis work, while **Chapters 3** and **5** concern the applications of the respective

flow-MRI platforms to quantitative studies of cooperativity effects. Cooperativity is quantified using the fluidity model owing to its simplicity and wide-spread use in studies of strongly confined flow in a range of soft particulate fluids.

Chapter 2 describes the development of a temperature-controlled CC with $w = 500 \mu\text{m}$. In addition to making the step towards the narrow-gap condition to study strongly confined flow, the notorious issue of mechanical instability of the bob in rotational rheo-MRI CCs is being tackled. The achieved improvements are validated and exploited in a proof-of-concept study of sub-mm flow of 27 wt% FCDs at three temperatures varying between 15 and 30 °C, using a 300 MHz MRI spectrometer. The use of a relatively high solid fat concentration of 27 wt% was dictated by the fact that concentrated dispersions are expected to exhibit stronger effect of cooperativity.

In **Chapter 3**, the developed 500 μm gap CC is applied to study the sub-mm flow of 27 wt% FCDs as a function of the crystal aggregate size, in turn controlled by the crystallization rate. A numerical modelling approach based on the fluidity model is introduced, by which the ξ values can be determined, even under the non-uniform stress field of the CC. A stress-independent ξ definition is assumed, based on the relatively low stress variation of 10% present in the used CC geometry. The observed varying extent of flow cooperativity across the microstructurally distinct samples is discussed and linked to the properties of the microstructure.

In **Chapter 4**, a microcapillary rheo-MRI platform is developed to comprehensively study sub-mm flow in geometries with an easily scalable gap size down to 100 μm and modifiable wall properties. The advantages of the setup are demonstrated in studies of confined flow of 0.5 wt% Carbopol in capillaries with hydrophilic or hydrophobic walls and of 15 wt% FCDs as a function of the confinement size, using a 600 MHz MRI spectrometer. The varied flow conditions allow to investigate the effect of fluid-wall interactions and the flow confinement degree on flow cooperativity, respectively. As can be noted, the concentration of solid fat in the dispersions used in this work is lower than that of samples used in **Chapters 2** and **3**. This was dictated by the necessity to lower the σ_y of the fluid, to be able to pump the dispersions through gaps as small as 250 μm , with the maximum available pressure of 8 bar. The change in solid fat content also allows to study the dependence of flow cooperativity on concentration in FCDs. For quantification of cooperativity lengths, the stress-independent ξ definition is maintained for consistency with the CC data and for comparability with other literature studies, despite the presence of a 100% stress variation.

In **Chapter 5**, flow of concentrated MFC dispersions in a 250 μm confinement is explored. The evolution of the fundamental rheological properties of the used material as a function of pre-shear time is demonstrated with microcapillary rheo-MRI velocimetry measurements. The obtained local flow behavior is explained in terms of shear- and temperature-induced changes in the microstructure on the μm and nm length scale.

The General Discussion (**Chapter 6**) consists of two parts. In the first part, the properties of the two velocimetry platforms developed throughout this thesis work are compared with regards to their experimental capabilities. The section is concluded with perspectives for further improvements. In the second part, ξ values found in FCDs and Carbopol throughout this thesis work are compiled with values reported in literature studies for other cooperative fluids and experimental conditions. Based on that comparison, conclusions are drawn about the key factors governing flow cooperativity effects. As an outlook towards a more accurate and robust quantification of ξ , two approaches based on the fluidity model are proposed and discussed: (i) modelling of stress-dependent ξ values and (ii) modelling of cooperative flow while accounting for sample's thixotropic properties in a flow geometry with a non-uniform stress field. Finally, future research questions regarding flow cooperativity are proposed, which can be answered by using the technical developments within MRI velocimetry, achieved in this thesis.

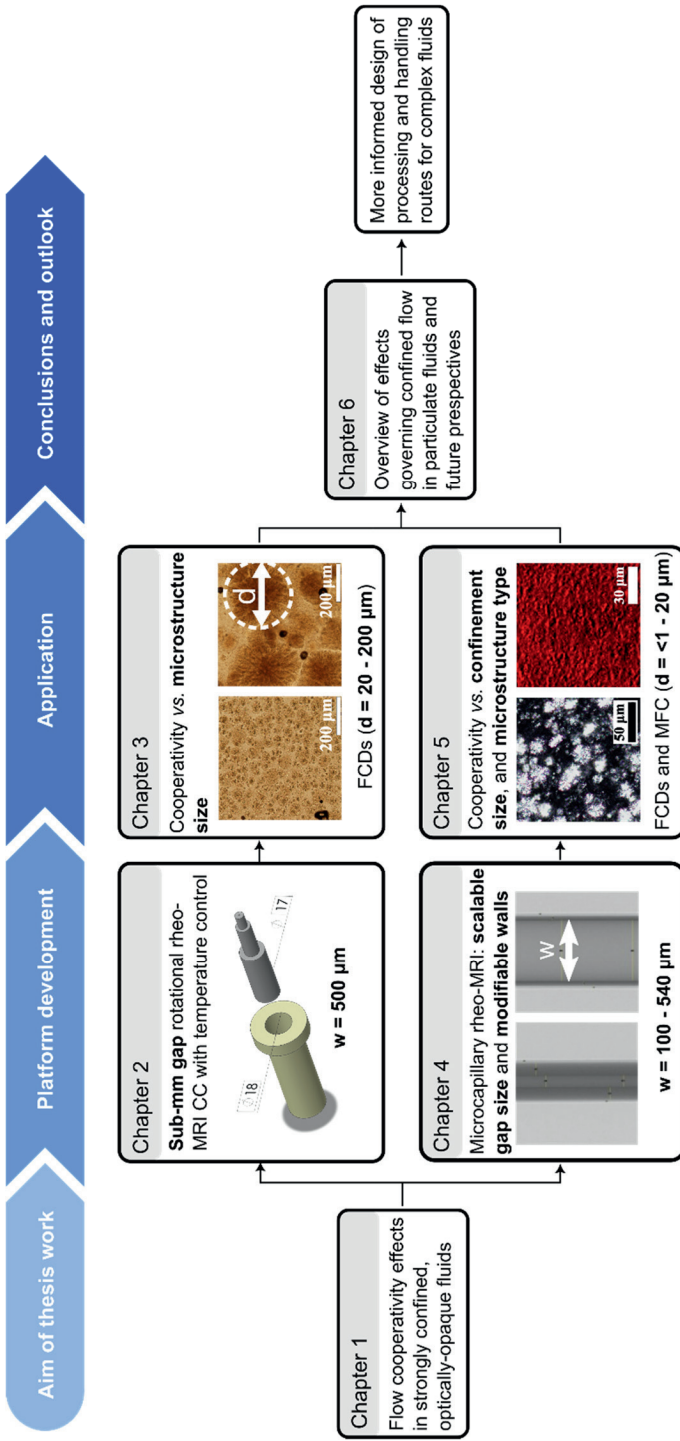


Figure 1.7: Graphical outline of the thesis, showing the key technical developments (**Chapter 2 and 4**) and the respective applications (**Chapter 3 and 5**) achieved during this thesis work. The bold phrases refer to the properties of experimental methods reviewed in Table 1.1.

References

- (1) Anna, S. L. Droplets and Bubbles in Microfluidic Devices, *Annu. Rev. Fluid Mech.* **2016**, *48* (1), 285-309.
- (2) Dollet, B.; Scagliarini, A.; Sbragaglia, M. Two-dimensional plastic flow of foams and emulsions in a channel: experiments and lattice Boltzmann simulations, *J. Fluid Mech.* **2015**, *766*, 556-589.
- (3) Macosko, C. W. *Rheology: Principles, Measurements and Applications*, 1st ed.; John Wiley & Sons, 1994.
- (4) Kyriakopoulou, K.; Dekkers, B.; van der Goot, A. J. In *Sustainable Meat Production and Processing*, Galanakis, C. M.; Academic Press, 2019, pp 103-126.
- (5) Venkatesan, R.; Östlund, J.-A.; Chawla, H.; Wattana, P.; Nydén, M.; Fogler, H. S. The Effect of Asphaltenes on the Gelation of Waxy Oils, *Energy Fuels* **2003**, *17* (6), 1630-1640.
- (6) Fall, A.; Paredes, J.; Bonn, D. Yielding and Shear Banding in Soft Glassy Materials, *Phys. Rev. Lett.* **2010**, *105* (22), 225502.
- (7) Jenny, M.; Kiesgen de Richter, S.; Louvet, N.; Skali-Lami, S.; Dossmann, Y. Taylor-Couette instability in thixotropic yield stress fluids, *Phys. Rev. Fluids* **2017**, *2* (2), 023302.
- (8) Møller, P. C. F.; Rodts, S.; Michels, M. A. J.; Bonn, D. Shear banding and yield stress in soft glassy materials, *Phys. Rev. E* **2008**, *77* (4), 041507.
- (9) Isa, L.; Besseling, R.; Poon, W. C. K. Shear Zones and Wall Slip in the Capillary Flow of Concentrated Colloidal Suspensions, *Phys. Rev. Lett.* **2007**, *98* (19), 198305.
- (10) Zhang, X.; Lorenceau, E.; Bourouina, T.; Basset, P.; Oerther, T.; Ferrari, M.; Rouyer, F.; Goyon, J.; Coussot, P. Wall slip mechanisms in direct and inverse emulsions, *J. Rheol.* **2018**, *62* (6), 1495-1513.
- (11) Serial, M. R.; Nikolaeva, T.; Vergeldt, F. J.; van Duynhoven, J. P. M.; van As, H. Selective oil-phase rheo-MRI velocity profiles to monitor heterogeneous flow behavior of oil/water food emulsions, *Magn. Reson. Chem.* **2019**, *57* (9), 766-770.
- (12) Goyon, J.; Colin, A.; Ovarlez, G.; Ajdari, A.; Bocquet, L. Spatial cooperativity in soft glassy flows, *Nature* **2008**, *454*, 84-87.
- (13) de Kort, D. W.; Veen, S. J.; Van As, H.; Bonn, D.; Velikov, K. P.; van Duynhoven, J. P. M. Yielding and flow of cellulose microfibril dispersions in the presence of a charged polymer, *Soft Matter* **2016**, *12* (21), 4739-4744.
- (14) Géraud, B.; Jørgensen, L.; Ybert, C.; Delanoë-Ayari, H.; Barentin, C. Structural and cooperative length scales in polymer gels, *Eur. Phys. J. E* **2017**, *40* (5), 1-10.
- (15) Goyon, J.; Colin, A.; Bocquet, L. How does a soft glassy material flow: finite size effects, non local rheology, and flow cooperativity, *Soft Matter* **2010**, *6* (12), 2668-2678.
- (16) Masselon, C.; Salmon, J.-B.; Colin, A. Nonlocal Effects in Flows of Wormlike Micellar Solutions, *Phys. Rev. Lett.* **2008**, *100* (3), 038301.
- (17) Paredes, J.; Shahidzadeh, N.; Bonn, D. Wall slip and fluidity in emulsion flow, *Phys. Rev. E* **2015**, *92* (4), 042313.
- (18) Callaghan, P. T. Rheo-NMR: nuclear magnetic resonance and the rheology of complex fluids, *Rep. Prog. Phys.* **1999**, *62* (4), 599-670.
- (19) Nikolaeva, T.; den Adel, R.; van der Sman, R.; Martens, K. J. A.; Van As, H.; Voda, A.; van Duynhoven, J. P. M. Manipulation of Recrystallization and Network Formation of Oil-Dispersed Micronized Fat Crystals, *Langmuir* **2019**, *35* (6), 2221-2229.
- (20) Nikolaeva, T.; den Adel, R.; Velichko, E.; Bouwman, W. G.; Hermida-Merino, D.; Van As, H.; Voda, A.; van Duynhoven, J. P. M. Networks of micronized fat crystals grown under static conditions, *Food Funct.* **2018**, *9* (4), 2102-2111.
- (21) Angelico, R.; Gentile, L.; Ranieri, G. A.; Oliviero Rossi, C. Flow-induced structures observed in a viscoelastic reverse wormlike micellar system by magnetic resonance imaging and NMR velocimetry, *RSC Adv.* **2016**, *6* (40), 33339-33347.

- (22) Brox, T. I.; Douglass, B.; Galvosas, P.; Brown, J. R. Observations of the influence of Taylor-Couette geometry on the onset of shear-banding in surfactant wormlike micelles, *J. Rheol.* **2016**, *60* (5), 973-982.
- (23) Graziano, R.; Preziosi, V.; Uva, D.; Tomaiuolo, G.; Mohebbi, B.; Claussen, J.; Guido, S. The microstructure of Carbopol in water under static and flow conditions and its effect on the yield stress, *J. Colloid Interface Sci.* **2021**, *582*, 1067-1074.
- (24) Serial, M. R.; Velichko, E.; Nikolaeva, T.; den Adel, R.; Terenzi, C.; Bouwman, W. G.; van Duynhoven, J. P. M. High-pressure homogenized citrus fiber cellulose dispersions: Structural characterization and flow behavior, *Food Struct.* **2021**, *30*, 100237.
- (25) Tyowua, A. T.; Yiase, S. G.; Binks, B. P. Double oil-in-oil-in-oil emulsions stabilised solely by particles, *J. Colloid Interface Sci.* **2017**, *488*, 127-134.
- (26) Chen, K.; Chen, M.; Feng, Y.; Yu, G.; Zhang, L.; Li, J. Application and rheology of anisotropic particle stabilized emulsions: Effects of particle hydrophobicity and fractal structure, *Colloids Surf. A: Physicochem. Eng.* **2017**, *524*, 8-16.
- (27) Bonn, D.; Denn, M. M.; Berthier, L.; Divoux, T.; Manneville, S. Yield stress materials in soft condensed matter, *Rev. Mod. Phys.* **2017**, *89* (3), 035005.
- (28) Dinkgreve, M.; Fazilati, M.; Denn, M. M.; Bonn, D. Carbopol: From a simple to a thixotropic yield stress fluid, *J. Rheol.* **2018**, *62* (3), 773-780.
- (29) Herschel, W. H.; Bulkley, R. Konsistenzmessungen von Gummi-Benzollösungen, *Kolloid-Zeitschrift* **1926**, *39* (4), 291-300.
- (30) Goodeve, C. F.; Whitfield, G. W. The measurement of thixotropy in absolute units, *Trans. Faraday Soc.* **1938**, *34*, 511-520.
- (31) Mewis, J.; Wagner, N. J. Thixotropy, *Adv. Colloid Interface Sci.* **2009**, *147-148*, 214-227.
- (32) Serial, M. R.; Bonn, D.; Huppertz, T.; Dijksman, J. A.; van der Gucht, J.; van Duynhoven, J. P. M.; Terenzi, C. Nonlocal effects in the shear banding of a thixotropic yield stress fluid, *Phys. Rev. Fluids* **2021**, *6* (11), 113301.
- (33) Larson, R. G.; Wei, Y. A review of thixotropy and its rheological modeling, *J. Rheol.* **2019**, *63* (3), 477-501.
- (34) Sollich, P.; Lequeux, F.; Hébraud, P.; Cates, M. E. Rheology of Soft Glassy Materials, *Phys. Rev. Lett.* **1997**, *78* (10), 2020-2023.
- (35) Picard, G.; Ajdari, A.; Lequeux, F.; Bocquet, L. Slow flows of yield stress fluids: Complex spatiotemporal behavior within a simple elastoplastic model, *Phys. Rev. E* **2005**, *71* (1), 010501.
- (36) Maloney, C.; Lemaître, A. Subextensive Scaling in the Athermal, Quasistatic Limit of Amorphous Matter in Plastic Shear Flow, *Phys. Rev. Lett.* **2004**, *93* (1), 016001.
- (37) Chikkadi, V.; Wegdam, G.; Bonn, D.; Nienhuis, B.; Schall, P. Long-Range Strain Correlations in Sheared Colloidal Glasses, *Phys. Rev. Lett.* **2011**, *107* (19), 198303.
- (38) Derzsi, L.; Filippi, D.; Mistura, G.; Pierno, M.; Lulli, M.; Sbragaglia, M.; Bernaschi, M.; Garstecki, P. Fluidization and wall slip of soft glassy materials by controlled surface roughness, *Phys. Rev. E* **2017**, *95* (5), 052602.
- (39) Meeker, S. P.; Bonnecaze, R. T.; Cloitre, M. Slip and flow in pastes of soft particles: Direct observation and rheology, *J. Rheol.* **2004**, *48* (6), 1295-1320.
- (40) Geraud, B.; Bocquet, L.; Barentin, C. Confined flows of a polymer microgel, *Eur. Phys. J. E* **2013**, *36* (3), 1-13.
- (41) Kamrin, K.; Koval, G. Nonlocal Constitutive Relation for Steady Granular Flow, *Phys. Rev. Lett.* **2012**, *108* (17), 178301.
- (42) de Cagny, H.; Fall, A.; Denn, M. M.; Bonn, D. Local rheology of suspensions and dry granular materials, *J. Rheol.* **2015**, *59* (4), 957-969.
- (43) Henann, D. L.; Kamrin, K. A predictive, size-dependent continuum model for dense granular flows, *Proc. Natl. Acad. Sci.* **2013**, *110* (17), 6730-6735.
- (44) Fielding, S. M.; Cates, M. E.; Sollich, P. Shear banding, aging and noise dynamics in soft glassy materials, *Soft Matter* **2009**, *5* (12), 2378-2382.

- (45) Falk, M. L.; Langer, J. S. Dynamics of viscoplastic deformation in amorphous solids, *Phys. Rev. E* **1998**, *57* (6), 7192-7205.
- (46) Pouliquen, O.; Forterre, Y. A non-local rheology for dense granular flows, *Philos. Trans. Royal Soc. A* **2009**, *367* (1909), 5091-5107.
- (47) Bocquet, L.; Colin, A.; Ajdari, A. Kinetic Theory of Plastic Flow in Soft Glassy Materials, *Phys. Rev. Lett.* **2009**, *103* (3), 036001.
- (48) Benzi, R.; Sbragaglia, M.; Succi, S.; Bernaschi, M.; Chibbaro, S. Mesoscopic lattice Boltzmann modeling of soft-glassy systems: Theory and simulations, *J. Chem. Phys.* **2009**, *131* (10), 104903.
- (49) Benzi, R.; Sbragaglia, M.; Perlekar, P.; Bernaschi, M.; Succi, S.; Toschi, F. Direct evidence of plastic events and dynamic heterogeneities in soft-glasses, *Soft Matter* **2014**, *10* (26), 4615-4624.
- (50) Moller, P.; Fall, A.; Chikkadi, V.; Derks, D.; Bonn, D. An attempt to categorize yield stress fluid behaviour, *Philos. Trans. Royal Soc. A* **2009**, *367* (1909), 5139-5155.
- (51) Bouzid, M.; Izzet, A.; Trulsson, M.; Clément, E.; Claudin, P.; Andreotti, B. Non-local rheology in dense granular flows, *Eur. Phys. J. E* **2015**, *38* (11), 5091-5107.
- (52) Raffel, M.; Willert, C.; Wereley, S.; Kompenhans, J. *Particle Image Velocimetry: A Practical Guide*, 3rd ed.; Springer, 2018.
- (53) Gallot, T.; Perge, C.; Grenard, V.; Fardin, M.-A.; Taberlet, N.; Manneville, S. Ultrafast ultrasonic imaging coupled to rheometry: Principle and illustration, *Rev. Sci. Instrum.* **2013**, *84* (4), 045107.
- (54) Takeda, Y. *Ultrasonic Doppler velocity profiler for fluid flow*, 1st ed.; Springer, 2012; Vol. 101.
- (55) Haavisto, S.; Cardona, M. J.; Salmela, J.; Powell, R. L.; McCarthy, M. J.; Kataja, M.; Koponen, A. I. Experimental investigation of the flow dynamics and rheology of complex fluids in pipe flow by hybrid multi-scale velocimetry, *Exp. Fluids* **2017**, *58* (11), 158.
- (56) Haavisto, S.; Salmela, J.; Koponen, A. Accurate velocity measurements of boundary-layer flows using Doppler optical coherence tomography, *Exp. Fluids* **2015**, *56* (5), 96.
- (57) Herle, V.; Manneville, S.; Fischer, P. Ultrasound velocimetry in a shear-thickening wormlike micellar solution: Evidence for the coexistence of radial and vorticity shear bands, *Eur. Phys. J. E* **2008**, *26* (1), 3-12.
- (58) Levitt, M. H. *Spin dynamics: basics of nuclear magnetic resonance*, 2nd ed.; John Wiley & Sons, 2013.
- (59) Keeler, J. *Understanding NMR Spectroscopy*, 2nd ed.; John Wiley & Sons, 2010.
- (60) Brown, R. W.; Cheng, Y.-C. N.; Haacke, E. M.; Thompson, M. R.; Venkatesan, R. *Magnetic resonance imaging: physical principles and sequence design*, 2nd ed.; John Wiley & Sons, 2014.
- (61) Callaghan, P. T. *Translational Dynamics & Magnetic Resonance*, 1st ed.; Oxford University Press, 2011.
- (62) Galvosas, P.; Brox, T. I.; Kuczera, S. Rheo-NMR in food science—Recent opportunities, *Magn. Reson. Chem.* **2019**, *57* (9), 757-765.
- (63) Laryea, E.; Schuhardt, N.; Guthausen, G.; Oerther, T.; Kind, M. Construction of a temperature controlled Rheo-NMR measuring cell—Influence of fluid dynamics on PMMA-polymerization kinetics, *Microporous Mesoporous Mater.* **2018**, *269*, 65-70.
- (64) Kind, J.; Thiele, C. M. MRI and localised NMR spectroscopy of sessile droplets on hydrophilic, hydrophobic and superhydrophobic surfaces – Examination of the chemical composition during evaporation, *J. Mag. Reson.* **2019**, *307*, 106579.
- (65) Echeverria, C.; Almeida, P. L.; Feio, G.; Figueirinhas, J. L.; Rey, A. D.; Godinho, M. H. Rheo-NMR study of water-based cellulose liquid crystal system at high shear rates, *Polymer* **2015**, *65*, 18-25.
- (66) Raynaud, J. S.; Moucheront, P.; Baudez, J. C.; Bertrand, F.; Guilbaud, J. P.; Coussot, P. Direct determination by nuclear magnetic resonance of the thixotropic and yielding behavior of suspensions, *J. Rheol.* **2002**, *46* (3), 709-732.
- (67) Coussot, P.; Raynaud, J.; Bertrand, F.; Moucheront, P.; Guilbaud, J.; Huynh, H.; Jarny, S.; Lesueur, D. Coexistence of Liquid and Solid Phases in Flowing Soft-Glassy Materials, *Phys. Rev. Lett.* **2002**, *88* (21), 218301.

- (68) Britton, M. M.; Callaghan, P. T. Shear banding instability in wormlike micellar solutions, *Eur. Phys. J. B* **1999**, *7* (2), 237-249.
- (69) Leal, C. R.; van der Klink, J.; Martins, A. F. Some aspects of the Rheo-NMR behavior of the lyotropic liquid crystal poly(γ -benzyl-L-glutamate) in m-cresol, *Mol. Cryst. Liq. Cryst.* **2004**, *420* (1), 35-45.
- (70) Geng, Y.; Almeida, P. L.; Feio, G. M.; Figueirinhas, J. L.; Godinho, M. H. Water-Based Cellulose Liquid Crystal System Investigated by Rheo-NMR, *Macromolecules* **2013**, *46* (11), 4296-4302.
- (71) Andrade, D. E. V.; Coussot, P. Brittle solid collapse to simple liquid for a waxy suspension, *Soft Matter* **2019**, *15* (43), 8766-8777.
- (72) Andrade, D. E. V.; Ferrari, M.; Coussot, P. The liquid regime of waxy oils suspensions: A magnetic resonance velocimetry analysis, *J. Non-Newton. Fluid Mech.* **2020**, *279*, 104261.
- (73) Ovarlez, G.; Bertrand, F.; Rodts, S. Local determination of the constitutive law of a dense suspension of noncolloidal particles through magnetic resonance imaging, *J. Rheol.* **2006**, *50* (3), 259-292.
- (74) Hollingsworth, K. G.; Johns, M. L. Rheo-nuclear magnetic resonance of emulsion systems, *J. Rheol.* **2004**, *48* (4), 787-803.
- (75) Ovarlez, G.; Rodts, S.; Ragouilliaux, A.; Coussot, P.; Goyon, J.; Colin, A. Wide-gap Couette flows of dense emulsions: Local concentration measurements, and comparison between macroscopic and local constitutive law measurements through magnetic resonance imaging, *Phys. Rev. E* **2008**, *78* (3), 036307.
- (76) Oelschlaeger, C.; Marten, J.; Péridont, F.; Willenbacher, N. Imaging of the microstructure of Carbopol dispersions and correlation with their macroelasticity: A micro- and macrorheological study, *J. Rheol.* **2022**, *66* (4), 749-760.
- (77) Bonn, D.; Denn, M. M. Yield Stress Fluids Slowly Yield to Analysis, *Science* **2009**, *324* (5933), 1401-1402.
- (78) Acevedo, N. C.; Block, J. M.; Marangoni, A. G. Critical laminar shear-temperature effects on the nano- and mesoscale structure of a model fat and its relationship to oil binding and rheological properties, *Faraday Discuss.* **2012**, *158*, 171-194.
- (79) Marangoni, A. G.; Acevedo, N.; Maleky, F.; Co, E.; Peyronel, F.; Mazzanti, G.; Quinn, B.; Pink, D. Structure and functionality of edible fats, *Soft Matter* **2012**, *8* (5), 1275-1300.
- (80) Marangoni, A. G.; van Duynhoven, J. P. M.; Acevedo, N. C.; Nicholson, R. A.; Patel, A. R. Advances in our understanding of the structure and functionality of edible fats and fat mimetics, *Soft Matter* **2020**, *16* (2), 289-306.
- (81) Maleky, F.; Smith, A. K.; Marangoni, A. Laminar Shear Effects on Crystalline Alignments and Nanostructure of a Triacylglycerol Crystal Network, *Cryst. Growth Des.* **2011**, *11* (6), 2335-2345.
- (82) Münüklü, P.; Jansens, P. J. Particle formation of an edible fat (rapeseed 70) using the supercritical melt micronization (ScMM) process, *J. Supercrit. Fluids* **2007**, *40* (3), 433-442

CHAPTER

2

Validation of temperature-controlled rheo-MRI measurements in a sub-mm gap Couette geometry

This chapter was published as:

Milc, K. W.; Serial, M. R.; Philippi, J.; Dijkman, J. A.; van Duynhoven, J. P. M.; Terenzi, C. Validation of temperature-controlled rheo-MRI measurements in a sub-mm gap Couette geometry, *Magn. Reson. Chem.*, **2022**, *60* (7), 606-614.

Abstract

A temperature-controlled sub-mm gap (500 μm) rheo-MRI Couette cell has been developed to measure confined flow of soft structured materials under controlled temperature. The proposed setup enables performing rheo-MRI measurements using (i) a spatially-uniform temperature control over the range 15 - 40 $^{\circ}\text{C}$, and (ii) a high spatial resolution up to 10 μm , as a consequence of the improved mechanical stability of the in-house developed rotating elements. Here, we demonstrate the performance of the cell for the rheo-MRI velocimetry study of a thixotropic fat crystal dispersion, a complex fluid commonly used in food manufacturing. The sub-mm gap geometry and variable temperature capability of the cell enable observing the effects of shear- and temperature-induced fat recrystallization on both wall slip and shear banding under strongly confined flow. Our improved rheo-MRI setup opens new perspectives for the fundamental study of strongly confined flow, cooperative effects, and the underlying inter-particle interactions and for ultimately aiding optimization of products involved in spreading/extrusion, such as cosmetics and foods.

2.1. Introduction

Industrially-relevant complex fluids, such as food dispersions or emulsion-based cosmetics and paints, flow through geometries that drastically vary in size during manufacturing or even customer use. In factories, pipes used for transporting such fluids between different process modules, have diameters of meters/centimeters, while millimeter/micrometer-sized nozzles are typically used for extrusion of fluids into molds and packaging. Flow in millimeter-sized gaps is also present during mastication and spreading of foods, governing mouthfeel and customer satisfaction. Additionally, flow through micron-scale geometries is encountered in many novel technologies, such as microflow reactors and 3D printing in food or chemical industry. Most structured fluids used in those processes, such as food colloids or polymer gels, exhibit a microstructure with length scales in the order of tens or hundreds of micrometers, and flow through gaps whose sizes are comparable with these structural length scales. In such conditions, flow can be considered as strongly confined, and can differ from non-confined flow as a result of inter-particle interactions.

Currently, standard rheology focuses mostly on bulk studies of non-confined flow of complex fluids.¹ Recent developments in the combination of rheology with molecular spectroscopy and/or imaging techniques have boosted our molecular-level understanding of non-confined flow, in relation with shear-induced microstructural rearrangements, even in complex fluids. For instance, rheo-Magnetic-Resonance-Imaging (rheo-MRI)²⁻⁴ enables detecting shear-induced structural changes, such as alignment^{5,6} or network destruction or rejuvenation,⁷ that occur at micro-/millimeter scales, while rheo-Small-Angle-X-ray-Diffraction (rheo-SAXD) offers insight into changes, *e.g.*, in terms of the sizes of the structural elements, that occur at a sub-micron scale.^{7,8} However, as has been demonstrated for emulsions⁹ and granular media,¹⁰ strongly-confined flow properties cannot be inferred from measurements carried out in non-confined conditions. When the confinement size, w , becomes comparable to the characteristic length scale of the fluid's microstructure, d , namely when $w \leq 100 \cdot d$, flow can become cooperative and, thus, spatially heterogeneous.⁹ Flow cooperativity is driven by non-local effects, where the local relation between stress and strain rate at a given location within the fluid can be strongly influenced by the plastic rearrangements occurring at a neighboring location, as illustrated in Fig. 2.1.^{9,11}

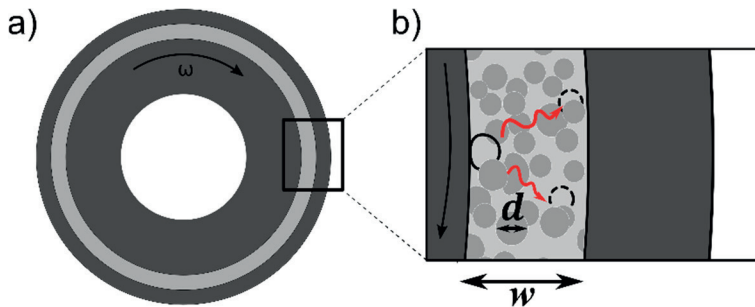


Figure 2.1: Schematic representation of a complex fluid, with particles of average diameter d , being sheared in a Couette Cell (CC) made of PEEK (dark grey) with gap size w . a) Top view of the CC; cup filled with the complex fluid (light grey) and bob filled with a reference fluid (white). b) Zoom-in of a gap-filling fluid exhibiting cooperative flow: when $w \leq 100 \cdot d$, plastic rearrangements (empty black circles) of particles can cause stress modulations throughout the gap (red arrows) resulting in additional correlated plastic rearrangements at neighboring sites (dashed black circles).

To quantitatively describe spatially-heterogeneous cooperative flow in soft structured dispersions, experimental flow setups are needed that enable velocimetry measurements in sub-mm gaps with high spatial resolution.^{4,12,13} Currently available methods for high resolution microfluidic flow measurements, e.g. Particle Image Velocimetry (PIV)^{9,14} or Dynamic Light Scattering (DLS)¹⁵, are not suitable for applications to most complex fluids, such as optically-opaque and strongly-scattering materials. Additionally, these methods often require the use of tracer particles, which in turn may alter the inter-particle interactions responsible for cooperative flow.

Rheo-MRI velocimetry¹⁶, already widely applied to room-temperature flow studies of complex fluids, does not suffer from any of the above mentioned limitations.^{2,3,17} Yet, so far only geometries with 1 – 4 mm gap sizes have been available, which are unsuitable for probing confinement effects in most food colloids due to (i) the excessively large gap size compared to the relevant structural lengths, and (ii) the non-negligible stress inhomogeneity throughout the gap, which in turn hampers the identification of cooperativity or other complex flow properties. The lack of geometries with sub-mm gap sizes is due to several challenges associated with their implementation in rheo-MRI setups. The first challenge is the low signal-to-noise ratio (SNR) in sub-mm geometries, due to both small sample volumes and the need to increase the MRI spatial resolution in order to acquire enough data points within the sub-mm gap. Achieving high MRI resolution is, in turn, hampered by the second

challenge, namely the off-axis mechanical displacement of the bob during rotation. The so-called ‘bob wobble’ is a well-known severe issue of rotating concentric cylindrical setups in general,¹⁸ including the currently available rheo-MRI geometries. Such wobbling limits the achievable spatial resolution typically to only about 50 μm , not sufficient for sub-mm geometries, and causes unstable shear flow as well as a fluctuating gap size during shear.¹⁹

Due to both its inherent complex phenomenology and the lack of versatile sub-mm flow setups, cooperativity is still poorly understood at the fundamental level and not yet quantified with a unique model. Additionally, not all fluids undergoing strongly confined flow exhibit cooperativity effects, while for some other fluids, such as polymer microgels,²⁰ these effects were observed even for the particle size to confinement ratio, $w/d \geq 100$.²¹⁻²³ Hence, despite its profound influence on bulk flow, *e.g.*, in terms of suppressing local yield stress,²⁴ cooperativity cannot yet be taken into account in the industrial design and manufacturing of foods, paints or other complex fluids, thus limiting the ability to correctly predict the microstructural and rheological properties of the final products. An additional key factor to be taken into account when optimizing manufacturing of most complex fluids, such as fat or fiber dispersions,²⁵⁻²⁷ polymer solutions,²⁸ granular media,¹⁰ or concentrated suspensions,²⁹ is temperature. The latter determines the microstructure, in terms of crystal form and particle sizes, as well as the viscosity of the final products. It is thus desirable to have highly-controlled temperature conditions during flow, and to be able to quantify the flow behavior and cooperativity effects as a function of temperature. The temperature ranges most commonly used during manufacturing vary depending on the industry and the flowing fluid. For production and design of foods it is particularly important to study the effect of temperatures in the range 10 – 80 °C. At these temperatures microstructure-formation processes take place, such as gelation, crystallization or dissolution.³⁰⁻³² Studies of the effect of body temperature on flow of fluids are also important for customer-oriented food design. To this goal, a few temperature-controlled shear CCs with mm-sized gaps have been constructed and used in rheo-NMR spectroscopy, and Small-Angle-Scattering (SAS) experiments.^{33,34} However, up to date temperature-controlled rheo-MRI velocimetric studies have not yet been carried out.

In the present work, we extend the well-established advantages of rheo-MRI towards temperature-controlled studies of strongly-confined flow of complex fluids, such as food dispersions or emulsions with particles larger than 10 μm , by developing and

validating a temperature-controlled rheo-MRI CC with a gap size of 500 μm . We first demonstrate the key technical improvements in our proposed sub-mm gap CC for rheo-MRI, namely: (i) the high mechanical stability of the bob, which enables imposing steady shear flow and measuring local velocity profiles with MRI spatial resolution up to 10 μm , and (ii) the spatially-uniform temperature control over 15 – 45 $^{\circ}\text{C}$, which enables the study of confined flow as a function of temperature. Thereafter, we show an illustrative application of the sub-mm gap CC for studies of confined flow in a 27 wt% fat crystal dispersion (FCD) at 15 and 30 $^{\circ}\text{C}$.

2.2. Improved design of the sub-mm gap rheo-MRI CC

Our proposed design for a sub-mm gap rheo-MRI CC is shown in Fig. 2.2. For its use in high-field NMR spectrometers, the cell is made of polyether ether ketone (PEEK), like all other available rheo-MRI geometries. The bob contains an internal chamber which can be filled with a reference Newtonian fluid. Both cup and bob have smooth walls, that can be modified by sandblasting or serration. For all experiments, the cup is filled with a sample and, upon insertion of the bob, the sample is enclosed within a gap of 500 μm . For improving the off-axis mechanical stability during rotation, the bob has been designed as one-piece and the bearing has been extended further down into the cup to better fix the axis of rotation. In the commercially-available mm-gap rheo-MRI geometries, the bob is made as a two-piece element with a separate top, and the bearing is shorter by 5 mm as compared to our new design: both factors make the mm-gap setups less mechanically stable in the off-axis direction. In addition, in our new sub-mm gap CC the casing of the cup houses a water circuit, that can be connected to an external water bath operating at both

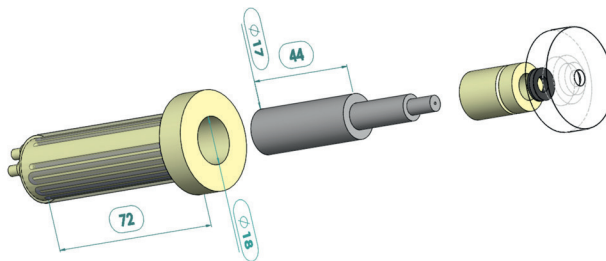


Figure 2.2: Technical drawing of the sub-mm gap rheo-MRI CC made of PEEK. From left to right: cup with the temperature control water circuit, the bob and the bearing. All dimensions are in mm. The outer shield of the cup and the top part of the bearing are made semi-transparent in the figure for visibility of the water circuit and of the rubber o-ring, respectively. The design of the cell and the technical drawing were done in SolidWorks 2018.

temperatures, $T_b \sim 15 - 45$ °C, with which the sample temperature, T_s , can be controlled during shear. The upper temperature limit of 45 °C in this design is dictated by the highest temperature that the glue used in construction of the cell can withstand. As PEEK can withstand up to 170 °C, the current temperature limit could be extended by using an appropriately heat-resistant glue. Similarly to the commercially-available rheo-MRI setups, the assembly of the cell prohibits shear stress measurements inside the MRI spectrometer. However, the whole cell is replicated to also fit into a standard cup holder for Anton Paar rheometers for torque measurements, and the bob can be used with a commercially available custom shaft holder.¹⁹

2.3. Materials and methods

2.3.1. Sample preparation

Micronized fat crystals (MFCs), prepared as described elsewhere⁷, were added to a commercial sunflower oil in a 3:8 (w/w) ratio and the blend was heated to 50 °C to erase crystal polymorphic history. The mixture was cooled to 20 °C at a rate of 0.2 °C/min. The obtained FCD contained polydispersed spherulitic fat crystallite aggregates with diameter of approximately 150 μm . The sample was used for measurements within 8 h from the crystallization.

2.3.2. Rheo-NMR/-MRI measurements

All MRI and rheo-MRI experiments were performed on a wide-bore Bruker Avance III spectrometer operating at 7 T. Excitation and detection of the ^1H signal was performed with a bird-cage radiofrequency coil with an inner diameter of 25 mm, in the standard microimaging gradient system Micro 2.5 (Bruker) with maximum gradient intensity of 1.5 T m^{-1} along all three axes. For rheo-MRI measurements, the Bruker rheo-MRI accessory was used in combination with the custom-made 500 μm gap CC or the commercially available serrated CC with $r_i/r_o = 7/11$ mm (4 mm gap), also made of PEEK.

^1H rheo-MRI measurements aiming at assessing the mechanical stability of the bob were performed with the cup and bob filled with distilled water doped with 1 wt% CuSO_4 (Merck), to decrease the NMR longitudinal relaxation time of water to about 20 ms. The decreased relaxation time enabled using a short repetition time, $T_R = 14$ ms, and a number of scans, $NS = 1$ while retaining a high SNR. As a result, the duration of 1 scan was minimized to 7 s, as required for the scopes of this set of

measurements. For the acquisition of images under the constant rotation of the bob at 0.72 rpm Fast Low Angle SHot (FLASH) MRI sequence was used with a slice selective sinc excitation pulse of duration 1 ms and tip angle of 30°. The field-of-view (FOV) was 20 x 20 mm and the resulting spatial resolution was 40 x 40 $\mu\text{m}/\text{pixel}$. Consecutive images were acquired over three axial slices, each 1 mm thick, at heights $z = 8, 16$ and 22 mm from the bottom of the bob. Acquisition of each image lasted 7 s, therefore to measure over 2 rotations of the bob (167 s), 25 images were acquired. The position of the center of the cup and that of the bob were extracted from each image using a circle-tracking algorithm in MATLAB R2018b that enables sub-pixel accuracy in the centroid estimation. The coordinates of the two centers were subtracted from each other to yield the positions of the bob's center with respect to the cup's center in consecutive images.

^1H Chemical Shift Imaging (CSI) NMR measurements of CH_3OH (Merck, purity > 99 %) filling both the cup and the bob were conducted to calibrate the temperature over the range $T_b = 15 - 45$ °C in steps of 5 °C. CSI spectra from three axial slices, 1 mm thick each, at heights $z = 18, 26$ and 32 mm from the bottom of the cup were recorded with a FOV of 25.6 x 25.6 mm, and the resolution of 40 x 40 $\mu\text{m}/\text{pixel}$. The local temperature in each pixel, T_{loc} , was calculated from the difference in chemical shift ($\Delta\delta$) between the CH_3 and the OH methanol peaks using the following equation:³⁵

$$T_{loc}[\text{°C}] = 135.85 - 36.54 \cdot \Delta\delta - 21.85 \cdot \Delta\delta^2. \quad (2.1)$$

The *in situ* sample temperature, T_s^{MRI} , was calculated by averaging values of T_{loc} within and over the 3 slices. The bulk, *ex situ*, temperature of the sample inside the cup, T_s^{TC} , was measured with a thermocouple.

1D velocity profiles were measured by a Pulsed Field Gradient Spin Echo (PFG-SE) sequence with a slice thickness of 1 mm in two dimensions,³⁶ echo time $T_E = 19.5$ ms, and $T_R = 2$ s. The duration of the velocity-encoding gradient pulses and their inter-pulse spacing were $\delta = 1$ ms and $\Delta = 13$ ms, respectively. The amplitudes of the velocity-encoding gradients were, respectively in the 500 μm gap and 4 mm gap CC, set to (i) 1.50, 1.19 and 0.14 T m^{-1} for recording shear rates of $\dot{\gamma} = 0.5, 1$ and 8 s^{-1} , or to 0.51 and 0.05 T m^{-1} for recording shear rates of $\dot{\gamma} = 0.5$ and 8 s^{-1} . To avoid chemical-shift artefacts, a CHEmical Shift Selective (CHESS) suppression module, as implemented by Nikolaeva *et al.*,³⁷ was used in all measurements using three 90° chemically selective pulses with bandwidth of 0.8 kHz. The offset was set to 1 kHz or

0.1 kHz respectively for measurements at shear rates of $\dot{\gamma} = 0.5$ and 8 s^{-1} at room temperature or at shear rate of $\dot{\gamma} = 1 \text{ s}^{-1}$ under variable temperature conditions. Different offsets were used due to the presence of water in the water channels giving rise to an additional MR signal thus altering the spectrometer's reference frequency in the temperature-controlled studies. The frequency-encoding read gradient provided a 10 mm-long slice over 1024 pixels, such that the spatial resolution was $\Delta x = 10 \text{ }\mu\text{m}$. The time needed to obtain a single velocity profile within the gap was 34 min for a number of scans of $NS = 512$. Three replicate measurements were collected at each rotation speed.

2.4. Results and discussion

2.4.1. Mechanical stability of the bob

Our previous measurement of the off-axis displacement of the bob in a commercially available 1 mm rheo-MRI CC yielded wobbling values up to $\sim 60\text{--}80 \text{ }\mu\text{m}$ at low rotation rates, where wobbling is most significant (see Fig. S2.1 in section 2.6). Such wobbling size would be excessive in our sub-mm gap setup, resulting in $\sim 16\%$ variation in the gap size during rheo-MRI measurements. Furthermore, during the off-axis movement of the bob under shear, the sheared fluid is pushed sideways within the gap, thus resulting in additional artefactual flow components. The consequent distortions that appear in the velocity profiles hamper the analysis of the underlying 'true' flow behavior, thus making the identification of flow effects such as cooperativity even more challenging. COMSOL simulations of the effect of the off-axis displacement by $80 \text{ }\mu\text{m}$ on the expected linear velocity profiles of a Newtonian fluid flowing in a $500 \text{ }\mu\text{m}$ gap CC yield up to 50% deviation from the expected linear velocity (see Fig. S2.2 in section 2.6 for an experimental velocity profile with an effect of $\sim 60 \text{ }\mu\text{m}$ off-axis displacement of the bob). If the off-axis displacement is reduced down to about $10 \text{ }\mu\text{m}$, such deviation becomes only 5%, which is within the experimental error associated with rheo-MRI flow measurements (see Fig. S2.2 in section 2.6). Such improved off-axis mechanical stability also enables achieving a spatial MRI resolution of $10 \text{ }\mu\text{m}$ with the $500 \text{ }\mu\text{m}$ CC, which in turn is desired to record the velocity profiles with a sufficient number of data points. Hence, reducing the off-axis wobble to below $10 \text{ }\mu\text{m}$ is of importance for both (i) minimizing the artefacts in the velocity profiles, and (ii) avoiding having to discard the signal from pixels close to the bob because of the wobbling. Below we set out to quantify the improvement in the mechanical stability achieved in our newly-designed sub-mm gap cell.

Figure 2.3 shows ^1H MRI FLASH measurements along both x and y directions of the off-axis displacement of the center of the bob, filled with doped water, with respect to the center of the cup, expressed as a percentage of the gap size w . As indicated in the figure, the movement of the bob was tracked at three positions along the bob's height (z axis). In all three slices, the maximum observed off-axis displacement was within 5% of the gap size and appeared linearly decreasing when going from top to bottom, respectively being equal to 25, 17.5, and 7.5 μm at $z = 8, 16,$ and 22 mm. The error associated with the wobble values, due to the limit of accuracy in the estimation of the bob's and the cup's centers by the circle tracking algorithm, is ± 1 μm at all heights. The lower off-axis wobbling towards the bottom of the bob is due to the fact that (i) the protrusion that fits within the well at the bottom of the cup locally fixes the axis of rotation, and (ii) the probe is fixed at its base, but exhibits mechanical instability in the top part, where it also connects to the shaft and the forces acting on it are the largest.

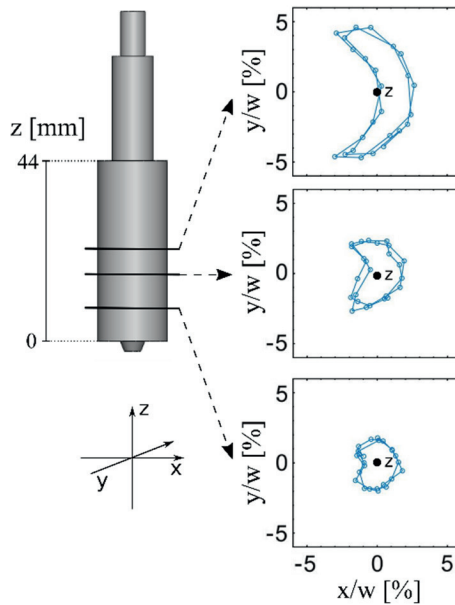


Figure 2.3: Rheo-MRI mapping of the off-axis displacement of the bob, filled with doped water, during rotation at 0.72 rpm. Consecutive FLASH images of 1 mm thick axial slices were measured. 25 images with the duration time of 7 s each were acquired to track 2 full rotations. The position of the center of the bob was extracted from each image using a circle tracking algorithm in MATLAB R2018b. Plots on the right show the coordinates obtained from slices measured at $z = 8, 16,$ and 22 mm along the bob's height, respectively.

The achieved reduction in the off-axis displacement down to $7.5 \mu\text{m}$ ($z = 8 \text{ mm}$) corresponds to a 10-fold improvement in stability as compared to commercially available rheo-MRI CC, and, importantly, is within the minimum desired MRI spatial resolution of $10 \mu\text{m}$ for acquiring velocity profiles in sub-mm gap geometries.

This remarkable improvement in off-axis mechanical stability enables us to use the cell for applying a steady and uni-directional shear, and for obtaining artefact-free velocity profiles even at low shear rates ($\dot{\gamma}$). We believe that the mechanical stability of our rheo-MRI setup can be enhanced even further by improving the stability of the MRI probe head. Based on the observations in Fig. 2.3 we decided to record all our velocity profiles at $z = 10 \text{ mm}$, where the off-axis displacement and its error can be estimated from the linear fit of the measured wobble values as $(9.5 \pm 2) \mu\text{m}$. This position is optimal considering both the stability of the bob and the SNR, which is highest closest to the center of the coil ($z = 14 \text{ mm}$).

2.4.2. Calibration of the temperature control circuit

All applications of temperature-controlled flow studies, *e.g.*, involving crystallization, gelation or polymerization processes, require highly stable and uniform temperature control. Temperature fluctuations can, for instance, lead to inhomogeneities in the sample and/or to flow instabilities.

Here, we have calibrated the temperature of the sub-mm gap CC at seven nominal bath temperature (T_b) values over the range $15\text{--}45 \text{ }^\circ\text{C}$. The temperature was estimated both locally (T_{loc}), from spatially-resolved ^1H CSI spectra of a methanol-filled CC by using Eq. (2.1)³⁵, and as bulk value (T_s^{TC} and T_s^{MRI}), respectively *ex situ* using a thermocouple or *in situ* by averaging the T_{loc} values obtained by ^1H CSI for all pixels from the three selected slices.

Figure 2.4a shows the temperature maps obtained from the ^1H CSI measurements, recorded at $T_b = 45 \text{ }^\circ\text{C}$. It can be seen that the temperature is uniform within each slice and across the z -range examined. A similar observation was obtained for all other T_b values. Thus an *in situ* temperature calibration curve could be constructed, averaging the local sample temperature, T_{loc} , within and over the three slices. Figure 2.4b shows the *ex* and *in situ* calibration curves, both evidencing a linear dependence of the temperature inside the gap. The standard deviation for the *ex* and *in situ* temperature values is $0.3 \text{ }^\circ\text{C}$ and $1 \text{ }^\circ\text{C}$, respectively, mostly due to imperfect shimming typical of wide-bore magnets. The expected temperature fluctuation is estimated to be $0.3 \text{ }^\circ\text{C}$, based on the fluctuations of the thermostat of the water bath. The

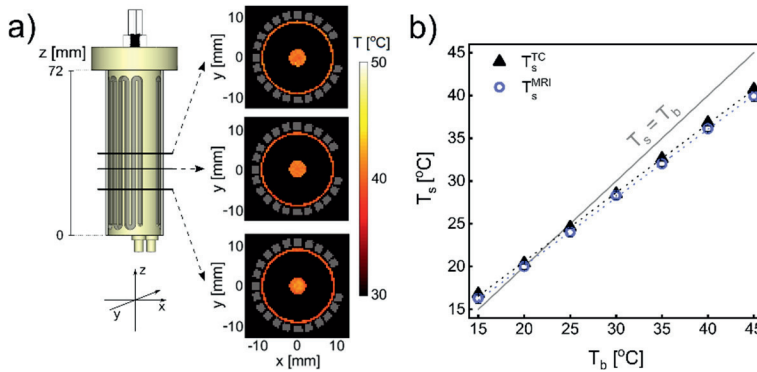


Figure 2.4: Calibrations of the temperature circuit (water channels shown in grey both in the drawing of the cell and in the images), with the cup and the bob filled with CH_3OH . **a)** At $T_b = 45\text{ }^\circ\text{C}$: axial ^1H MR CSI images acquired for three slices, each 1 mm thick, at positions $z = 18, 26$ and 32 mm along the cell's height, showing a uniform temperature, T_{loc} , as calculated using Eq. (2.1). **b)** At $T_b = 15 - 45\text{ }^\circ\text{C}$: effective bulk temperature in the gap, measured ex situ with a thermocouple (T_s^{TC}) and also in situ by ^1H MR CSI (T_s^{MRI}) by averaging the T_{loc} values obtained for the three axial slices shown in a).

embedding of such temperature circuit in the cell enables carrying out rheo-MRI experiments at controlled uniform temperatures within the range $T_s = 16 - 40\text{ }^\circ\text{C}$. This introduces a significant advancement to rheo-MRI, so far mostly limited to room temperature studies.

2.4.3. Case study: local flow behavior of a fat crystal dispersion

As an illustrative application of our novel sub-mm gap rheo-MRI CC, we studied the confined flow behavior of a fat crystal dispersion (FCD), with 27 wt% fat concentration. FCDs are used in production of fat-based products, such as chocolate or margarine. Due to the presence of large crystal aggregates with sizes up to $d = 200\text{ }\mu\text{m}$, these foods are prone to exhibit non-trivial and strongly temperature-dependent flow behavior in sub-mm or mm-sized confinements.^{12,25}

We have first carried out a preliminary investigation of the global flow behavior of the 27 wt% FCD by rheology, at shear rates in the range $\dot{\gamma} = 0.01 - 100\text{ s}^{-1}$, as commonly done to identify shear rates at which flow becomes unstable.⁴ From these measurements (data not reported here) we could observe flow instabilities at and below $\dot{\gamma} = 1\text{ s}^{-1}$. Therefore, we performed rheo-MRI measurements at shear rates above ($\dot{\gamma} = 8\text{ s}^{-1}$) or below ($\dot{\gamma} = 0.5\text{ s}^{-1}$) the transition from unstable to stable flow regimes, and compared the results obtained in the $500\text{ }\mu\text{m}$ and 4 mm gap CCs. We

note that the percentage stress variation across the 500 μm gap CC, calculated as the ratio of stresses at the outer and inner wall, is only 11%,³⁸ which yields linear velocity profiles in the absence of flow instabilities. Hence, flow instabilities can be easily observed from velocity profiles acquired with the sub-mm gap CC. Instead, in mm-gap CCs the non-negligible stress distribution, namely $> 20\%$, may make it impossible to discern and quantify possible effects due to flow cooperativity. Figure 2.5 shows the comparison between the 1D velocity profiles of the 27 wt% FCD at applied shear rates of $\dot{\gamma} = 0.5$ and 8 s^{-1} in the 500 μm (a) and 4 mm (b) gap CC. All measured velocity profiles are compared to the calculated velocity profiles expected for a simple yield-stress fluid in the absence of cooperativity effects. In both geometries, wall slip was quantified by an extrapolation of the last 10 pixels at the outer wall, and subtracted from the velocity profiles, as done in previous work.⁴ Figure 2.5a shows that in the sub-mm gap CC flow of the 27 wt% FCD is linear at $\dot{\gamma} = 8 \text{ s}^{-1}$, with an expected nearly uniform shear rate throughout the gap. In the unstable flow regime, at $\dot{\gamma} = 0.5 \text{ s}^{-1}$, a strongly curved velocity profile is observed, suggesting a spatially-dependent viscosity as also observed in cooperative flow.⁴ In Fig. 2.5b, the experimental velocity profiles for the 4 mm gap CC appear concave at both applied shear rates. The corresponding predicted velocity profiles for a fluid that does not exhibit cooperativity display the same deviation from linearity as experimentally observed

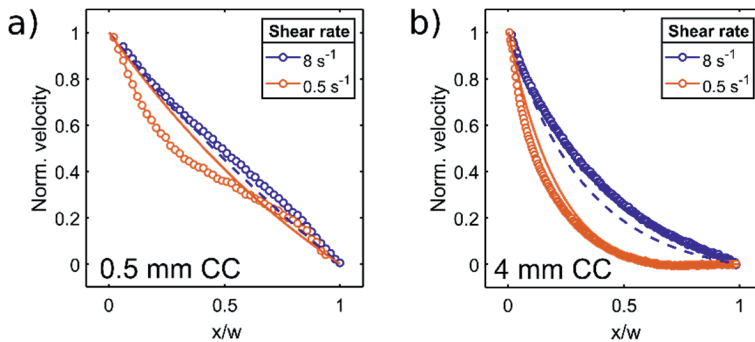


Figure 2.5: Experimental ^1H rheo-MRI velocity profiles (open circles) of a 27 wt% FCD, measured in a) 500 μm gap CC with smooth walls and b) 4 mm gap CC with serrated walls, at $\dot{\gamma} = 8$ and 0.5 s^{-1} , compared with calculated velocity profiles (dashed and solid lines, respectively) of Herschel-Bulkley yield-stress fluid ($4 + 2.54\dot{\gamma}^{0.5}$) without non-local effects, in the respective geometries. At both shear rates, velocities were normalized to the respective maximum velocity. Measured flow profiles were corrected for slippage at the outer wall, by subtracting the slip velocity determined by extrapolation of the last 10 pixels. Slip velocities at the outer wall as a percentage of the maximum expected velocity were 9 and 20% in the 500 μm gap CC, and 5 and 10% for the 4 mm gap CC, at high and low $\dot{\gamma}$ respectively.

for the 27 wt% FCD. This significant effect is solely due to the expected dominant stress variation across the 4 mm gap CC, which in turn makes it impossible to easily unravel flow cooperativity.

For the same 27 wt% FCD sample, we set out to illustrate the importance of temperature-controlled sub-mm rheo-MRI studies. Due to the crystalline nature of the platelets that form the aggregates in the FCD, flow at a temperature higher than room temperature was studied to unravel the influence of recrystallization effects on strongly-confined flow. In Figs. 2.6a and 2.6b the flow behavior at $\dot{\gamma} = 1 \text{ s}^{-1}$ of the 27 wt% FCD is shown at $T_b = 15$ and $30 \text{ }^\circ\text{C}$ respectively, at three shearing times over a 1.5 h time span.

At $T_b = 15 \text{ }^\circ\text{C}$ the confined flow is stable, likely indicating no significant shear-induced recrystallization effects. Concave velocity profiles evidence a non-uniform effective shear rate in agreement with evidences at ambient temperature and low shear rate (see Fig. 2.5). In addition, localized flow measurement enabled the quantification of a constant slip at both cell walls of $(20 \pm 3) \%$. The flow behavior of the dispersion at $T_b = 30 \text{ }^\circ\text{C}$ appears drastically different. The flow exhibits a significant wall slip during the first hour of shearing, with progressively decreasing shear banding effects. In the final 0.5 h, no discrete shear bands could be further distinguished. This indicates that recrystallization takes place, which weakens the structure of the material, causing it to become more susceptible to shear in the final 0.5 h. Additionally, recrystallization results in the formation of larger aggregates, which likely induces cooperativity

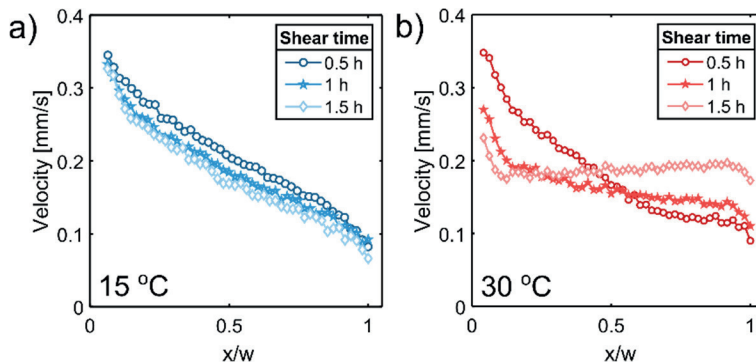


Figure 2.6: Dependence on shearing time (0.5, 1 and 1.5 h) of ^1H rheo-MRI velocity profiles for a 27 wt% FCD, measured at $\dot{\gamma} = 1 \text{ s}^{-1}$ and at a) $T_b = 15 \text{ }^\circ\text{C}$ or b) $T_b = 30 \text{ }^\circ\text{C}$. The flow profiles were acquired consecutively under continuous shear. The duration of each experiment was 0.5 h, with the resulting flow profile being an average measurement over such experiment time.

effects, since a concave, rather than a linear profile is observed in the final 0.5 h. We note that the demonstrated uniformity and stability of the temperature control circuit enables ruling out any possible effect due to temperature fluctuations.

The presence of cooperativity effects in the rheo-MRI results displayed in Fig. 2.5 and 2.6 can be confirmed and quantified by fitting the spatially-resolved velocities in combination with rheological stress measurements.³⁹ This requires separate measurements of bulk and spatially-resolved flow in twin setups.^{9,22,24,40} For reliable quantitative velocimetry studies, the spatially resolved flow profiles must be recorded at high spatial resolution and high SNR, while minimizing mechanical instability artefacts. From Figs. 2.5a and 2.6 it can be seen that such requirements are satisfied with our improved rheo-MRI setup. Thanks to the enhanced off-axis mechanical stability of the bob, acquired velocity profiles are free from wobble artefacts and acquired with very high MRI spatial resolution of 10 $\mu\text{m}/\text{pixel}$. The SNR obtained in the 500 μm gap CC is 120 ± 5 , as given by the ratio of mean signal intensity to the standard deviation of the noise, is comparable to that of wider gap geometries.⁴¹ Here, modelling the confined flow behavior of the FCD would have required accounting for the observed microstructural rearrangements and temperature effects, which was beyond the scope of this work.

2.5. Conclusions

With the aim to study strongly-confined flow by rheo-MRI, we have developed a 500 μm gap rheo-MRI CC, which requires small sample volumes (~ 0.4 ml) and is equipped with a water circuit for temperature control in the range 15 - 40 $^{\circ}\text{C}$. Calibration of the water circuit over this operational temperature range was obtained by performing ^1H CSI measurements of the cell filled with methanol, where the difference in chemical shift between CH_3 and OH signals can be used to quantify sample temperature. This approach revealed a spatially homogeneous temperature, within ± 0.3 $^{\circ}\text{C}$, over the entire sample volume. The mechanical stability of the rotating bob was improved by a factor of ~ 10 with respect to currently available rheo-MRI setups. The MRI spatial resolution could thus be boosted up to ~ 10 μm , the latter value being the estimated reduced size of off-axis wobbling of the bob. All these improved rheo-MRI features were conjointly exploited here to study the temperature-dependent confined flow of a thixotropic 27 wt% FCD sample. By using the sub-mm gap CC, evidences could be observed for (i) the onset of non-uniform flow, suggesting cooperativity effects at low shear rate and room temperature not discernible in

wider gaps, and for (ii) shear-induced microstructural changes at 30 °C, not visible at room temperature and linked to recrystallization effects. We foresee that our improved rheo-MRI setup, suitable for studying strongly confined flow, is a powerful tool for enabling fundamental studies of cooperative flow under *in situ* conditions and, ultimately, for aiding the rational design of foods, or other soft particulate dispersions such as emulsion-based paints or polymer coatings.

Author contributions

Conceptualization: C. T., J. A. D. and J. P. M. v. D.; technical design: J. P.; experimental measurements and data analysis: K. W. M.; validation: K. W. M., M. R. S.; formal analysis: K. W. M.; writing — original draft preparation: K. W. M.; writing — review and editing: M. R. S., C. T., J. A. D. and J. P. M. v. D.; visualization: K. W. M.; supervision: C. T., J. P. M. v. D., J. A. D. All authors have read and agreed to the published version of the manuscript.

Acknowledgements

We thank Bruker BioSpin (Germany) for co-sponsoring this project, and Dieter Gross and Thomas Oerther from Bruker BioSpin for useful discussions on the rheo-MRI setup. We also thank Ruud den Adel (Unilever) for preparation and useful discussion on FCD. C.T. acknowledges funding from the 4TU Precision Medicine program supported by High Tech for a Sustainable Future (https://www.4tu.nl/en/news/!/393/awarding_hightech/).

References

- (1) Fischer, P.; Windhab, E. J. Rheology of food materials, *Curr. Opin. Colloid Interface Sci.* **2011**, *16* (1), 36-40.
- (2) Galvosas, P.; Brox, T. I.; Kuczera, S. Rheo-NMR in food science—Recent opportunities, *Magn. Reson. Chem.* **2019**, *57* (9), 757-765.
- (3) Coussot, P. Progress in rheology and hydrodynamics allowed by NMR or MRI techniques, *Exp. Fluids* **2020**, *61* (9).
- (4) de Kort, D. W.; Veen, S. J.; Van As, H.; Bonn, D.; Velikov, K. P.; van Duynhoven, J. P. M. Yielding and flow of cellulose microfibril dispersions in the presence of a charged polymer, *Soft Matter* **2016**, *12* (21), 4739-4744.
- (5) Brox, T. I.; Douglass, B.; Galvosas, P.; Brown, J. R. Observations of the influence of Taylor-Couette geometry on the onset of shear-banding in surfactant wormlike micelles, *J. Rheol.* **2016**, *60* (5), 973-982.
- (6) Al-kaby, R. N.; Jayaratne, J. S.; Brox, T. I.; Codd, S. L.; Seymour, J. D.; Brown, J. R. Rheo-NMR of transient and steady state shear banding under shear startup, *J. Rheol.* **2018**, *62* (5), 1125-1134.
- (7) Nikolaeva, T.; den Adel, R.; Velichko, E.; Bouwman, W. G.; Hermida-Merino, D.; Van As, H.; Voda, A.; van Duynhoven, J. P. M. Networks of micronized fat crystals grown under static conditions, *Food Funct.* **2018**, *9* (4), 2102-2111.

- (8) Nikolaeva, T.; den Adel, R.; van der Sman, R.; Martens, K. J. A.; Van As, H.; Voda, A.; van Duynhoven, J. P. M. Manipulation of Recrystallization and Network Formation of Oil-Dispersed Micronized Fat Crystals, *Langmuir* **2019**, *35* (6), 2221-2229.
- (9) Goyon, J.; Colin, A.; Bocquet, L. How does a soft glassy material flow: finite size effects, non local rheology, and flow cooperativity, *Soft Matter* **2010**, *6* (12), 2668-2678.
- (10) Kamrin, K. Non-locality in Granular Flow: Phenomenology and Modeling Approaches, *Front. Phys.* **2019**, *7* (116).
- (11) Bocquet, L.; Colin, A.; Ajdari, A. Kinetic Theory of Plastic Flow in Soft Glassy Materials, *Phys. Rev. Lett.* **2009**, *103* (3), 036001.
- (12) Campos, R.; Marangoni, A. G. Crystallization Dynamics of Shear Worked Cocoa Butter, *Cryst. Growth Des.* **2014**, *14* (3), 1199-1210.
- (13) Rohart, A.; Sieffermann, J.-M.; Michon, C. Effect of micro-gel shape and concentration on sensory perception of micro-gels-enriched stirred yoghurts, *Colloids Surf. A: Physicochem. Eng.* **2015**, *475*, 94-102.
- (14) Santiago, J. G.; Wereley, S. T.; Meinhart, C. D.; Beebe, D. J.; Adrian, R. J. A particle image velocimetry system for microfluidics, *Exp. Fluids* **1998**, *25* (4), 316-319.
- (15) Salmon, J. B.; Bécu, L.; Manneville, S.; Colin, A. Towards local rheology of emulsions under Couette flow using Dynamic Light Scattering, *Eur. Phys. J. E* **2003**, *10* (3), 209-221.
- (16) Callaghan, P. T. Rheo-NMR and velocity imaging, *Curr. Opin. Colloid Interface Sci.* **2006**, *11* (1), 13-18.
- (17) Hollingsworth, K. G.; Johns, M. L. Rheo-nuclear magnetic resonance of emulsion systems, *J. Rheol.* **2004**, *48* (4), 787-803.
- (18) Macosko, C. W. *Rheology: Principles, Measurements and Applications*, 1st ed.; John Wiley & Sons, 1994.
- (19) Nikolaeva, T.; Vergeldt, F. J.; Serial, R.; Dijkman, J. A.; Venema, P.; Voda, A.; van Duynhoven, J. P. M.; Van As, H. High Field MicroMRI Velocimetric Measurement of Quantitative Local Flow Curves, *Anal. Chem.* **2020**, *92* (6), 4193-4200.
- (20) Geraud, B.; Bocquet, L.; Barentin, C. Confined flows of a polymer microgel, *Eur. Phys. J. E* **2013**, *36* (3), 1-13.
- (21) Meeker, S. P.; Bonnacaze, R. T.; Cloitre, M. Slip and flow in pastes of soft particles: Direct observation and rheology, *J. Rheol.* **2004**, *48* (6), 1295-1320.
- (22) Derzsi, L.; Filippi, D.; Mistura, G.; Pierno, M.; Lulli, M.; Sbragaglia, M.; Bernaschi, M.; Garstecki, P. Fluidization and wall slip of soft glassy materials by controlled surface roughness, *Phys. Rev. E* **2017**, *95* (5), 052602.
- (23) Andrade, D. E. V.; Ferrari, M.; Coussot, P. The liquid regime of waxy oils suspensions: A magnetic resonance velocimetry analysis, *J. Non-Newton. Fluid Mech.* **2020**, *279*, 104261.
- (24) Paredes, J.; Shahidzadeh, N.; Bonn, D. Wall slip and fluidity in emulsion flow, *Phys. Rev. E* **2015**, *92* (4), 042313.
- (25) Acevedo, N. C.; Block, J. M.; Marangoni, A. G. Critical laminar shear-temperature effects on the nano- and mesoscale structure of a model fat and its relationship to oil binding and rheological properties, *Faraday Discuss.* **2012**, *158*, 171-194.
- (26) Tran, T.; Ghosh, S.; Rousseau, D. Spheroidal Fat Crystal Microstructures Formed with Confined Gap Shearing, *Cryst. Growth Des.* **2014**, *14* (12), 6383-6390.
- (27) Klemm, D.; Heublein, B.; Fink, H.-P.; Bohn, A. Cellulose: Fascinating Biopolymer and Sustainable Raw Material, *Angew. Chem. Int. Ed.* **2005**, *44* (22), 3358-3393.
- (28) Mohammadigoushki, H.; Muller, S. J. A flow visualization and superposition rheology study of shear-banding wormlike micelle solutions, *Soft Matter* **2016**, *12* (4), 1051-1061.
- (29) Aral, B. K.; Kalyon, D. M. Effects of temperature and surface roughness on time-dependent development of wall slip in steady torsional flow of concentrated suspensions, *J. Rheol.* **1994**, *38* (4), 957-972.

- (30) Banerjee, S.; Bhattacharya, S. Food Gels: Gelling Process and New Applications, *Crit. Rev. Food Sci. Nutr.* **2012**, *52* (4), 334-346.
- (31) Mishra, K.; Dufour, D.; Windhab, E. J. Yield Stress Dependent Foaming of Edible Crystal-Melt Suspensions, *Cryst. Growth Des.* **2020**, *20* (2), 1292-1301.
- (32) Ramel, P. R.; Campos, R.; Marangoni, A. G. Effects of Shear and Cooling Rate on the Crystallization Behavior and Structure of Cocoa Butter: Shear Applied During the Early Stages of Nucleation, *Cryst. Growth Des.* **2018**, *18* (2), 1002-1011.
- (33) Velichko, E.; Tian, B.; Nikolaeva, T.; Koning, J.; van Duynhoven, J. P. M.; Bouwman, W. G. A versatile shear cell for investigation of structure of food materials under shear, *Colloids Surf. A: Physicochem. Eng.* **2019**, *566*, 21-28.
- (34) Laryea, E.; Schuhardt, N.; Guthausen, G.; Oerther, T.; Kind, M. Construction of a temperature controlled Rheo-NMR measuring cell – Influence of fluid dynamics on PMMA-polymerization kinetics, *Microporous Mesoporous Mater.* **2018**, *269*, 65-70.
- (35) Ammann, C.; Meier, P.; Merbach, A. A simple multinuclear NMR thermometer, *J. Magn. Reson.* **1982**, *46* (2), 319-321.
- (36) Callaghan, P. T. Rheo-NMR: nuclear magnetic resonance and the rheology of complex fluids, *Rep. Prog. Phys.* **1999**, *62* (4), 599-670.
- (37) Serial, M. R.; Nikolaeva, T.; Vergeldt, F. J.; van Duynhoven, J. P. M.; van As, H. Selective oil-phase rheo-MRI velocity profiles to monitor heterogeneous flow behavior of oil/water food emulsions, *Magn. Reson. Chem.* **2019**, *57* (9), 766-770.
- (38) de Kort, D. W.; Nikolaeva, T.; Dijkman, J. A. In *Modern Magnetic Resonance*, Webb, G. A.; Springer International Publishing, 2018, pp 1589-1608.
- (39) Goyon, J.; Colin, A.; Ovarlez, G.; Ajdari, A.; Bocquet, L. Spatial cooperativity in soft glassy flows, *Nature* **2008**, *454*, 84-87.
- (40) Jop, P.; Mansard, V.; Chaudhuri, P.; Bocquet, L.; Colin, A. Microscale Rheology of a Soft Glassy Material Close to Yielding, *Phys. Rev. Lett.* **2012**, *108* (14), 148301.
- (41) Ovarlez, G.; Rodts, S.; Ragouilliaux, A.; Coussot, P.; Goyon, J.; Colin, A. Wide-gap Couette flows of dense emulsions: Local concentration measurements, and comparison between macroscopic and local constitutive law measurements through magnetic resonance imaging, *Phys. Rev. E* **2008**, *78* (3), 036307.

2.6. Supplementary information

Figure S2.1 shows the positions of the centers of the bob during rotation within the commercially available 1 mm gap CC and the in-house developed 0.5 mm gap CC, demonstrating the off-axis displacements. Figure S2.2 shows the effect of the off-axis bob wobble on a velocity profile of a Newtonian fluid, resulting in artefactual negative velocities and deviations from linearity.

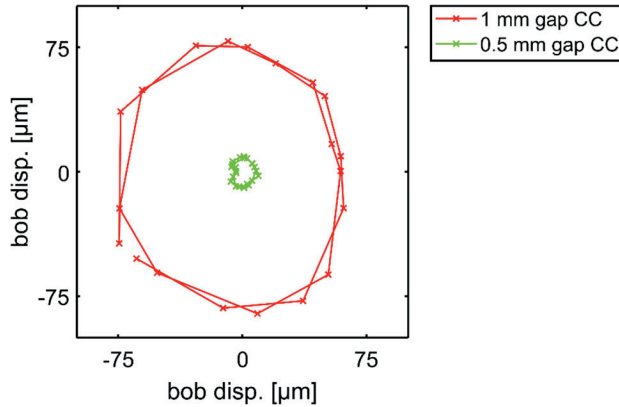


Figure S2.1: Comparison of the off-axis displacement of the bob during rotation at 0.72 rpm in a commercially MRI compatible available 1 mm gap CC and the in-house developed 500 μm gap CC. The bob was filled with doped water and consecutive FLASH images of axial slices were measured. A total of 25 images with the acquisition time of 7 s each were acquired to track 2 full rotations of the bob. The position of the bob's center was extracted from each image using a circle tracking algorithm (MATLAB R2018b).

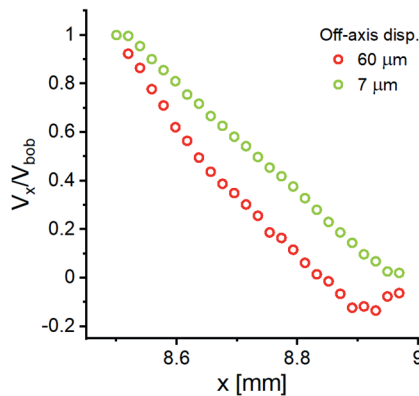


Figure S2.2: Effect of an off-axis displacement of the bob of $\sim 60 \mu\text{m}$ and $\sim 7 \mu\text{m}$ during rotation at 0.72 rpm on an experimental MRI velocity profile of water in a 500 μm gap CC with an old bob design and in the improved bob design, respectively.

CHAPTER

3

Quantifying cooperative flow of fat crystal dispersions

This chapter was published as:

Milc, K. W.; Dijksman, J. A.; van Duynhoven, J. P. M.; Terenzi, C. Quantifying cooperative flow of fat crystal dispersions, *Soft Matter*, **2022**, *18* (14), 2782-2789.

Abstract

We quantify the cooperative flow behavior of fat crystal dispersions (FCDs) upon varying crystallization conditions. The latter enabled altering the multiscale microstructure of the FCDs, ranging from the nanometer-sized platelets and the dispersed fractal aggregates up to the strength of the mesoscopic weak-link network. To the goal of characterizing strongly-confined flow in these optically-opaque materials, we acquire high-resolution rheo-magnetic-resonance-imaging (rheo-MRI) velocimetry measurements using an in-house developed 500 μm gap Couette cell (CC). We introduce a numerical fitting method, based on the fluidity model, which yields the cooperativity length, ξ , in the narrow-gap CC. FCDs with aggregates sizes smaller than the confinement size by an order of magnitude were found to exhibit cooperativity effects. The respective ξ values diverged at the yield stress, in agreement with the kinetic elastoplastic (KEP) theory. In contrast, the FCD with aggregates sizes in the order of the gap size did not exhibit any cooperativity effect: we attribute this result to the correspondingly decreased mobility of the aggregates. We foresee that our optimized rheo-MRI measurement and fitting analysis approach will propel further similar studies of flow of other multiscale and optically-opaque materials.

3.1. Introduction

Flow through sub-mm geometries of complex dispersions, with particle sizes in the order of tens to hundreds micrometers, occurs during production processes and customer use of foods, cosmetics or paints.¹⁻³ It is well known that, under such strongly-confined conditions, flow of particulate dispersions can become cooperative, due to the onset of spatial coupling between plastic events throughout the system.⁴ As a result, the flowing material is macroscopically fluidized and, thus, exhibits higher velocities and larger spatial heterogeneities of viscosity as compared to theoretical flow predictions in the absence of cooperativity.

Despite many experimental and numerical studies conducted over the last two decades,^{5,6} a quantitative and comprehensive characterization of flow cooperativity is still missing, specifically regarding its dependence on microstructural and confinement properties. Thus, predicting cooperativity effects in fundamental soft matter studies, and in industrial applications of complex fluids, remains an open challenge.⁷⁻¹⁰ To address this, suitable measurement techniques and numerical models must be developed for quantifying and predicting flow cooperativity in non-model, optically-opaque dispersions.

In the pioneering works of Goyon *et al.*^{10,11} and Bocquet *et al.*,¹² a quantitative formalism was introduced, centered around the concepts of fluidity, flow cooperativity and a characteristic length scale, ξ . Since then, cooperativity effects have been quantified, under confined flow conditions, in emulsions,⁸ microgels,¹³ cellulose dispersions, and granular materials.¹⁴ In all these studies, cooperativity lengths were consistently found to be several times larger than the sizes of the microstructural constituents, *e.g.* grains, droplets, or aggregates. Yet, studies of the effect of microstructural properties on the extent of cooperativity have been, thus far, limited to evaluating the dependence on concentration and polydispersity of the dispersed particles. Goyon *et al.*¹⁰ found that, in flowing model emulsions, ξ increased with both concentration and droplet size, while it decreased with increasing polydispersity. Similar results were found by Géraud *et al.*^{13,15} in flowing microgels. Less well established is the influence of flow confinement on cooperativity. In their same study on concentrated model emulsions, Goyon *et al.*¹⁰ found that flow cooperativity was independent of both gap size and wall roughness, while Paredes *et al.*⁸ found that only in rough microchannels flow of emulsions could be described as cooperative, and even as responsible for the apparent wall slip. In agreement with these works, Derzsi *et al.*⁷ observed, both experimentally and

numerically, enhanced cooperativity effects in concentrated model emulsions flowing through geometries with rough walls. Interestingly, in most of the above-mentioned studies, the authors reported stress-independent ξ values, which is in disagreement with numerical simulations based on the KEP theory.¹² The latter predicts that cooperativity lengths diverge as stresses approach the yield stress of the material. Stress-dependent ξ values are reported only in the numerical simulations of granular materials by Kamrin *et al.*⁴, or in the studies of microgels by Géraud *et al.*¹³ Thus far extensive studies were mostly limited to model, optically-transparent fluids with rather simple colloidal structures.^{7,8,10,16} Consequently, the fundamental understanding of flow cooperativity in multiscale, and typically optically-opaque, complex materials remains elusive, hindering reliable predictions of strongly-confined flow in industrial applications.

As an example, strongly-confined flow of FCDs is encountered during the production and consumption of, *e.g.* margarine or chocolate. The flow behavior of FCDs depends on the morphology of the multiscale crystal structure, which in turn is strongly dependent on the crystallization conditions, namely applied shear, cooling rate, and temperature.¹⁷⁻¹⁹ These parameters govern the interplay between fat crystallization and network formation processes, in turn affecting the shape, size and fractal dimension of the crystal aggregates, as well as the strength of the interstitial network. The latter has been established to be in the weak-link regime.^{20,21} Thus far, the flow of FCDs with varying microstructural properties has been studied only in geometries with cm-sized gaps, exceeding the sizes of crystal aggregates by at least two orders of magnitude, while the respective sub-mm confined flow behavior and the potential presence of cooperativity effects have never been addressed.^{17,19}

In this work, we study the sub-mm flow of three 27 wt% FCD samples prepared at different crystallization rates, yielding different crystal aggregate sizes, fractal dimensions and strength of the interstitial weak-link network. These microstructural properties were respectively characterized, under static conditions, using light microscopy, wide- and small-angle X-ray diffraction (WAXD and SAXD), ultra-small-angle X-ray scattering (USAXS), and Raman imaging. We study the global flow behavior in both wide- and narrow-gap CCs with classical rheology, and compare the results with spatially-resolved rheo-MRI velocimetry measurements using an in-house developed CC with 500 μm gap.²² We find that the presence and spatial extent of cooperative flow depends on the microstructural changes induced by varying crystallization rates. By fitting the data to a numerical fluidity-based model adapted

for narrow-gap CC, we show that the flow cooperativity length depends not only on the size of the fat crystal aggregates, but also on the inter-particle interactions mediated by the colloidal network.

3.2. Materials and methods

3.2.1. Sample preparation

The solid fat blend was mixed with a commercially available sunflower oil (SF) to give a 27 wt% fat-in-oil dispersion, which was heated at 50 °C for 20 min to erase crystal polymorphic history. For each sample, the melt was subjected to a distinct crystallization procedure, to obtain samples with varying microstructures. For an isothermal crystallization (IC) the melt was transferred to a vessel pre-set to 15 °C, yielding an approximate cooling rate of 5 °C/min. For rapid crystallization (RC) and slow crystallization (SC), the melt was cooled to 20 °C at a rate respectively of 1 or 0.1 °C/min. Using the crystallization rates and temperatures as labels, we henceforth refer to the above mentioned samples as **IC(15)**, **RC(1)** and **SC(0.1)**, respectively. All measurements were carried out on 27 wt% FCD samples at room temperature (RT) within 8 h from the completion of their crystallization process, with the exception of USAXS, which was carried out within 3 days of chilled storage and transport since the crystallization.

3.2.2. WAXD

A Bruker D8-Discover diffractometer with a Vântec 500 2D detector and an μ S microfocus X-ray source (CuK α radiation, λ \approx 0.154 nm) was used in a θ/θ configuration. WAXD data were collected in the range of $7^\circ < 2\theta < 55^\circ$. The beam cross section at the sample position was about 1 mm. The distance and angle between detector and sample were 32.5 cm and 10° , respectively.

3.2.3. Polarized Light Microscopy

Optical images of the three samples were obtained using a polarized light microscope (Nikon Eclipse) equipped with a 10x objective lens. The images were acquired with an Olympus DP70 camera and digitalized using a cellSens imaging software. To obtain an estimate of the average crystal aggregate size for each sample, 15 images were acquired at different locations across the measured surface. The mean size and its standard deviation (SD) over 50 randomly chosen aggregates was calculated in ImageJ 1.52.

3.2.4. USAXS and SAXD

USAXS and SAXD measurements were performed at the ID02 beamline at the European Synchrotron Radiation Facility (ESRF) (Grenoble, France). The average crystal thickness was obtained from the first order diffraction peak originating from triglyceride 2L layers using the Scherrer equation.²³ For the determination of the fractal dimension, data processing was conducted in Igor Pro 6.37 software using the Irena SAS 2.57 package. The USAXS signal of the SF oil sample was subtracted before data modelling. The Unified Fit model²⁴ provided the radius of gyration, R_{gi} , and the Porod slope, P_i , from which information about the crystal surface, morphology and the fractal dimension can be extracted. For $P_i < 3$ the fractal dimension equals to and relates to a mass fractal. Otherwise, the fractal dimension can be calculated as $6 - P_i$ and indicates a surface fractal.

3.2.5. Raman imaging

The hyperspectral Raman images were acquired using a WITec confocal Raman (Alpha 300R+) microscope equipped with a Zeiss upright microscope with a 532 nm laser at 25.0 mW, using a 100×/0.9 objective. The Raman spectrometer was coupled to a cooled (−60 °C) EMCCD detector. The obtained Raman spectra were in the range of 100 – 3800 cm^{-1} . An integration time of 0.05 s was used for imaging a 150 × 150 μm area with a resolution of 1 μm . The raw data were subjected to standard corrections, namely the cosmic ray removal and background subtraction in the Project FIVE 5.2 software after which the true component analysis was performed using the Raman spectra of the pure components to obtain the spatial distribution of solid fat and liquid oil in the three samples.

3.2.6. Rheology

All rheometric measurements were performed using an Anton Paar (MCR 301) rheometer. Global flow curves were acquired using a standard stainless steel CC with the diameter of the bob, $r_i = 5.25$ mm, and the diameter of the cup, $r_o = 8.75$ mm. Sandpaper was glued to the surface of both bob and cup to prevent slip. Each sample was pre-sheared for 3 min at 30 s^{-1} and, thereafter, exposed to stress measurements under a shear rate sweep from 100 s^{-1} to 0.01 s^{-1} . A total of 20 points per decade in shear rate were recorded, averaging each stress value over 5 s. Confined flow measurements were carried out using an in-house constructed CC made of polyether ether ketone (PEEK) with the radii of the bob and the cup, $r_i = 8.5$ mm and $r_o = 9$ mm,

respectively. This CC is identical to the one used in rheo-MRI measurements in order to ensure comparability of the results.

3.2.7. Rheo-MRI

Rheo-MRI velocimetry measurements were performed on a wide-bore Bruker Avance III spectrometer operating at 7 T. Excitation and detection of the ^1H signal was performed with a bird-cage radiofrequency coil with an inner diameter of 25 mm, in the standard microimaging gradient system Micro 2.5 (Bruker Biospin) with maximum gradient intensity of 1.5 T m^{-1} along all three axes. The magnet was equipped with the standard Bruker rheo-MRI accessory, consisting of a stepper motor and drive shaft, used in combination with a custom-made 500 μm CC ($r_i/r_o = 8.5/9 \text{ mm}$) with smooth walls.²²

1D velocity profiles were measured using a Pulsed Field Gradient Spin Echo (PFG-SE)²⁵ sequence, within a slice 1 mm thick along two dimensions, echo time $T_E = 20 \text{ ms}$ and repetition time $T_R = 2 \text{ s}$. The duration of the velocity-encoding gradient pulses, and their inter-pulse spacing, were $\delta = 1 \text{ ms}$ and $\Delta = 13 \text{ ms}$, respectively. To avoid chemical-shift artefacts, a CHEMical Shift Selective (CHESS) suppression module, as implemented by Serial *et al.*,²⁶ was used in all measurements using three 90° chemically selective pulses with bandwidth of 0.8 kHz and offset of 1.1 kHz. The frequency-encoding read gradient provided a 10 mm-long slice over 1024 pixels, such that the spatial resolution was $\Delta x = 10 \mu\text{m}$. Using a number of scans, $NS = 512$, the total measurement time per velocity profile was 34 min. Each measurement was carried out on a fresh sample batch.

3.3. Results and discussion

3.3.1. Multiscale Structure

From the melt, 27 wt% FCDs were prepared by isothermal crystallization at $15 \text{ }^\circ\text{C}$ (**IC(15)**) and by rapid and slow crystallization at 1 or $0.1 \text{ }^\circ\text{C}/\text{min}$, here denoted as **RC(1)** and **SC(0.1)**, respectively. Irrespective of the applied cooling regime, all fat crystals in the 27 wt% FCDs are in the β' polymorphic form, as evidenced by the presence of strong diffraction peaks at 19.5 and $23.4 \text{ } 2\theta$ in WAXD spectra (see Fig. S3.1a in section 3.5.1).²⁷ The different crystallization rates did, however, affect the sizes of the crystal aggregates, yielding samples with aggregates ranging across two orders of magnitude in size, and with varying polydispersity, as shown in the polarized light micrographs in Fig. 3.1. The isothermal crystallization at $15 \text{ }^\circ\text{C}$ yielded a sample with

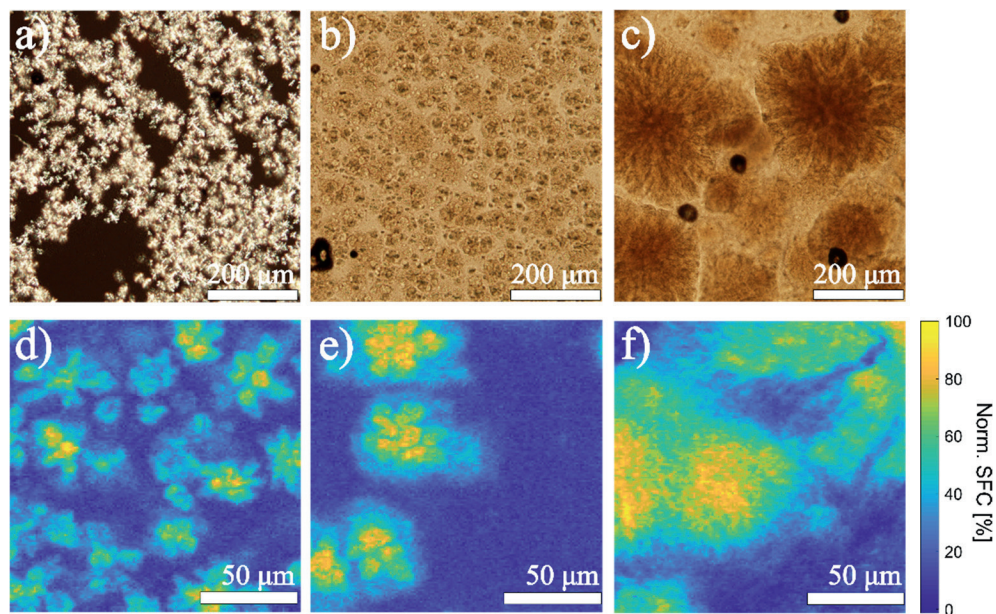


Figure 3.1: Images of the 27 wt% FCD samples **IC(15)** (left), **RC(1)** (middle) and **SC(0.1)** (right) obtained by polarized light microscopy (top) or Raman imaging (bottom). The images were acquired at RT within 3 h after completion of the crystallization process.

aggregates' mean diameter of $30 \pm 13 \mu\text{m}$ (**IC(15)**), while crystallization rates of 1 and $0.1 \text{ }^\circ\text{C}/\text{min}$ towards $20 \text{ }^\circ\text{C}$ resulted in dispersions with respective aggregates' mean diameters of $53 \pm 12 \mu\text{m}$ (**RC(1)**), and $223 \pm 119 \mu\text{m}$ (**SC(0.1)**). This trend is in line with studies on microstructures of model and real fat systems crystallized under varying conditions of temperature and shear.²⁸⁻³¹ According to the established theories on crystallization mechanisms in FCDs, lower crystallization rates lead to persistent lower degree of undercooling, resulting in a decrease of nucleation rate and thus larger crystallites. The crystallites then aggregate into fractal networks.³² The increase in crystallite size with decreasing crystallization rates was confirmed by SAXD measurements, which yielded the average crystallite thickness of $54.0 \pm 0.3 \text{ nm}$, $60.0 \pm 0.3 \text{ nm}$ and $80.0 \pm 0.3 \text{ nm}$ for samples **IC(15)**, **RC(1)** and **SC(0.1)**, respectively. The fractal nature of the aggregates was confirmed by the USAXS measurements, with the quantified fractal dimensions for samples **IC(15)**, **RC(1)** and **SC(0.1)** respectively of 2.90 ± 0.03 , 2.70 ± 0.03 and 2.40 ± 0.01 (see Fig. S3.1b in section 3.5.1). The lowest fractal dimension for sample **SC(0.1)** is in line with the porous and spherulitic appearance of the crystal aggregates visible in the micrograph in Fig. 3.1c. To gain further insight into the structure and the colloidal network

beyond the crystal aggregates, we investigated the spatial distribution of solid fat in the three samples with Raman imaging, with results presented in Figs. 3.1d – f. As expected, in all samples the solid fat is concentrated within the aggregates. However, the analysis of the Raman spectra (see Fig. S3.2 in section 3.5.1) corresponding to voxels within interstitial spaces revealed an increasing similarity with the reference spectrum of the pure solid fat component of the FCDs, going from sample **IC(15)** to **SC(0.1)**. Both the spatially-resolved Raman spectroscopy and SAXD measurements evidence that the weak-link network in the **IC(15)** and **RC(1)** samples has a lower solid fat content and is composed of thinner crystal platelets. In contrast, in the **SC(0.1)** sample more solid fat is present in the weak-link network, composed of less space filling, thicker crystallites.

3.3.2. Flow characterization

The flow of the FCDs is typically studied globally and described with a local constitutive rheological law, which is insensitive to flow confinement size.^{19,21,33} To test whether such theoretical approach is sufficient to capture all aspects of flow of the 27 wt% FCDs we study and compare the global and local flow of each sample, using classical rheology and sub-mm rheo-MRI, respectively.

3.3.3. Global flow

The global flow behavior of samples **IC(15)**, **RC(1)** and **SC(0.1)** under strain-controlled conditions in a 3.5 mm gap CC is shown in Figs. 3.2a – c (black circles) as measurements of shear stress, σ , at varying shear rates, $\dot{\gamma}$, in the range $0.01 - 100 \text{ s}^{-1}$. The data appear independent of the microstructural differences across the samples, and can be well described by the Herschel-Bulkley (HB) model: $\sigma = \sigma_y + K\dot{\gamma}^n$. Here, σ_y denotes the yield stress, K is a proportionality constant with the units of $\text{Pa} \cdot \text{s}^{1/n}$ and n is a dimensionless power law index.³⁴ The fitted parameters obtained for the three samples are summarised in Table 3.1. In section 3.5.2 we include a verification that the wide gap condition, with the intrinsic shear and stress inhomogeneity, does not affect our results.

Table 3.1: Fitting parameters obtained from fitting analysis of the global flow curves of the three 27 wt% FCDs using the HB model.

	σ_y [Pa]	K [Pa s ^{1/n}]	n
IC (15 °C)	13.7 ± 0.2	3.1 ± 0.1	0.70 ± 0.01
RC (1 °C/min)	17.3 ± 0.2	4.4 ± 0.1	0.67 ± 0.01
SC (0.1 °C/min)	12.6 ± 0.1	4.1 ± 0.1	0.67 ± 0.01

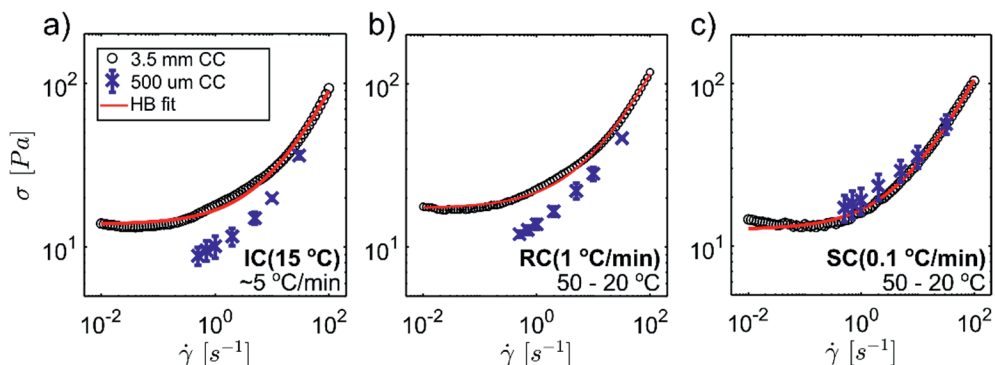


Figure 3.2: Global flow curves of the 27 wt% FCD samples **IC(15)** (a), **RC(1)** (b), and **SC(0.1)** (c) measured with a rheometer, starting from high shear rates, using a standard 3.5 mm gap CC with glued sandpaper to prevent slip (open circles). Each flow curve was fitted with a HB model (solid red line). Stress values at chosen shear rates were also measured with a 500 μ m gap CC with smooth walls (blue crosses). The plotted values are the mean and the SD of two repeats.

To investigate whether the measured global flow behavior depends on the size of the flow geometry, we measured the global stress responses of the three 27 wt% FCDs in a 500 μ m gap CC at chosen shear rates of $\dot{\gamma} = 0.5, 0.7, 1, 2, 5, 10$ and 30 s^{-1} (blue crosses in Figs. 3.2a – c). Comparison between results obtained with the 500 μ m and 3.5 mm gap CCs shows that flow in sample **SC(0.1)**, where aggregate sizes are the largest, is independent of the gap size (Fig. 3.2c). However, for the other two samples the global stress is markedly lower in the narrow-gap CC. The presence of a gap-size dependence of the rheological properties for samples **IC(15)** and **RC(1)** can arise from various sources of flow instability, such as shear banding,³⁵ wall slip,⁸ and/or cooperative flow behavior.¹¹ To elucidate the source of the bulk rheological properties observed in Fig. 3.2, local flow information is needed. Thus, in the next section we study the confined flow in a spatially-resolved manner by rheo-MRI.

3.3.4. Local flow

The local flow behavior was studied by high-field rheo-MRI using an in-house developed 500 μ m gap CC. This cell was designed to enable imposing confined flow while keeping both stress inhomogeneity and off-axis wobbling negligible.²² These conditions are essential for observing and quantifying confined flow behavior, without distortions originating from the rotating geometry. The rheo-MRI velocity profiles of all 27 wt% FCDs, acquired at the same shear rates as the stress measurements by standard rheology (Fig. 3.2), are shown in Figs. 3.3a – c. Local shear

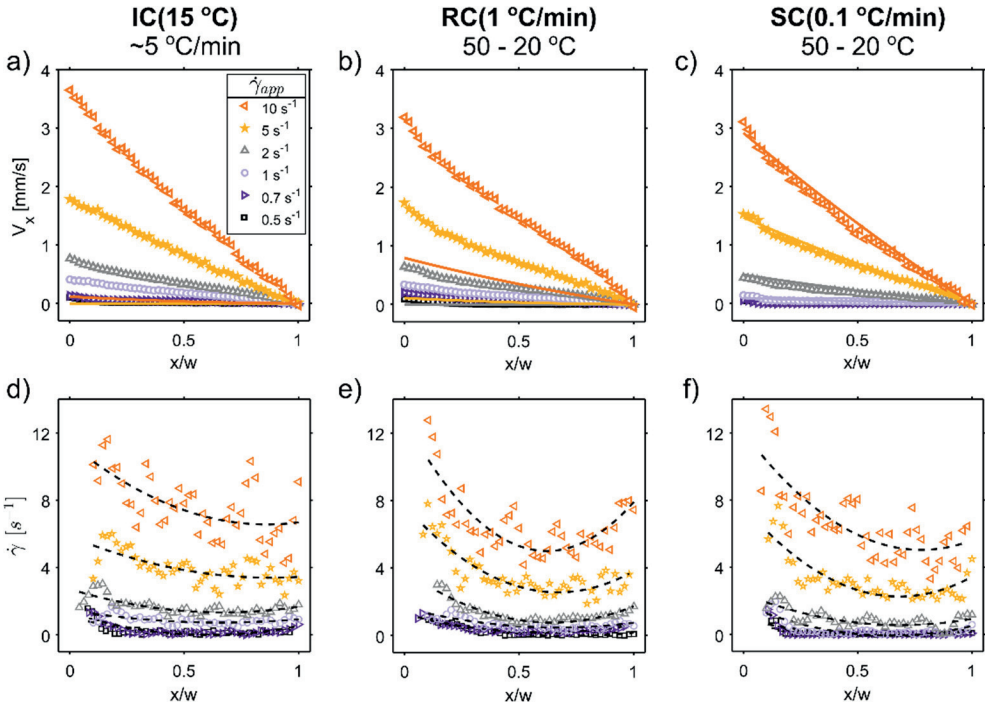


Figure 3.3: For the 27 wt% FCD samples **IC(15)**, **RC(1)** and **SC(0.1)**, from left to right: a) – c) ^1H rheo-MRI velocity profiles measured in a $500\ \mu\text{m}$ gap CC (open symbols) and respective calculated velocities from the HB model (solid lines) as a function of the normalized position across the gap, upon varying applied shear rates, $\dot{\gamma}_{app}$. Measured flow profiles were corrected for slippage by subtracting the slip velocity (see section 3.5.3) determined by extrapolation of the last 10 pixels at the outer wall as done in previous work; d) – f) corresponding shear rates calculated from each measured velocity profile. The dotted line serves as a guide for the eye.

rates, shown in Figs. 3.3d – f, were derived from each of the measured velocity profiles using the following equation:

$$\dot{\gamma}(x) = \frac{\partial v(x)}{\partial x} - \frac{v(x)}{x}, \quad (3.1)$$

where x is the measured position across the gap and $v(x)$ is the respective spatially-dependent velocity. As $\dot{\gamma}(x)$ values are proportional to the first spatial derivative of $v(x)$, they are expected to better unravel sample-specific deviations from linear flow profiles. It can be seen in Figs. 3.3a – c that all samples exhibit non-linear velocity profiles and, thus, non-uniform local shear rates (Figs. 3.3d – f). Furthermore, for samples **IC(15)** and **RC(1)**, shear banding can be observed only at the lowest $\dot{\gamma}_{app}$

value, while flow in sample **SC(0.1)** bands over $\dot{\gamma}_{app}$ values up to 1 s^{-1} (Fig. 3.3c). Similarly, the percentage of wall slip, averaged across all $\dot{\gamma}_{app}$ values (see Fig. S3.4 in section 3.5.3), is 35% for **IC(15)** and **RC(1)**, but decreases to 47% for **SC(0.1)**, indicating a markedly distinct behavior of the latter sample. With the aim to describe this complex flow behavior, we compare the measured rheo-MRI velocity profiles with those calculated from the global HB flow behavior (solid lines in Figs. 3.3a – c). We find that only for sample **SC(0.1)** the measured velocities are in agreement with the predictions from the HB equation, while for samples **IC(15)** and **RC(1)** they largely exceed the predicted velocities at all shear rates. Hence, our narrow-gap rheo-MRI measurements indicate (i) the failure of the local HB flow model, and the existence of enhanced velocities, for the 27 wt% FCDs prepared at high crystallization rates, and (ii) the presence of shear-banding and shear-dependent wall slip. In literature, such flow instabilities have been associated with confinement-induced cooperativity effects.^{8,10,11,15} Thus, in the following section we describe and use a non-local rheological model, suitable for the adopted narrow-gap CC, to quantify flow cooperativity for samples **IC(15)** and **RC(1)**.

3.3.5. Characterization of flow cooperativity

Cooperativity effects in the flow of soft particle dispersions can be quantified using a so-called fluidity model. Fluidity, defined as the ratio of the shear rate and the shear stress, namely $f = \dot{\gamma}/\sigma$, is linked, on a microscopic level, to the local rate of plastic rearrangements across the whole flowing system. If the material exhibits cooperative flow, the plastic rearrangements have non-local character, *i.e.* they induce further rearrangements of neighbouring particles and lead to complex spatio-temporal variations of the fluidity. In this case, the fluidity is predicted to obey a non-local equation:

$$f(x) = f_{bulk} + \xi^2 \frac{\partial^2 f(x)}{\partial x^2}, \quad (3.2)$$

where f_{bulk} is the bulk fluidity in the absence of non-local effects, ξ is the cooperativity length, which can be interpreted as the distance over which plastic events at one site influence spatial rearrangements of neighboring particles, and x is the position across the gap. For our samples, whose global flow is well described by the HB model (see Fig. 3.2), the bulk fluidity is defined as:

$$f_{bulk} = \begin{cases} \frac{1}{\sigma} \left(\frac{\sigma - \sigma_y}{K} \right)^{1/n} & \sigma > \sigma_y \\ 0 & \sigma < \sigma_y, \end{cases} \quad (3.3)$$

where $\sigma = \frac{T}{2\pi Hr_i^2}$ is the stress distribution specific to the CC geometry. The latter expression is derived from the momentum balance, where T is the torque exerted on the rotating bob measured at a rheometer, and H is the height of the bob.³⁶ Given the form of the stress distribution in a CC, Eq. 3.2 has no closed, analytical solution. Hence, to obtain the cooperativity lengths for each sample at varying shear rates, we numerically solve the following system of first-order ordinary differential equations (ODEs), with the shear rates at both inner and outer walls, respectively $\dot{\gamma}_{ri}$ and $\dot{\gamma}_{ro}$, as boundary conditions:

$$\begin{aligned} \frac{\partial}{\partial x} \left(\frac{\dot{\gamma}_{loc}}{\sigma} \right) &= Y_2 \\ \frac{\partial Y_2}{\partial x} &= \frac{1}{\xi^2} \left[\frac{\dot{\gamma}_{loc} - \dot{\gamma}_{bulk}}{\sigma} \right], \end{aligned} \quad (3.4)$$

where $\dot{\gamma}_{loc}$ is the local shear rate obtained from rheo-MRI measurements (Figs. 3.3d – f). We note that our proposed numerical approach for solving the fluidity equation enables easily adapting the model to different flow geometries with radial symmetry, by simply defining the expression of the stress distribution. The stress distribution, along with the definition of bulk fluidity, becomes instead a constraining factor in the commonly used analytical integrations of the fluidity equation,^{8,10,13} making the model less general and straightforward. The solution of Eq. 3.4 is numerically integrated to obtain a theoretical velocity profile, which we fit to the measured data using the boundary conditions and ξ as fitting parameters. To achieve a robust estimate of all fitting parameters, in particular of the boundary conditions which rely on the derivative of the velocity profiles, high spatial resolution in the measured data is a key requirement. This condition is satisfied in our experimental data, where a spatial resolution of 10 $\mu\text{m}/\text{pixel}$ could be achieved thanks to our improved design of the new rheo-MRI setup with boosted mechanical stability of the rotating elements.^{37,38}

In Figs. 3.4a and 3.4b the experimental velocity profiles, respectively for samples **IC(15)** and **RC(1)** and displayed also in Figs. 3.3a and 3.3b, are fitted using the fluidity model. In section 3.5.3 we include the fitting results using the bulk flow behavior corrected for the shear rate inhomogeneity of a wide gap geometry. We also attempted fitting the model to the velocity profiles of sample **SC(0.1)**, which yielded

either no convergence or cooperativity lengths below the mean particle size (see Fig. S3.5 in section 3.5.3), further confirming the absence of cooperativity in this 27 wt% FCD sample. For samples **IC(15)** and **RC(1)** the mean cooperativity lengths were obtained, at each shear rate, as an average fitting result from triplicate measurements (Figs. 3.4c and 3.4d). The calculated mean ξ values were weighed using the fitting error of each repeat, while the error bars represent the maximum and the minimum ξ value obtained from fitting the individual measurements (see Fig. S3.6 in section 3.5.3 for plots of the other fitting parameters, $\dot{\gamma}_{ri}$ and $\dot{\gamma}_{ro}$). First, we observe that the obtained numerical solutions of Eq. 3.4 are in agreement with the measured velocity profiles, and that all obtained ξ values are in the order of the

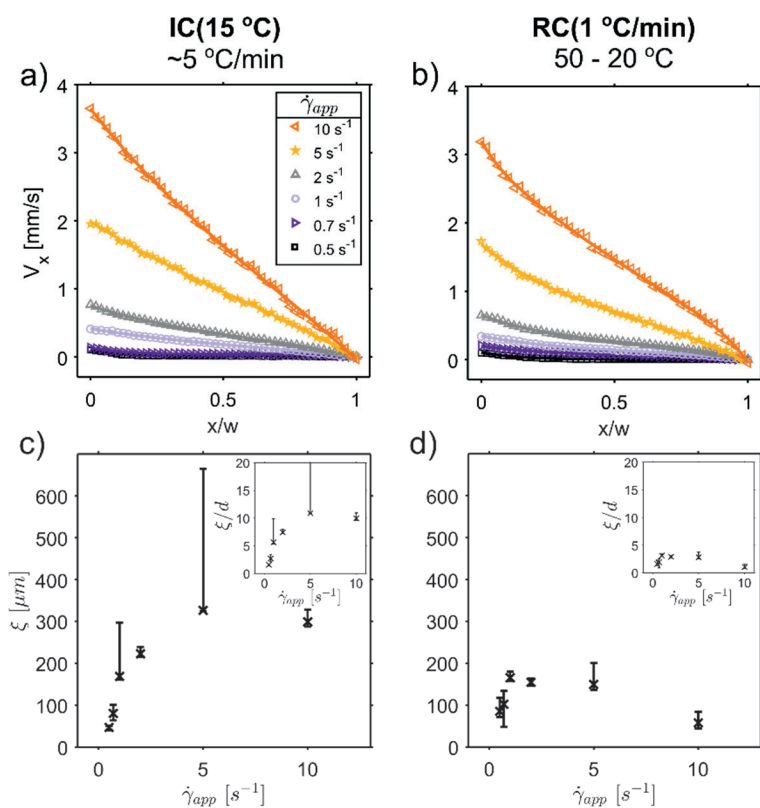


Figure 3.4: For samples **IC(15)** (a and c) and **RC(1)** (b and d): experimental and fitted velocity profiles (top row) and mean cooperativity lengths, ξ , (bottom row) obtained using Eqs. 3.2 and 3.3. The mean ξ values were obtained from three replicate rheo-MRI measurements per $\dot{\gamma}_{app}$ and calculated using the individual fitting errors as weights. The error bars represent the spread of the ξ values. Insets report the obtained ξ values normalized to the respective mean aggregate size, d .

aggregate sizes in the 27 wt% FCD samples. This is in agreement with the current understanding of flow cooperativity, and in line with findings from previous studies.^{8,10,15} Interestingly, we observe a decrease in the cooperativity length with increasing aggregate sizes, reaching a null cooperativity length in sample **SC(0.1)**, characterized by the largest aggregates. The different flow behavior of the examined 27 wt% FCDs likely originates from the difference among these samples in terms of mesoscopic weak-link network and aggregates' fractality. We hypothesize that in the **IC(15)** and **RC(1)** samples, the inter-particle weak-link network favors the onset of cooperative flow. Instead, the coarser interstitial network, higher fractality, and mean size of the aggregates of the **SC(0.1)** sample result in excessive confinement condition, hindering the mobility of the aggregates under shear. This severely limits the inter-particle interactions in the **SC(0.1)** sample, resulting in the absence of cooperativity effects. A similar hypothesis was made by Géraud *et al.* in their study on cooperative flow of microgels.¹³

Lastly, Figs. 3.4c and 3.4d unravel a non-monotonic trend of the ξ values as a function of the applied shear rate. This trend is in agreement with the KEP model,¹² which suggests that the cooperativity length should diverge at the yield stress of the material, according to the following equation:

$$\xi(\sigma) = C \times \sqrt{\frac{1 + H(\sigma_y - \sigma)}{|\sigma - \sigma_y|}} \times d, \quad (3.5)$$

where C is a dimensionless scaling constant, and d is the characteristic length scale of the fluid microstructure, which here we assume to be the determined mean aggregate sizes and their respective SD. In Fig. 3.5 we show the theoretical cooperativity lengths as a function of stress over a range relevant for samples **IC(15)** and **RC(1)**. The ξ values were calculated using either the respective mean sizes of the aggregates, namely 30 and 53 μm (solid lines), or the corresponding minimum and maximum values calculated as $(30 \pm 13) \mu\text{m}$ and $(53 \pm 12) \mu\text{m}$ (dotted lines). We compare these predictions with the ξ values obtained from the fitted velocity profiles (cross symbols in Fig. 3.4), plotted in Fig. 3.5 against the stress values measured in the 500 μm CC by classical rheology (Fig. 3.2). Although the theoretical and fitted ξ values are not in perfect agreement, it is clear that for both **IC(15)** and **RC(1)** samples ξ reaches a maximum around the corresponding yield stress value.

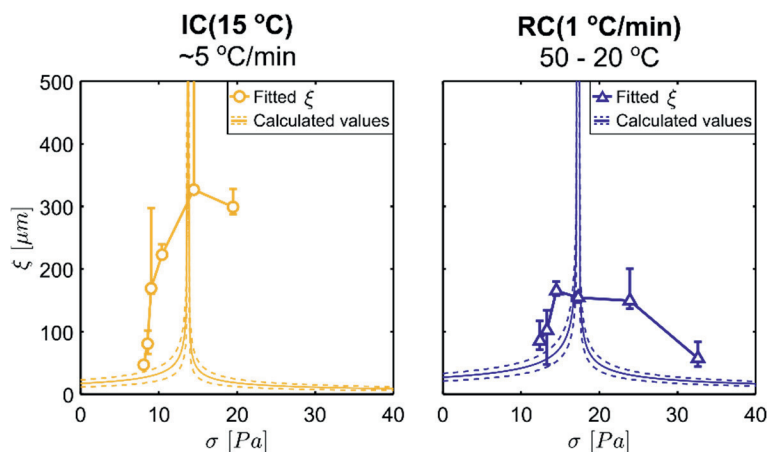


Figure 3.5: Theoretical ξ values predicted by the KEP model for samples **IC(15)** and **RC(1)** (solid lines) at stresses 1 – 40 Pa, compared with the mean cooperativity lengths, ξ obtained from fits of the fluidity model, plotted against stresses at the bob, measured by global rheology. Dotted lines are the calculated ξ values for smallest and largest aggregates present in each sample, given the respective polydispersity.

3.4. Conclusions

In this work, we have studied the flow behavior of three 27 wt% FCDs, prepared at different crystallization rate conditions, in both sub-mm and wide gap CCs. The examined 27 wt% FCDs had average crystal aggregate sizes in the range of 10 – 10² μm and varying colloidal network properties. We have found that the flow of the 27 wt% FCD sample with the largest crystal aggregates is independent of the confinement size, and is well described by a classical rheological HB model. In contrast, the flow of the 27 wt% FCDs with smaller crystal aggregates was sensitive to the confinement size, yielding lower stress values in sub-mm confinement than in a wide-gap CC. With the sub-mm rheo-MRI CC measurements, we identified cooperativity as the underlying cause of the observed differences in the confined flow between the 27 wt% FCDs. By fitting the measured velocity profiles with our proposed numerical fluidity model, we have quantified the cooperativity length scale, ξ , for samples **IC(15)** and **RC(1)**. The found ξ values were 1 – 15 times larger than the respective mean aggregates' sizes, in line with previous findings.^{8,10,15} In addition, ξ values were found to be dependent on the applied shear rate, diverging at the samples' yield stress, in agreement with theoretical predictions obtained with the KEP model. Finally, sample **IC(15)**, with smallest aggregates and lowest polydispersity, respectively ~30 μm and 40%, exhibited the highest ξ values at

medium shear rates. In contrast, sample **SC(0.1)**, with largest aggregates and highest polydispersity, respectively $\sim 200 \mu\text{m}$ and 50%, did not exhibit any cooperativity effects, which we attribute to the decreased mobility of the aggregates, caused by the high fractality and large sizes approximating the confinement size.

Thanks to the optimized narrow-gap rheo-MRI setup and the developed numerical modelling approach, we were able to characterize confined flow of the 27 wt% FCDs, and to quantify the dependence of its cooperative flow on the adopted crystallization conditions. The obtained results show that the cooperativity length does not necessarily scale with particle size. We foresee that our proposed experimental and modelling approach can be used to aid elucidating the dependence of cooperativity on other structural or rheological properties of FCDs, such as particle concentration and shape, confinement size and wall slip. This will ultimately aid in robustly predicting flow cooperativity in FCDs, and other industrially-relevant structured fluids, under varying flow conditions.

Author Contributions

Conceptualization: C. T., J. A. D. and J. P. M. v. D.; experimental measurements and data analysis: K. W. M.; validation: K. W. M.; formal analysis: K. W. M.; writing — original draft preparation: K. W. M.; writing — review and editing: C. T., J. A. D. and J. P. M. v. D.; visualization: K. W. M.; supervision: C. T., J. P. M. v. D, J. A. D. All authors have read and agreed to the published version of the manuscript.

Acknowledgements

We thank Bruker BioSpin (Germany) for co-sponsoring this project, and Dieter Gross and Thomas Oerther from Bruker BioSpin for useful discussions on the rheo-MRI setup. We thank John Philippi for the design of the rheo-MRI CC. We also acknowledge: Brian Tighe (TU Delft), for fruitful discussions on numerical modelling and data interpretation; Theyencheri Narayanan and Michael Sztucki, for support during experiments on the ID02 beamline at ESRF; Ruud van Adel, for help with the analysis of WAXD, SAXD and USAXS spectra; Arjen Bader, for help with the acquisition of Raman spectra. We acknowledge the support of NWO for the MAGNEFY centre, which is part of the uNMR-NL national facility. The USAXS experiments were performed at the European Synchrotron Radiation Facility (ESRF), Grenoble, France. C.T. acknowledges funding from the 4TU Precision Medicine Program supported by High Tech for a Sustainable Future (https://www.4tu.nl/en/news/!/393/awarding_hightech/).

References

- (1) Corrieu, G.; Béal, C. In *Reference Module in Food Science*, Smithers, G.; Elsevier, 2016, pp 617-624.
- (2) Sun, J.; Zhou, W.; Huang, D. In *Reference Module in Food Science*, Smithers, G. W.; Elsevier, 2018, pp 1-9.
- (3) Xu, L.; Gu, L.; Su, Y.; Chang, C.; Wang, J.; Dong, S.; Liu, Y.; Yang, Y.; Li, J. Impact of thermal treatment on the rheological, microstructural, protein structures and extrusion 3D printing characteristics of egg yolk, *Food Hydrocoll.* **2020**, *100*, 105399.
- (4) Kamrin, K.; Koval, G. Nonlocal Constitutive Relation for Steady Granular Flow, *Phys. Rev. Lett.* **2012**, *108* (17), 178301.
- (5) Dijkstra, J. A. Connecting the Drops: Observing Collective Flow Behavior in Emulsions, *Front. Phys.* **2019**, *7* (198).
- (6) Kamrin, K.; Henann, D. L. Nonlocal modeling of granular flows down inclines, *Soft Matter* **2015**, *11* (1), 179-185.
- (7) Derzsi, L.; Filippi, D.; Mistura, G.; Pierno, M.; Lulli, M.; Sbragaglia, M.; Bernaschi, M.; Garstecki, P. Fluidization and wall slip of soft glassy materials by controlled surface roughness, *Phys. Rev. E* **2017**, *95* (5), 052602.
- (8) Paredes, J.; Shahidzadeh, N.; Bonn, D. Wall slip and fluidity in emulsion flow, *Phys. Rev. E* **2015**, *92* (4), 042313.
- (9) de Kort, D. W.; Veen, S. J.; Van As, H.; Bonn, D.; Velikov, K. P.; van Duynhoven, J. P. M. Yielding and flow of cellulose microfibril dispersions in the presence of a charged polymer, *Soft Matter* **2016**, *12* (21), 4739-4744.
- (10) Goyon, J.; Colin, A.; Bocquet, L. How does a soft glassy material flow: finite size effects, non local rheology, and flow cooperativity, *Soft Matter* **2010**, *6* (12), 2668-2678.
- (11) Goyon, J.; Colin, A.; Ovarlez, G.; Ajdari, A.; Bocquet, L. Spatial cooperativity in soft glassy flows, *Nature* **2008**, *454*, 84-87.
- (12) Bocquet, L.; Colin, A.; Ajdari, A. Kinetic Theory of Plastic Flow in Soft Glassy Materials, *Phys. Rev. Lett.* **2009**, *103* (3), 036001.
- (13) Geraud, B.; Bocquet, L.; Barentin, C. Confined flows of a polymer microgel, *Eur. Phys. J. E* **2013**, *36* (3), 1-13.
- (14) Kamrin, K. Non-locality in Granular Flow: Phenomenology and Modeling Approaches, *Front. Phys.* **2019**, *7* (116).
- (15) Géraud, B.; Jørgensen, L.; Ybert, C.; Delanoë-Ayari, H.; Barentin, C. Structural and cooperative length scales in polymer gels, *Eur. Phys. J. E* **2017**, *40* (5), 1-10.
- (16) Seth, J. R.; Locatelli-Champagne, C.; Monti, F.; Bonnecaze, R. T.; Cloitre, M. How do soft particle glasses yield and flow near solid surfaces?, *Soft Matter* **2012**, *8* (1), 140-148.
- (17) Nikolaeva, T.; den Adel, R.; van der Sman, R.; Martens, K. J. A.; Van As, H.; Voda, A.; van Duynhoven, J. P. M. Manipulation of Recrystallization and Network Formation of Oil-Dispersed Micronized Fat Crystals, *Langmuir* **2019**, *35* (6), 2221-2229.
- (18) Marangoni, A. G.; Rogers, M. A. Structural basis for the yield stress in plastic disperse systems, *Appl. Phys. Lett.* **2003**, *82* (19), 3239-3241.
- (19) Nikolaeva, T.; den Adel, R.; Velichko, E.; Bouwman, W. G.; Hermida-Merino, D.; Van As, H.; Voda, A.; van Duynhoven, J. P. M. Networks of micronized fat crystals grown under static conditions, *Food Funct.* **2018**, *9* (4), 2102-2111.
- (20) Narine, S. S.; Marangoni, A. G. Fractal nature of fat crystal networks, *Phys. Rev. E* **1999**, *59* (2), 1908-1920.
- (21) Marangoni, A. G.; van Duynhoven, J. P. M.; Acevedo, N. C.; Nicholson, R. A.; Patel, A. R. Advances in our understanding of the structure and functionality of edible fats and fat mimetics, *Soft Matter* **2020**, *16* (2), 289-306.

- (22) Milc, K. W.; Serial, M. R.; Philippi, J.; Dijkstra, J. A.; van Duynhoven, J. P. M.; Terenzi, C. Validation of temperature-controlled rheo-MRI measurements in a submillimeter-gap Couette geometry, *Magn. Reson. Chem.* **2022**, *60* (7), 606-614.
- (23) den Adel, R.; van Malssen, K.; van Duynhoven, J. P. M.; Mykhaylyk, O. O.; Voda, A. Fat Crystallite Thickness Distribution Based on SAXD Peak Shape Analysis, *Eur. J. Lipid Sci. Technol.* **2018**, *120* (9), 1800222.
- (24) Peyronel, F.; Ilavsky, J.; Mazzanti, G.; Marangoni, A. G.; Pink, D. A. Edible oil structures at low and intermediate concentrations. II. Ultra-small angle X-ray scattering of in situ tristearin solids in triolein, *J. Appl. Phys.* **2013**, *114* (23), 234902.
- (25) Callaghan, P. T. Rheo-NMR: nuclear magnetic resonance and the rheology of complex fluids, *Rep. Prog. Phys.* **1999**, *62* (4), 599-670.
- (26) Serial, M. R.; Nikolaeva, T.; Vergeldt, F. J.; van Duynhoven, J. P. M.; van As, H. Selective oil-phase rheo-MRI velocity profiles to monitor heterogeneous flow behavior of oil/water food emulsions, *Magn. Reson. Chem.* **2019**, *57* (9), 766-770.
- (27) D'Souza, V.; deMan, J. M.; deMan, L. Short spacings and polymorphic forms of natural and commercial solid fats: A review, *J. Am. Oil Chem. Soc.* **1990**, *67* (11), 835-843.
- (28) Maleky, F.; Acevedo, N. C.; Marangoni, A. G. Cooling rate and dilution affect the nanostructure and microstructure differently in model fats, *Eur. J. Lipid Sci. Technol.* **2012**, *114* (7), 748-759.
- (29) Kaufmann, N.; De Graef, V.; Dewettinck, K.; Wiking, L. Shear-induced Crystal Structure Formation in Milk Fat and Blends with Rapeseed Oil, *Food Biophys.* **2012**, *7* (4), 308-316.
- (30) Liang, B.; Shi, Y.; Hartel, R. W. Correlation of Rheological and Microstructural Properties in a Model Lipid System, *J. Am. Oil Chem. Soc.* **2008**, *85* (5), 397-404.
- (31) Campos, R.; Narine, S. S.; Marangoni, A. G. Effect of cooling rate on the structure and mechanical properties of milk fat and lard, *Food Res. Int.* **2002**, *35* (10), 971-981.
- (32) Peyronel, F.; Acevedo, N. C.; Pink, D. A.; Marangoni, A. G. In *Crystallization of Lipids*, Sato, K.; Wiley, 2018, pp 143-181.
- (33) Acevedo, N. C.; Block, J. M.; Marangoni, A. G. Critical laminar shear-temperature effects on the nano- and mesoscale structure of a model fat and its relationship to oil binding and rheological properties, *Faraday Discuss.* **2012**, *158*, 171-194.
- (34) Herschel, W. H.; Bulkley, R. Konsistenzmessungen von Gummi-Benzollösungen, *Kolloid-Zeitschrift* **1926**, *39* (4), 291-300.
- (35) Lerouge, S.; Olmsted, P. D. Non-local Effects in Shear Banding of Polymeric Flows, *Front. Phys.* **2020**, *7* (246), 1-11.
- (36) McKelvey, J. M. *Polymer Processing*; Wiley: New York, 1962, p 106 - 108.
- (37) Coussot, P.; Raynaud, J.; Bertrand, F.; Moucheront, P.; Guilbaud, J.; Huynh, H.; Jarny, S.; Lesueur, D. Coexistence of Liquid and Solid Phases in Flowing Soft-Glassy Materials, *Phys. Rev. Lett.* **2002**, *88* (21), 218301.
- (38) Hollingsworth, K. G.; Johns, M. L. Rheo-nuclear magnetic resonance of emulsion systems, *J. Rheol.* **2004**, *48* (4), 787-803.

3.5. Supplementary information

3.5.1. Multiscale structure characterization

Figure S3.1 shows the results of WAXD and USAXS measurements, performed to determine the polymorphic form of the crystal platelets and the fractal dimension of the aggregates, respectively.

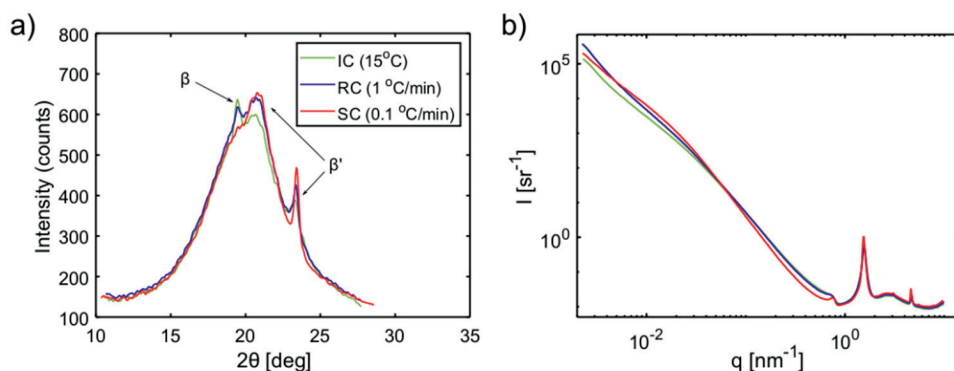


Figure S3.1: a) WAXD spectra of the three 27 wt% FCD samples evidencing the β' polymorphic form of the aggregate-forming crystal platelets, for all crystallization rates; b) USAXS intensity, I , as a function of scattering vector, q , with the obtained Porod slope, P_i of 3.1, 3.3 and 2.4 for the 27 wt% FCD samples **IC(15)** (green), **RC(1)** (blue) and **SC(0.1)** (red), respectively.

Figure S3.2 shows the Raman spectra for the 27 wt% FCD samples, acquired in the interstitial spaces between the aggregates, in comparison with the spectrum of a sample consisting solely of the solid fat component of the FCDs. An increase in the intensity of the signals at Raman shifts of 1078 cm^{-1} and 1135 cm^{-1} , and a decrease in intensity of the peak at a shift of 1272 cm^{-1} , evidences an increasing similarity with the spectrum of pure solid fat, going from sample **IC(15)** towards **SC(0.1)**. This indicates an increase in the solid fat content and in the colloidal network strength with decreasing crystallization rate.

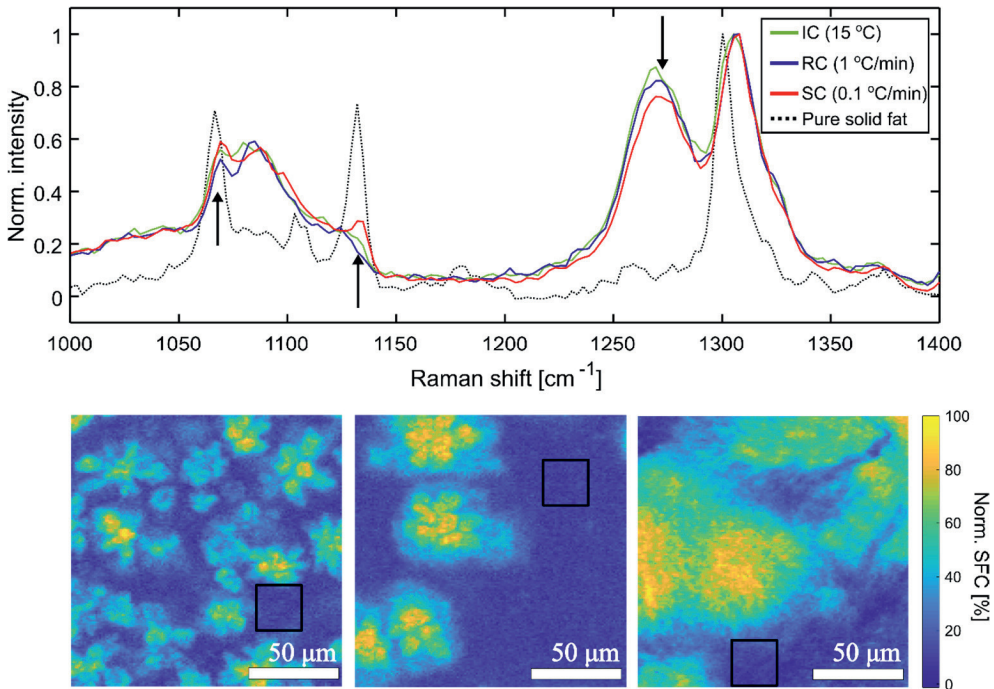


Figure S3.2: Raman spectra (top) of the three 27 wt% FCD samples, resulting from averaging of 625 spectra in the interstitial space of 25 x 25 pixels, from the areas marked with black rectangles in the respective Raman images (bottom) of samples **IC(15)** (left), **RC(1)** (middle) and **SC(0.1)** (right). Spectra of the 27 wt% FCDs are compared with the spectrum of pure solid fat (dotted black line).

3.5.2. Shear rate inhomogeneity in the wide-gap CC

We calibrated the effect of the wide gap condition on the measured stress and shear rate values by acquiring flow curves of a Newtonian fluid, silicone oil, with viscosity, $\eta = 1 \text{ Pa}\cdot\text{s}$ in narrow and wide gap CCs, with respective gap sizes of 0.4 mm and 3.5 mm (data not shown). The calibration yielded an empirical scaling factor of 4 in the applied shear rate, such that $\dot{\gamma}_{\text{narrow}} = 4 \times \dot{\gamma}_{\text{wide}}$.

In Fig. S3.3 we present global flow curves for the three 27 wt% FCDs including the correction in the shear rates. The adjusted wide-gap CC global flow data was fitted with the HB model, with the fitting parameters presented in Table S3.1. Comparing the parameters in Tables S3.1 and Table 3.1 we note that only the proportionality constant, K changed as a result of the shear rate correction.

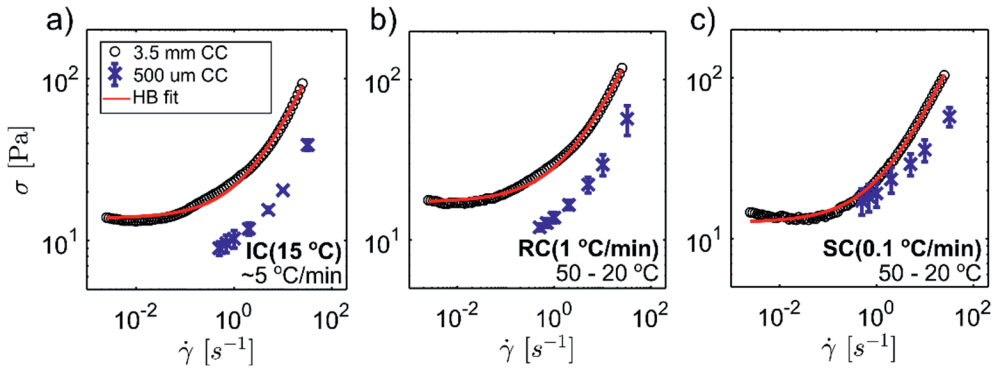


Figure S3.3: Global flow curves of the 27 wt% FCD samples **IC(15)** (a), **RC(1)** (b), and **SC(0.1)** (c) measured with a rheometer, with the stresses acquired in the 3.5 mm gap CC (black circles) plotted against shear rates adjusted for the shear rate inhomogeneity caused by the wide gap condition, according to the calibration performed with a Newtonian fluid.

Table S3.1: Fitting parameters obtained from fitting of the HB model to the global flow curves of the three 27 wt% FCDs adjusted for the shear rate inhomogeneity.

	σ_y [Pa]	K [Pa s ^{1/n}]	n
IC (15 °C)	13.7 ± 0.2	7.3 ± 0.2	0.70 ± 0.01
RC (1 °C/min)	17.3 ± 0.2	10.3 ± 0.2	0.67 ± 0.01
SC (0.1 °C/min)	12.6 ± 0.1	9.7 ± 0.1	0.67 ± 0.01

3.5.3. Local flow behavior of the 27 wt% FCDs

The percentage of slip velocity, v_{slip} , shown in Fig. S3.4, was calculated according to the following equation:

$$v_{slip} = \left(1 - \frac{v_{obs}}{v_{theor}}\right) \times 100 \quad (S3.1)$$

where v_{obs} is the maximum measured velocity and the v_{theor} is the theoretical maximum velocity.

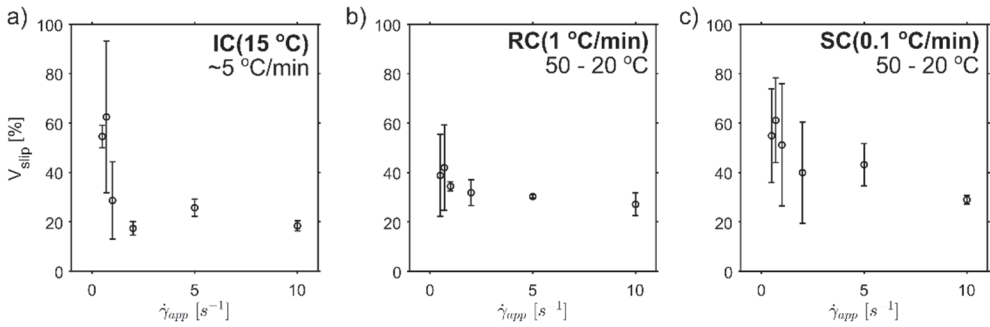


Figure S3.4: Mean value of slip velocity at the inner wall, V_{slip} , vs. $\dot{\gamma}_{app}$, calculated from the rheo-MRI velocity profiles using Eq. (S3.1). The error bars is the standard deviation of V_{slip} over three replicate measurements.

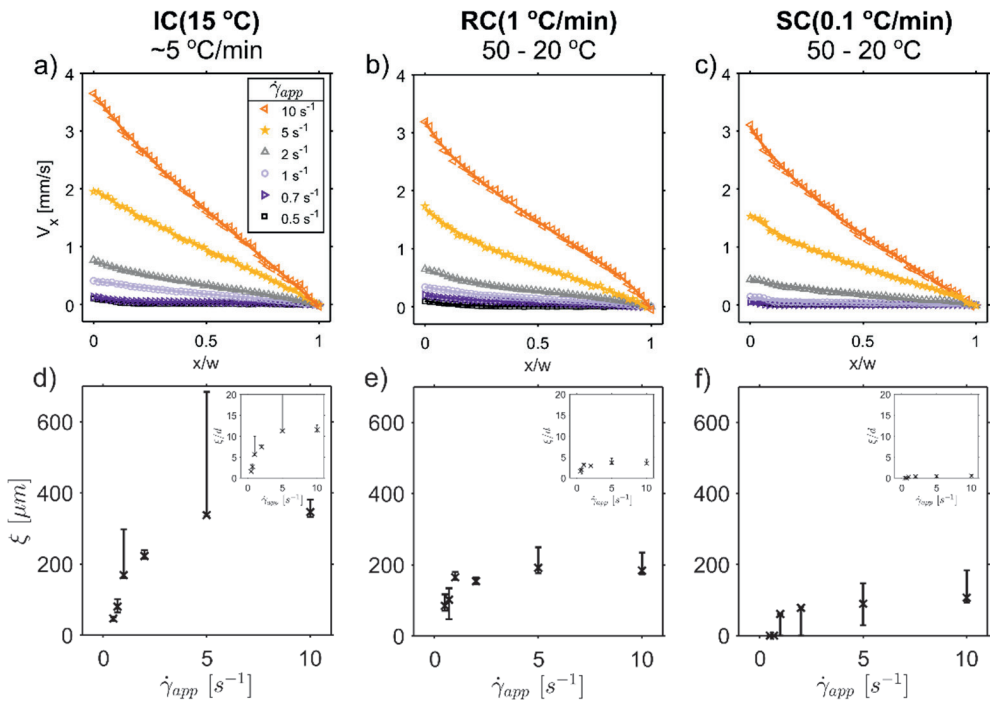


Figure S3.5: For samples **IC(15)** (a and d), **RC(1)** (b and e) and **SC(0.1)** (c and f): experimental and fitted velocity profiles (top row) and mean cooperativity lengths, ξ , (bottom row) obtained from fitting the fluidity model using the bulk flow behavior adjusted for the shear rate inhomogeneity.

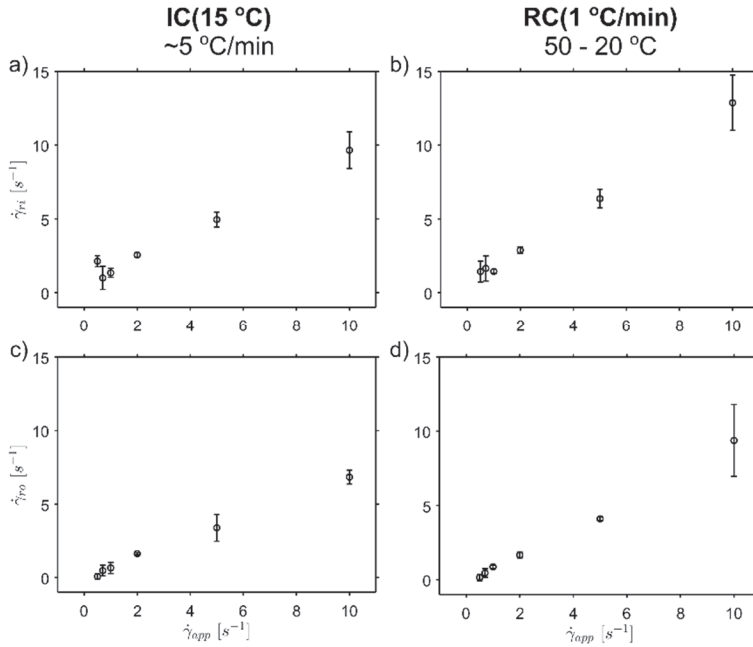


Figure S3.6: Plots of the boundary conditions, namely the shear rate at the bob, $\dot{\gamma}_{ri}$ (top), and at the cup, $\dot{\gamma}_{ro}$ (bottom), vs. $\dot{\gamma}_{app}$ obtained from fitting the fluidity model to the rheo-MRI velocity profiles of samples **IC(15)** (a and c) and **RC(1)** (b and d). The error bars represent the fitting uncertainty.

CHAPTER

4

Capillary flow-MRI: quantifying micron-scale cooperativity in complex dispersions

This chapter was published as:

Milc, K. W.; Oerther, T.; Dijkman, J. A.; van Duynhoven, J. P. M.; Terenzi, C. Capillary flow-MRI: quantifying micron-scale cooperativity in complex dispersions, *Anal. Chem.*, **2023**, *95* (41), 15162-15170.

Abstract

Strongly-confined flow of particulate fluids is encountered in applications ranging from 3D printing to spreading of foods and cosmetics into thin layers. When flowing in constrictions with gap sizes, w , within 10^2 times the mean size of particles or aggregates, d , structured fluids experience enhanced bulk velocities and inhomogeneous viscosities, as a result of so-called cooperative, or non-local, particle interactions. Correctly predicting cooperative flow for a wide range of complex fluids requires high-resolution flow imaging modalities applicable *in situ* to even optically-opaque fluids. To this goal, we here developed a pressure-driven high-field MRI velocimetry platform, comprising of a pressure controller connected to a capillary. Wall properties and diameter could be modified respectively as hydrophobic/hydrophilic, or in size, ranging from $w \sim 100$ - $540 \mu\text{m}$. By achieving a high spatial resolution of $9 \mu\text{m}$, flow cooperativity length scales, ξ , down to $15 \mu\text{m}$ in 0.5 wt% Carbopol with $d \sim 2 \mu\text{m}$, could be quantified by means of established physical models, with an accuracy of 13%. The same approach was adopted for a heterogeneous fat crystal dispersion (FCD) with d and ξ values up to an order of magnitude higher than in 0.5 wt% Carbopol. We found that, for strongly-confined flow of 0.5 wt% Carbopol in the $100 \mu\text{m}$ capillary, ξ is independent of flow conditions. For the 15 wt% FCD, ξ increases with the gap size and with applied pressures over 0.25 – 1 bar. In both samples, non-local interactions span domains up to about 5 – 8 particles, but at the highest confinement degree explored, $\sim 8\%$ for FCD, domains of only ~ 2 particles contribute to cooperative flow. The developed flow-MRI platform is easily scalable to ultra-high field MRI conditions for chemically-resolved velocimetric measurements of, *e.g.*, complex fluids with anisotropic particles undergoing alignment. Future potential applications of the platform encompass imaging extrusion under confinement during 3D printing of complex dispersions and *in vitro* vascular and perfusion studies.

4.1. Introduction

Flow of particulate fluids, such as dispersions and microgels is encountered in daily life and many industrial processes, with examples including squeezing cosmetics out of packings or flow of foods in pipes and nozzles during their production. In many such cases, flow of particulate fluids is well described and can be successfully predicted by global rheological models, such as Herschel-Bulkley (HB).¹⁻⁵ However, complex fluids tend to exhibit flow instabilities such as wall slip⁶ and shear-history dependence in flow, known as thixotropy,⁷ significantly complicating flow modelling. Additionally, the global rheology approach tends to fail in describing the flow behavior under conditions where the flow confinement size, w , is within two orders of magnitude of the average microstructural size of the flowing fluid, d . Such conditions can be encountered in food 3D printing^{8,9} or spreading of cosmetics and paints into thin layers. In such strongly-confined regime, where the degree of confinement, $d/w \geq 1\%$, flow can become cooperative, due to non-local interactions between the flowing particles. This typically leads to an increase in the macroscopic velocity, and to the onset of spatially heterogeneous viscosity, as compared to non-confined flow conditions.¹⁰⁻¹² Thus, accurately predicting strongly-confined flow, accounting for cooperativity effects in non-model or industrially-relevant structured fluids, inherently requires broadly applicable velocimetry techniques with high spatial resolution. Since the first study of flow cooperativity, approximately two decades ago by optical velocimetry measurements, the latter have been used to investigate the dependence of cooperativity on the gap size and wall properties of the flow geometry. Recent work also revealed impact of microstructural properties such as size distribution, concentration, and anisotropy of particles within optically-transparent, colloidal model dispersions.^{11,13-15} Problematically, most structured fluids are optically-opaque, due to the presence of bubbles, droplets or other particles, and thus cannot be measured by optical imaging methods. Under such circumstances, Magnetic Resonance Imaging (MRI) velocimetry can be beneficial, as it does not suffer from this limitation. In recent years, MRI velocimetry has been applied to unravel flow cooperativity in fluids with particles sizes $\geq 30 \mu\text{m}$, like cellulose, fat crystal dispersions (FCDs), and milk microgels, or even in granular materials.¹⁶⁻²¹ These studies were performed using rotational rheo-MRI setups^{22,23} equipped with commercially-available or custom-made²⁴ Couette cells (CC) with gap sizes down to 0.5 mm, or cone-plate (CP) geometries with angles down to 4° . On the one hand, the cylindrical symmetry of the CC geometry lends itself well to MRI measurements, while on the other hand the

stress distribution is approximately homogeneous in a CP geometry. Yet, both geometries possess characteristic limitations which impede their use for wide-range studies of cooperativity. Specifically, downsizing the gap within a CC geometry below 0.5 mm²⁴ is not realistic, due to challenges in the vertical alignment of the concentric cylinders inside the magnet, and in the mechanical stability of the rotating parts²⁴. Conversely, because of the increasing gap size along the radial direction of a CP geometry, imposing a well-defined degree of flow confinement, increasing the imaging slice thickness to achieve higher signal-to-noise ratio (SNR), and shearing dense or heterogeneous structured fluids is a challenge. For both such geometries, modifying wall properties is costly and time-consuming. Furthermore, the CCs and CPs, along with the rheo-MRI drive shafts must be manufactured for specific bore-sizes of MRI magnets, and are currently not available for narrow-bore and/or ultra-high field MRI magnets. All these limitations have thus far prevented broadening the scope of high-field flow-MRI measurements towards micron-scale cooperativity studies. To bridge this gap, in this work, we have developed a capillary flow-MRI platform for translational flow measurements, available with various capillary sizes and wall properties, and easily scalable for use at any magnetic field strength and magnet bore size. These features of the platform broaden the experimental conditions under which cooperative flow can be studied, and also open the possibility to study industrially-relevant processes including extrusion^{25,26} and mixing of multiphase fluids in sub-mm confinements.²⁷

We first demonstrate the validation of the proposed flow-MRI platform by determining the local viscosities of a Newtonian fluid, namely silicone oil, flowing in capillaries with diameters within 100-540 μm . Subsequently, we study the confined flow of two particulate fluids: 0.5 wt% Carbopol and a 15 wt% FCD as a function of the capillary diameter and wall properties. Carbopol, typically containing particle sizes in the order of 1-10 μm ,^{3,14,28} is often used as a model yield stress fluid in rheological studies and, in this work, it enables benchmarking the capability of our approach in estimating cooperativity lengths in a fluid with particle sizes below the spatial MRI resolution. On the other hand, 15 wt% FCDs with crystal aggregates sizes from hundreds nm up to ~ 200 μm in diameter²⁹⁻³² are relevant for the processing of foods, such as margarine or chocolate. With the proposed platform we were able to quantify flow cooperativity over the broad range of particle sizes covered by the two particulate dispersions, with relevance in rheological and industrial applications. We found that in 0.5 wt% Carbopol cooperativity appears independent of strongly-confined flow conditions with only minor effect from wall properties, while in the 15

wt% FCDs, with larger particle sizes, the capillary diameter largely affects the cooperativity length scales. In the final part, we demonstrate that higher stress variation within the flow geometry leads to a decrease of ξ values, by comparing the results obtained with the developed capillary setup and a corresponding CC geometry.

4.2. Materials and methods

4.2.1. Sample preparation

As a model Newtonian fluid, silicone oil, with viscosity $\eta_{25^\circ} = 1 \text{ Pa}\cdot\text{s}$ at 25°C was purchased from Sigma Aldrich and used with no further modifications. As a model yield stress fluid, 0.5 wt% Carbopol was prepared following the procedure described by Géraud *et al.*¹⁴ Carbopol ETD 2050 powder (Lubrizol) was added to milliQ water heated to 50°C , in a ratio to give 0.5 wt% solution, after which the dispersion was stirred for 30 min with a magnetic stirrer at 50°C until a complete dissolution of the powder. The resulting solution was cooled to room temperature (RT), and the pH was adjusted from ~ 3 to 7.0 ± 0.5 , by a dropwise addition of aqueous NaOH (5 M), under continuous stirring. During the neutralization, jamming of the polymer network occurs due to swelling of the polymer blobs with water.²⁸ It is known from literature that the stirring method affects the microstructure.¹⁴ Hence, the resulting arrested gel was stirred with a mixer for 24 h at 2000 rpm at RT to obtain the desired microstructure size of $\sim 3 \mu\text{m}$. After preparation the sample was stored at RT. For preparation of the 15 wt% FCD, a solid fat blend was mixed with a commercially available sunflower oil (SF) to give a 15 wt% fat-in-oil dispersion, which was heated at 50°C for 20 min to erase crystal polymorphic history. Subsequently, the melt was transferred to a vessel pre-set at 15°C for isothermal crystallization over 10 min. A fresh batch of sample was prepared before each experiment and used within 8 h from preparation.

4.2.2. Microstructure determination

The microstructure of 0.5 wt% Carbopol was visualized under a confocal microscope (Nikon Ti2 Eclipse), equipped with a high sensitivity camera (Nikon C2). A drop of 0.5 wt% Carbopol, stained with Rhodamine B, was deposited on a glass slide and examined with an oil objective (60x magnification, NA = 1.4). A laser with a wavelength of $\lambda = 561 \text{ nm}$ was used for excitation with the collected fluorescence bandwidth set to 510 – 593 nm. The microstructure of the 15 wt% FCD was visualized using a polarized light microscope (Nikon Eclipse) equipped with a 10x objective lens.

The images were acquired with an Olympus DP70 camera and digitalized using a cellSens imaging software. The mean sizes of the polymer blobs in 0.5 wt% Carbopol and of the crystal aggregates in the 15 wt% FCD sample were obtained from the Intensity Correlation Spectroscopy approach, as described in detail by Géraud *et al.*¹⁴ The 2D autocorrelation function of micrographs of both samples was calculated and radially averaged. The resulting exponential decay was fitted with the following equation:

$$g(r) = g_0 \exp\left(-\left(\frac{r}{r_0}\right)^\alpha\right) + g_\infty, \quad (4.1)$$

where r_0 is the correlation length, an equivalent of particle radius, g_0 is the peak intensity and g_∞ is the background intensity.

4.2.3. μ CT measurements

The glass capillaries were fitted on the rotation table of the μ CT and imaged using a Skyscan 1172 desktop μ CT system with a 100kV X-ray source (10W, 20-100kV, 0-250 μ A, <5 μ m spot size) and a 11 Mp X-ray detector (4000 x 2664 pixels). A power setting of 60kV and 167 μ A was used. Images were acquired using a step size of 0.3° over 360° with a camera binning of 4 x 4 and frame averaging of 2. The pixel size was set to 3.75 μ m. The total scanning time, yielding 1200 projection images, was just under 1 h. A stack of 631 horizontal cross sections of 292 x 292 pixels was obtained after tomographic reconstruction of a small region of interest of the projection images. A beam hardening correction of 50% and ring artefact correction of 100 and smoothing of 2 were selected. Avizo V2022.1 was used to generate ortho-slices and with the ruler function it was possible to determine the internal diameter.

4.2.4. Flow-MRI platform design

The capillary flow-MRI platform is schematically shown in Fig. 4.1. The components of the platform were purchased from commercial suppliers, namely: the pressure controller (Elveflow) for controlling the applied pressure, P_{app} in the range 0 – 8 bar with the operational error of ± 1 mbar; the PTFE connecting tubing with $w = 0.9$ mm (BGB Analytik); the PEEK connectors with $w = 0.5$ mm (BGB Analytik); the hydrophilic and hydrophobic glass capillaries with diameters in the range 100 – 540 μ m (BGB Analytik). The hydrophilic/hydrophobic properties of the walls are used in the experiments as a way to probe the flow behavior under different conditions of fluid-wall interactions. Since velocities in cylindrical capillaries scale according to $(w/2)^2$, we have measured the radius of all capillaries with μ CT (see Fig. S4.1 in

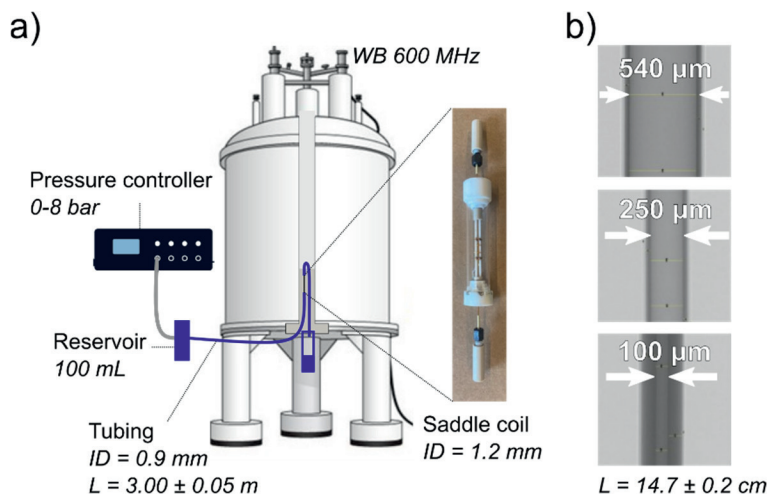


Figure 4.1: a) Scheme of the capillary flow-MRI platform in a WB 600 MHz NMR spectrometer, b) μ CT images of the glass capillaries, used for quantification of the capillary inner diameters.

section 4.5.1). The 1.2 mm saddle coil was supplied by Bruker BioSpin and adapted to the probe in-house. For all experiments, the length of the capillary was fixed to $L = 14.7 \pm 0.2$ cm, the fluid of interest was placed in the reservoir, and the target pressure was applied. The sample flows in the tubing and through the connected glass capillary, positioned inside the saddle coil. If the sample exhibits spatial heterogeneities, *e.g.* due to sedimentation or ageing, it is possible to place the reservoir on a stirrer plate and apply continuous stirring with a magnetic bar during the course of the measurement. Such approach was followed here for the 15 wt% FCD. The flow measurements were carried out at a constant temperature of 20 °C, set by the temperature of the cooling water of the triple axis MRI gradients.

4.2.5. Flow-MRI measurements

The ^1H MRI velocimetry measurements were performed on a wide-bore Avance NEO Bruker spectrometer operating at 14 T. Excitation and detection of the ^1H signal was performed with a saddle radiofrequency coil with an inner diameter of 1.2 mm, using the Micro 5 microimaging gradient system (Bruker BioSpin) with maximum gradient intensity of 3 T m^{-1} along all three directions.

2D ^1H MRI velocity maps were measured using a Pulsed Field Gradient Spin Echo (PFG-SE) sequence,²² within a 2 mm thick slice in the flow direction, echo time $T_E = 10$ ms and repetition time $T_R = 2$ s. The duration of the velocity-encoding gradient

pulses, and their inter-pulse spacing, were $\delta = 1$ ms and $\Delta = 5$ ms, respectively. While for silicone oil and Carbopol we observed only one ^1H NMR signal from methylene and water protons, respectively, SF oil in FCDs yields ^1H NMR signals at distinct chemical shifts at the field strength used in this work. Thus, to avoid chemical shift artefacts, a 90° chemically-selective, low-power, saturation pulse was used in all velocimetry measurements of 15 wt% FCDs with a bandwidth of 1 kHz and frequency offset of 2.46 kHz.² The field-of-view (FOV) in the read and phase directions was (i) 0.9×0.9 mm² for the 540 μm capillary and (ii) 0.6×0.6 mm² for both 250 and 100 μm capillaries. By correspondingly acquiring 64 x 64 pixels, isotropic spatial resolutions of 14 μm and 9 μm could be obtained for measurements (i) and (ii). Using a number of scans $NS = 2$, the total experiment time per velocity map was 4 min, and three consecutive velocity maps were acquired per sample and P_{app} value. Two replicates were acquired for each set of measurements, using a fresh sample batch for each repetition. For the data analysis, the 2D velocity maps were radially averaged to yield 1D velocity profiles. The averaging was performed in MATLAB, with the pixel values binned based on the distance to the center of the capillary. The number of bins was set to 64. As the original dataset contained 64 x 64 pixels, while the derived 1D velocity profile contains 64 averaged points over half of the FOV, the spatial resolution of the 1D profiles was twice that of the original 2D velocity maps.

4.2.6. Theoretical flow profiles

The theoretical velocities for the Newtonian fluid were calculated from the Hagen-Poiseuille (HP) equation:

$$v(x) = \frac{(w/2)^2}{4\eta} \frac{\Delta P}{L} \left[1 - \left(\frac{x}{w/2} \right)^2 \right], \quad (4.2)$$

where ΔP is the measured pressure drop between the inlet and outlet of the capillary, and x is the position across the gap. For the particulate yield stress fluids, the HB¹ model was used:

$$v(x) = \begin{cases} \int \left(\frac{\Delta P x / 2L - \sigma_y}{K} \right)^{1/n} dx & \sigma > \sigma_y \\ C & \sigma < \sigma_y, \end{cases} \quad (4.3)$$

where σ_y denotes the yield stress, K is a proportionality constant with the units of $Pa \cdot s^{1/n}$, and n is a dimensionless power law index, all obtained from global rheological measurements. For stresses below the yield stress, $\sigma < \sigma_y$, the velocity is uniform in the center of the capillary and denoted by C . We note that, for all investigated capillary diameters, the relative stress variation across the radial direction is 100%, with maximum stress at the walls and null value in the center of the capillary. ΔP across the capillary length was measured in a separate experiment using a setup located outside the spectrometer, identical to that used for flow-MRI measurements. The pressure sensors were connected directly to the 540 μm capillary, while an intermediate tubing with $w = 0.9$ mm was used between the sensor and the 250 or 100 μm capillaries. We note that, unlike for the latter capillaries, using a connector tubing with the 540 μm capillary contributed significantly to the measured ΔP values, due to the similar inner diameters of both the tubing and the capillary.

4.2.7. Quantification of flow cooperativity

A number of models have been developed to quantify non-local effects in particulate materials.^{10,11,33,34} In this work, we use the fluidity model developed by Goyon *et al.*¹² for soft, particulate, fluids with rheological properties similar to Carbopol and FCDs. The model is based on the concept of fluidity, defined as the ratio of the shear rate and the shear stress, $f = \dot{\gamma}/\sigma$, and is linked, on a microscopic level, to the local rate of plastic rearrangements across the whole flowing system. In the case of strongly-confined flow, namely, $d/w \geq 1\%$, the local fluidity, $f(x)$, is found to deviate from its predicted global value, f_{bulk} , and to obey the non-local equation¹²:

$$f(x) = f_{bulk} + \xi^2 \frac{\partial^2 f(x)}{\partial x^2}, \quad (4.4)$$

where ξ is the cooperativity length, and f_{bulk} is determined by independent rheological measurements in non-confined flow regime. Detailed description of solving and fitting the model to complex fluids flowing through geometries with non-uniform stress fields, such as the microcapillaries used in this work, can be found in our previous work²⁰. The ξ values for each P_{app} can be obtained either by fitting the mean velocity profiles or by fitting the profiles from individual measurements and averaging the obtained ξ values. For 0.5 wt% Carbopol, both tested approaches yielded equal results, and here we report only the results from the former approach.

For the 15 wt% FCD, due to the higher variability in velocities, the latter approach was used.

4.2.8. Rotational rheology

All rotational rheometric measurements were performed using an Anton Paar (MCR 301) rheometer. Global flow curves were acquired using a geometry with a gap size at least 100 times larger than the determined microstructure size of the sample. For 0.5 wt% Carbopol, a standard stainless steel CP geometry with a diameter of 25 mm was used. In this geometry the cone is truncated, with the resulting minimum gap of $\sim 50 \mu\text{m}$ in the center. Since the measured stress originates primarily from the outer regions of the CP, where the gap size is $\sim 200 \mu\text{m}$, for 0.5 wt% Carbopol the wide-gap approximation is fulfilled. The 15 wt% FCD was measured with a standard stainless steel CC with the radius of the bob $r_i = 5.25 \text{ mm}$, and the radius of the cup $r_o = 8.75 \text{ mm}$. Sandpaper was glued to the surface of the bob to prevent slip. Both samples were pre-sheared for 3 min at 30 s^{-1} and, thereafter, exposed to stress measurements under a shear rate sweep from 100 s^{-1} to 0.01 s^{-1} . A total of 20 points per decade in shear rate were recorded, averaging each stress value over 5 s.

4.3. Results and discussion

4.3.1. Precision of capillary flow measurements

We validated the precision of the MRI velocimetry measurements in capillaries with $w = 100, 250$ and $540 \mu\text{m}$, using silicone oil with viscosity $\eta_{20^\circ} = 1.1 \text{ Pa}\cdot\text{s}$. For the $250 \mu\text{m}$ capillary we also tested the effect of wall slip in untreated hydrophilic walls and treated hydrophobic walls. The resulting velocity profiles measured at $P_{app} = 1\text{-}6 \text{ bars}$ are shown in Fig. 4.2. All measured flow profiles for silicone oil are well described by the HP equation within 5% maximum relative deviation. Wall slip is absent in all measurements, as visible by the comparison of data in Figs. 4.2c and 4.2d. We also calculated the local flow curves, reporting the local shear rate, $\dot{\gamma}(x)$, obtained from the slopes, $\partial V_x / \partial x$, of all measured velocity profiles, vs. the local stress calculated as $\sigma(x) = \Delta P x / 2L$. All the resulting flow curves collapse onto one master curve, and are in agreement with separate rheological measurements of viscosity (see Fig. S4.2 in section 4.5.2). These results evidence that flow in our setup is temporally stable and reproducible.

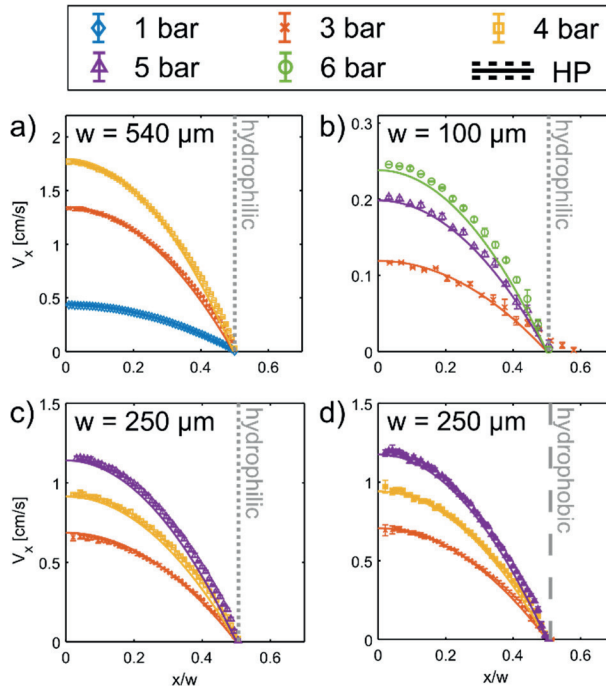


Figure 4.2: ^1H MRI velocity profiles of silicone oil ($\eta_{20\text{ }^\circ\text{C}} = 1.1 \text{ Pa}\cdot\text{s}$) acquired at various applied pressures in capillaries with either hydrophilic walls (gray dotted line) and w equal to a) $540 \mu\text{m}$, b) $100 \mu\text{m}$, c) $250 \mu\text{m}$, or d) hydrophobic walls (gray dashed line) and $w=250 \mu\text{m}$. The error bars represent variation in velocities over 3 time points and 2 replicates. Experimental profiles are compared with theoretical velocities (solid lines) calculated from the HP model (Eq. 4.2), plotted against a normalized spatial coordinate x/w .

4.3.2. Proof of concept: confined flow of 0.5 wt% Carbopol

In this section, we study the flow of 0.5 wt% Carbopol in capillaries with diameters of 540 and $100 \mu\text{m}$. In 0.5 wt% Carbopol, the polymer blob size was determined to be $(2.30 \pm 0.02) \mu\text{m}$ (see Figs. S4.3a-b and Table S4.1 in section 4.5.3). Hence, only for the smallest capillary the flow of 0.5 wt% Carbopol is expected to fall within the strongly-confined regime. The resulting ^1H MRI velocity profiles from all above capillaries, with either hydrophilic or hydrophobic walls, are presented in Figs. 4.3a – c. In all measured velocity profiles, a region of non-sheared fluid is detected in the center of the capillary. The coexistence of sheared and non-sheared regions is typical for yield stress fluids and occurs when the applied stress is below the yield stress of the material. In the top row of Fig. 4.3 the experimental velocity profiles are compared with velocities calculated from the global flow behavior measured by

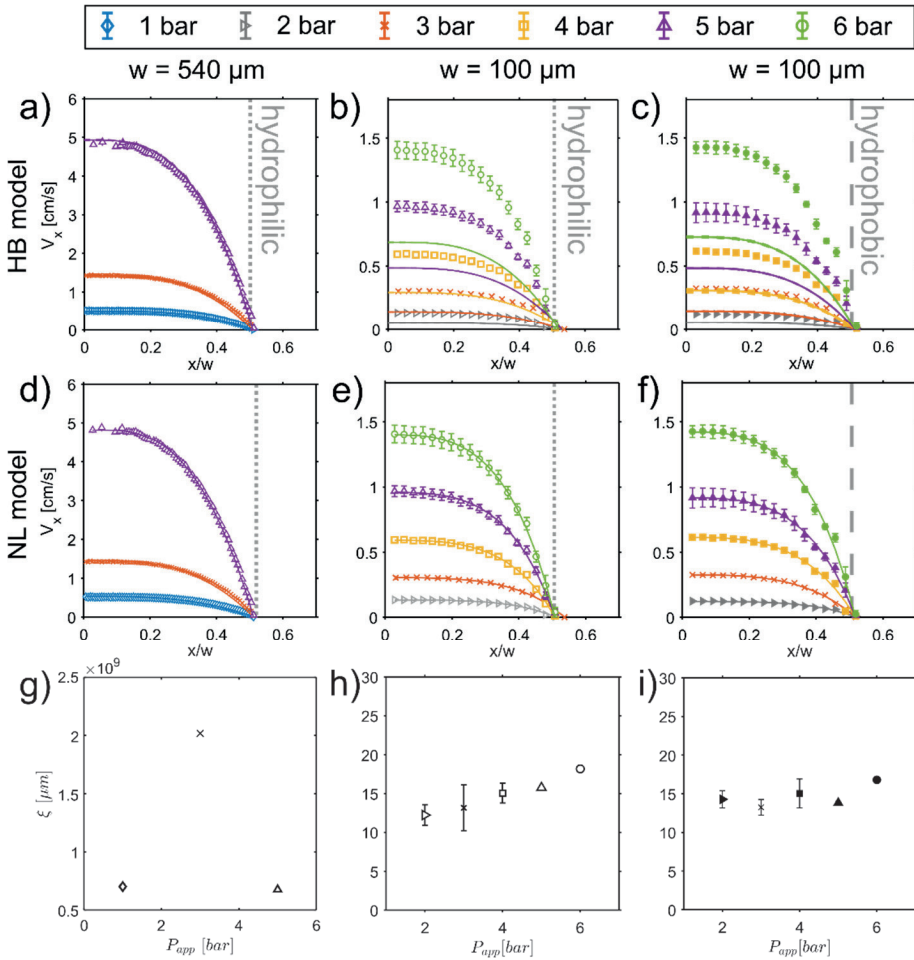


Figure 4.3: ^1H MRI velocity profiles of 0.5 wt% Carbopol acquired at various P_{app} values in capillaries with hydrophilic ($w=540\ \mu\text{m}$ and $100\ \mu\text{m}$, left and middle columns) or hydrophobic ($w=100\ \mu\text{m}$, right column) walls. The vertical gray dotted or dashed lines represent, respectively, hydrophilic or hydrophobic walls of the capillaries. The error bars refer to three consecutive measurements of two sample replicates. Experimental velocity profiles are compared with theoretical velocities calculated from the global HB model (solid line, top row) or fitted with the fluidity model (solid line, middle row). The fitted ξ values (h and i) are reported with the fitting error. The fitting of velocity profiles in the $w=540\ \mu\text{m}$ capillary failed to converge at a solution, resulting in unreliable ξ estimates (g).

conventional rotational CP rheology (Fig. S4.4a in section 4.5.3). As expected, only the velocities in the largest capillary, where flow of 0.5 wt% Carbopol is outside the strong confinement regime, can be correctly predicted by the global HB model. In

the smallest capillary, the measured velocities significantly exceed those predicted by the HB model. In the latter condition, no appreciable wall slip effect is observed. By plotting the local flow curves derived from the velocity profiles and the respective ΔP measurements (see Fig. S4.5 in section 4.5.3), it is evident that flow of 0.5 wt% Carbopol at $w = 100 \mu\text{m}$ cannot be described by a global law, and that the flow behavior at each P_{app} is unique and exhibits non-local character, as a result of cooperativity. As shown in Figs. 4.3d–i, by fitting the mean experimental velocity profiles for 0.5 wt% Carbopol acquired for $w = 100 \mu\text{m}$ with the fluidity model (Eq. 4.4), the cooperativity length, denoted as ξ ,¹² could be determined. All experimental velocity profiles appear well described by the fluidity model, although, as expected, for the largest capillary, the fitting sub-routine failed to converge at a reliable solution, which resulted in the exceedingly high ξ values with no physical meaning (Fig. 4.3g). For the $w = 100 \mu\text{m}$ capillaries, with either smooth or hydrophobic walls, the resulting mean ξ value is $15 \pm 2 \mu\text{m}$ and, as expected, in the order of a few particles. We note that this result is in good agreement with the cooperativity length determined in an identical sample of Carbopol by Géraud *et al.*¹⁴, with only 10% difference possibly originating from differences in the shape and size of the flow geometry.

Notably, all the ξ values obtained for 0.5 wt% Carbopol are in the order of our MRI spatial resolution, and could be reliably quantified thanks to the high mechanical stability of our platform, and to the high SNR and filling factor conditions. Finally, contrarily to what was found previously for emulsions by Paredes *et al.*,¹⁵ we observe here that altering the chemical properties of the walls has no significant effect on the inter-particle interactions in the flow of Carbopol. In contrast, the authors of the aforementioned study¹⁵ found that oil droplets in an emulsion adhere to hydrophobic walls of rectangular microchannels, affecting the flow at boundaries. In the case of Carbopol, such adhesion likely does not occur because the continuous and dispersed phases therein have similar hydrophobic interactions.

4.3.3. Proof of concept: confined flow of 15 wt% FCD

In our previous work,²⁰ based on rheo-MRI measurements in a custom-made $500 \mu\text{m}$ CC, we have shown that flow cooperativity in concentrated FCDs, with 27 wt% solid fat content (SFC), depends on the cooling rate used for sample preparation, as this, in turn, influences the fat crystal platelet aggregate size and the inter-aggregate weak-link network.²⁰ With the here proposed capillary flow-MRI platform we could investigate cooperativity at even higher confinement degrees. To this aim, we have

measured the flow behavior of a 15 wt% FCD sample, with SFC $\sim 15\%$, in 540 and 250 μm capillaries, and obtained the mean velocity profiles shown in Figs. 4.4a and 4.4b. We note that the oil in FCDs yields ^1H NMR signals at distinct chemical shifts at the field strength used in this work. With our chosen measurement approach² chemical shift artefacts were however adequately suppressed. We found that flow is stable in time and reproducible over the two replicates in the 250 μm capillary. In the largest capillary, velocities are temporally stable at all pressures, while reproducible across replicates only for the lowest P_{app} values, namely 0.25 and 0.5 bar. At the two highest pressures the reproducibility error increases up to about 14%. However, velocity enhancement of about 40% (data not shown) with respect to theoretical velocities

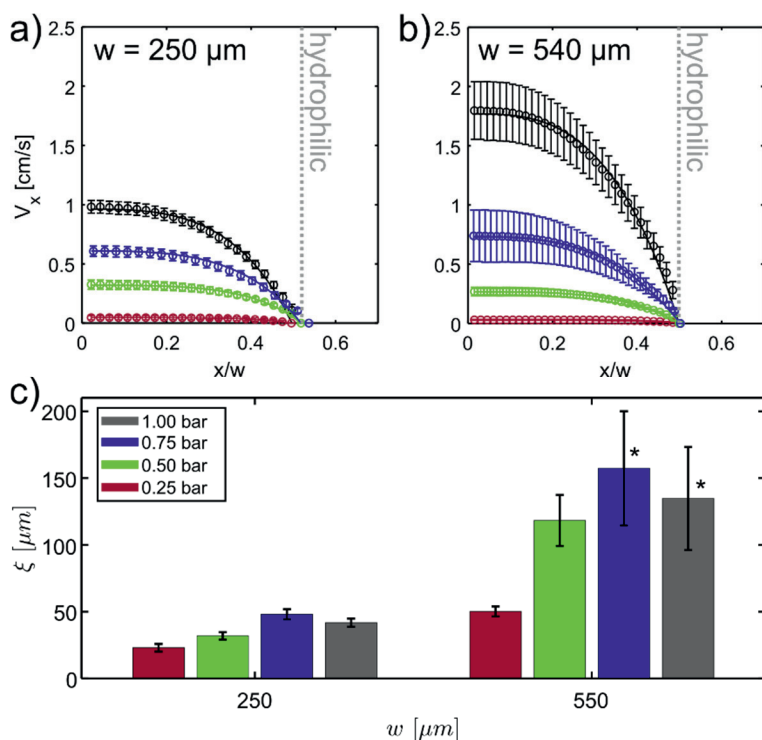


Figure 4.4: ^1H MRI velocity profiles of 15 wt% FCD acquired at various P_{app} in capillaries with w equal to a) 250 μm , and b) 540 μm , plotted as a function of the normalized position, x/w . The error bars represent variation in velocities over 6 profiles (3 time points, 2 replicates). Velocity profiles are fitted with the fluidity model (solid lines). The obtained ξ values are shown in c) for both capillaries with the error bar representing the standard deviation of individual values. All ξ values were calculated from 6 experiments with the exception of values with * symbol, where only 3 experiments were used for calculation.

calculated from the global flow behavior (see Fig. S4.4b in section 4.5.3) is observed for both capillaries and at all P_{app} values. As established from the autocorrelation function of the micrographs of the sample (see Figs. S4.3c and 4.3d in section 4.5.3), the mean size of the crystal aggregates in the 15 wt% FCD is $(21.06 \pm 0.02) \mu\text{m}$. It therefore follows that even in the largest capillary the flow falls within the strongly-confined flow regime, with $d/w \approx 4\%$. We note that during our velocimetry measurements we did not detect any particle migration perpendicularly to the flow direction, as evidenced from the constant ^1H NMR intensities in the 2D density profiles (see Fig. S4.7 in section 4.5.3). With an attempt to model the flow of the 15 wt% FCD in both capillaries, and quantify the extent of cooperativity, we fitted the experimental velocity profiles with the fluidity model (Eq. 4.4), with the results presented in Fig. 4.4. Because of the aforementioned variability across the individual profiles, we fitted each profile separately and in Fig. 4.4c we report the averaged ξ values. We observe that (i) at each pressure ξ increases by a factor of 2–3 between $w = 250 \mu\text{m}$ and $w = 540 \mu\text{m}$, and that (ii) ξ reaches highest values at 0.75 bar for both capillaries. We note the fluidity model describes well all measured flow profiles at $w = 250 \mu\text{m}$, but only those at the two lowest pressures for the $w = 540 \mu\text{m}$. For $P_{app} = 0.75$ and 1 bar ξ values could be reliably quantified only for one of the replicates (see caption of Fig. 4.4). The latter evidence confirms the lower reproducibility of flow measurements at those pressures. Hence, we conclude that at high applied stresses and relatively low confinement degree of $d/w \approx 4\%$, the system exits the cooperative flow regime and, thus, quantification of ξ values is less robust. This is further confirmed by the collapse of the local flow curves onto a master curve at high pressures for the largest capillary (see Fig. S4.6a in section 4.5.3).¹¹

4.3.4. Cooperativity lengths and microstructure

In Fig. 4.5 we compare the ξ values determined for the 0.5% Carbopol in the $100 \mu\text{m}$ capillary and for the 15 wt% FCD in the 250 and $540 \mu\text{m}$ capillaries. For the latter sample we also include the ξ values previously obtained with a rotational rheo-MRI setup using a CC geometry with $500 \mu\text{m}$ gap size.²⁴ Details of rotational rheo-MRI measurements and data analysis are reported in our previous study.²⁰ In this rotational setup the flow is shear-controlled, while in the capillary flow-MRI setup it is pressure-controlled. For data comparison, we plotted the ξ values against the walls stress, σ_{wall} , calculated from either the measured ΔP , for capillaries, or from the measured torque, for the CC. As can be seen from Fig. 4.5a, ξ values spanning two

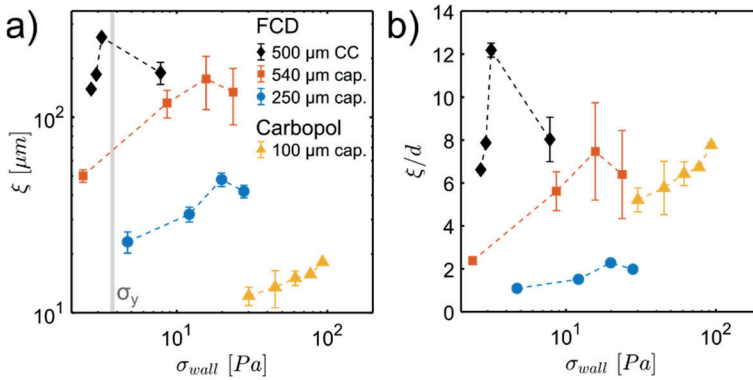


Figure 4.5: Cooperativity lengths ξ found in flow of 15 wt% FCD and 0.5 wt% Carbopol in all studied geometries, shown as a) non-normalized values or b) values normalized by the mean sizes of the particles, plotted against stress at the wall, calculated from the stress distribution in each geometry. The vertical grey panel in (a) marks the yield stresses of 0.5 wt% Carbopol and 15 wt% FCD, respectively equal to 4.07 and 3.46 Pa. The data points are connected with dashed lines as a guide for the eye.

orders of magnitude could be quantified. For 0.5 wt% Carbopol ξ varies by only 30% in the pressure range 2 – 6 bar, while for the 15 wt% FCD it respectively varies by 50% and 70% at $w = 250$ and $540 \mu\text{m}$ in the pressure range 0.25 – 1 bar. This different behavior of 0.5 wt% Carbopol and 15 wt% FCD agrees with the predictions of the kinetic elasto-plastic (KEP) model,¹⁰ according to which ξ diverges at the yield stress of the material. As shown in Fig. 4.5a, for 0.5 wt% Carbopol we have probed cooperativity at $\sigma \gg \sigma_y$, while for the 15 wt% FCD, the measurements were conducted at $\sigma \sim \sigma_y$. By using either the 500 μm gap CC at $\dot{\gamma}_{\text{app}} = 0.5 - 10 \text{ s}^{-1}$ or the 540 μm capillary at $P_{\text{app}} = 0.25 - 1 \text{ bar}$, consistent ξ values and trends were observed for the 15 wt% FCD sample. We note that ξ values in the 540 μm capillary, where stress inhomogeneity is 100%, are $\sim 35\%$ smaller than in the CC geometry, where stress inhomogeneity drops to $\sim 11\%$. Since the geometry-dependent stress distribution is accounted for in the adopted model, we conclude that the observed difference in ξ arises from a stress-dependent flow cooperativity, as predicted by the KEP model,¹⁰ and as also seen in studies of cellulose dispersions or soft colloidal microgels³⁵. Finally, in Fig. 4.5b we plot the normalized ξ/d values for the 15 wt% FCD and 0.5 wt% Carbopol, to represent the average number of particles participating in non-local interactions. We found that the non-local interactions span, on average, $\sim 5 - 8$ particles for both 0.5 wt% Carbopol ($d/w \approx 2\%$), and the 15 wt% FCD, the latter measured in either the 500 μm gap CC or the 540 μm capillary ($d/w \approx 4\%$). However, as the degree of confinement is increased to $\sim 8\%$, as done here for

the 15 wt% FCD in the 250 μm capillary, the number of particles participating in the non-local interaction decreases to 2. This is in good agreement with our previous work on 27 wt% FCD, where we varied the degree of confinement, d/w , in the range 5 – 40% by tuning the crystal aggregate size, d . In that study we observed that the ξ values decreased from spanning ~ 10 particles at $d/w = 5\%$ to null at the extreme confinement condition $d/w = 40\%$.

4.4. Conclusions

We have developed a capillary flow-MRI platform to study flow of complex structured fluids in confined geometries with easily tunable gap size and wall properties. Unlike existing rheo-MRI setups, the platform is easily adaptable to both higher- and lower-field MRI magnets, irrespectively of the bore size. The here exploited range of flow confinement sizes, within 100 – 540 μm , can be expanded down to ~ 50 μm and up to cm-scale. By ensuring mechanical stability of the capillaries under flow, velocities ~ 0.01 – 10 cm/s can be measured with in-plane spatial resolution up to 4.5×4.5 μm^2 . The use of cylindrical capillaries enables achieving high filling factor within the r.f. saddle coil and acquiring the signal within a slice up to 5 mm thick. As a results, high SNR can be obtained. Notably, the developed flow-MRI platform enables using microfluidics-scale gap sizes, typically used in optical velocimetry, without any requirement of fluids' optical-transparency. Furthermore, MRI velocimetry can uniquely be combined with, *e.g.*, spectroscopy or T_1 and T_2 relaxation measurements to probe molecular alignment, particle migration or phase separation under flow.

The performance of the developed flow-MRI setup was here demonstrated for the study of confinement-induced flow cooperativity for two industrially relevant fluids: 0.5 wt% Carbopol and 15 wt% FCD. Reproducible 2D velocity maps were obtained with resolution up to 9×9 μm^2 in capillaries with diameters 100 – 540 μm . 0.5 wt% Carbopol, with mean particle size ~ 2 μm , was found to exhibit pressure-independent cooperativity lengths, ξ , of ~ 15 μm in a 100 μm capillary. With this sample we tackled the quantification of ξ values as low as the MRI resolution. On the other hand, 15 wt% FCD was found to exhibit ξ values in the range 30 – 150 μm , depending on applied pressure and confinement size. Comparison with ξ values obtained previously for the 15 wt% FCD in a CC geometry,²⁴ with comparable confinement degree but more homogeneous stress distribution, revealed that ξ increases with increasing stress homogeneity within the geometry. Finally, we found that for the 15 wt% FCD, the number of particles participating in the non-local interaction decreases

from ~ 8 to ~ 2 particles with increasing confinement degree from 4% to 8%, in agreement with our previous rheo-MRI findings.²⁰

We foresee that the developed capillary flow-MRI platform will aid achieving, for a wide range of fluid properties, a comprehensive understanding of particle interactions under flow and their dependence on fluid's microstructure as well as on size, shape and wall properties of the confining geometry. The developed knowledge will enable correctly predicting flow profiles, even in industrially-relevant conditions, in complex fluids undergoing shear-induced microstructural changes, such as aggregation in protein solutions,³⁶ network destruction and rejuvenation in gels²⁹ or alignment, crucial in the production of fibers.³⁷⁻⁴⁰ The flow-MRI platform can be easily adapted to ultra-high field MRI magnets, boosting the sensitivity of the technique and enabling chemically-resolved, velocimetric experiments. Such measurements can be exploited in microfluidic studies of mixing of multiphase fluids or concentration changes during microfiltration. Ongoing and future work will involve monitoring the aforementioned microstructural alterations *in situ* at temperatures beyond the range currently achievable in narrow-gap rheo-MRI CC geometries,²⁰ limited to 45 °C by the presence of glued joints. In the future, other r.f. coil designs, such as striplines,⁴¹ will be explored for further advancement in sensitivity and resolution, possibly in combination with narrow-bore high- and ultra-high field MRI magnets.

Author Contributions

Conceptualization: C. T., J. A. D., J. P. M. v. D., and T. O.; experimental measurements and data analysis: K. W. M.; validation: K. W. M.; formal analysis: K. W. M.; writing — original draft preparation: K. W. M.; writing — review and editing: C. T., J. A. D. and J. P. M. v. D.; visualization: K. W. M.; supervision: C. T., J. P. M. v. D, J. A. D. All authors have read and agreed to the published version of the manuscript.

Acknowledgment

This project was supported by the uNMR-NL Grid: A distributed, state-of-the-art Magnetic Resonance facility for the Netherlands (NWO grant 184.035.002). Upfield (Wageningen, The Netherlands) is thanked for providing the solid fat blend. We acknowledge John Philippi for technical support. We thank Ruud den Adel and Lonneke Zuidgeest for help with acquisition and processing of the μ CT images.

References

- (1) Herschel, W. H.; Bulkeley, R. Konsistenzmessungen von Gummi-Benzollösungen, *Kolloid-Zeitschrift* **1926**, 39 (4), 291-300.
- (2) Nikolaeva, T.; Vergeldt, F. J.; Serial, R.; Dijkman, J. A.; Venema, P.; Voda, A.; van Duynhoven, J. P. M.; Van As, H. High Field MicroMRI Velocimetric Measurement of Quantitative Local Flow Curves, *Anal. Chem.* **2020**, 92 (6), 4193-4200.
- (3) Dinkgreve, M.; Fazilati, M.; Denn, M. M.; Bonn, D. Carbopol: From a simple to a thixotropic yield stress fluid, *J. Rheol.* **2018**, 62 (3), 773-780.
- (4) Raynaud, J. S.; Moucheront, P.; Baudez, J. C.; Bertrand, F.; Guilbaud, J. P.; Coussot, P. Direct determination by nuclear magnetic resonance of the thixotropic and yielding behavior of suspensions, *J. Rheol.* **2002**, 46 (3), 709-732.
- (5) de Kort, D. W.; Nikolaeva, T.; Dijkman, J. A. In *Modern Magnetic Resonance*, Webb, G. A.; Springer International Publishing, 2018, pp 1589-1608.
- (6) Meeker, S. P.; Bonnetcaze, R. T.; Cloitre, M. Slip and flow in pastes of soft particles: Direct observation and rheology, *J. Rheol.* **2004**, 48 (6), 1295-1320.
- (7) Larson, R. G.; Wei, Y. A review of thixotropy and its rheological modeling, *J. Rheol.* **2019**, 63 (3), 477-501.
- (8) Sun, J.; Zhou, W.; Huang, D. In *Reference Module in Food Science*, Smithers, G. W.; Elsevier, 2018, pp 1-9.
- (9) Liu, F.; Wang, X. Synthetic Polymers for Organ 3D Printing, *Polymers* **2020**, 12 (8).
- (10) Bocquet, L.; Colin, A.; Ajdari, A. Kinetic Theory of Plastic Flow in Soft Glassy Materials, *Phys. Rev. Lett.* **2009**, 103 (3), 036001.
- (11) Goyon, J.; Colin, A.; Bocquet, L. How does a soft glassy material flow: finite size effects, non local rheology, and flow cooperativity, *Soft Matter* **2010**, 6 (12), 2668-2678.
- (12) Goyon, J.; Colin, A.; Ovarlez, G.; Ajdari, A.; Bocquet, L. Spatial cooperativity in soft glassy flows, *Nature* **2008**, 454, 84-87.
- (13) Derzsi, L.; Filippi, D.; Mistura, G.; Pierno, M.; Lulli, M.; Sbragaglia, M.; Bernaschi, M.; Garstecki, P. Fluidization and wall slip of soft glassy materials by controlled surface roughness, *Phys. Rev. E* **2017**, 95 (5), 052602.
- (14) Géraud, B.; Jørgensen, L.; Ybert, C.; Delanoë-Ayari, H.; Barentin, C. Structural and cooperative length scales in polymer gels, *Eur. Phys. J. E* **2017**, 40 (5), 1-10.
- (15) Paredes, J.; Shahidzadeh, N.; Bonn, D. Wall slip and fluidity in emulsion flow, *Phys. Rev. E* **2015**, 92 (4), 042313.
- (16) de Kort, D. W.; Veen, S. J.; Van As, H.; Bonn, D.; Velikov, K. P.; van Duynhoven, J. P. M. Yielding and flow of cellulose microfibril dispersions in the presence of a charged polymer, *Soft Matter* **2016**, 12 (21), 4739-4744.
- (17) Serial, M. R.; Bonn, D.; Huppertz, T.; Dijkman, J. A.; van der Gucht, J.; van Duynhoven, J. P. M.; Terenzi, C. Nonlocal effects in the shear banding of a thixotropic yield stress fluid, *Phys. Rev. Fluids* **2021**, 6 (11), 113301.
- (18) Serial, M. R.; Velichko, E.; Nikolaeva, T.; den Adel, R.; Terenzi, C.; Bouwman, W. G.; van Duynhoven, J. P. M. High-pressure homogenized citrus fiber cellulose dispersions: Structural characterization and flow behavior, *Food Struct.* **2021**, 30, 100237.
- (19) de Cagny, H.; Fall, A.; Denn, M. M.; Bonn, D. Local rheology of suspensions and dry granular materials, *J. Rheol.* **2015**, 59 (4), 957-969.
- (20) Milc, K. W.; Dijkman, J. A.; van Duynhoven, J. P. M.; Terenzi, C. Quantifying cooperative flow of fat crystal dispersions, *Soft Matter* **2022**, 18 (14), 2782-2789.
- (21) Fazelpour, F.; Tang, Z.; Daniels, K. E. The effect of grain shape and material on the nonlocal rheology of dense granular flows, *Soft Matter* **2022**, 18 (7), 1435-1442.
- (22) Callaghan, P. T. Rheo-NMR: nuclear magnetic resonance and the rheology of complex fluids, *Rep. Prog. Phys.* **1999**, 62 (4), 599-670.

- (23) Callaghan, P. T. Rheo-NMR and velocity imaging, *Curr. Opin. Colloid Interface Sci.* **2006**, *11* (1), 13-18.
- (24) Milc, K. W.; Serial, M. R.; Philippi, J.; Dijkstra, J. A.; van Duynhoven, J. P. M.; Terenzi, C. Validation of temperature-controlled rheo-MRI measurements in a submillimeter-gap Couette geometry, *Magn. Reson. Chem.* **2022**, *60* (7), 606-614.
- (25) Fink, J. K. In *High Perform. Polym.*, Fink, J. K.; William Andrew Publishing, 2014, pp 301-320.
- (26) Xu, L.; Gu, L.; Su, Y.; Chang, C.; Wang, J.; Dong, S.; Liu, Y.; Yang, Y.; Li, J. Impact of thermal treatment on the rheological, microstructural, protein structures and extrusion 3D printing characteristics of egg yolk, *Food Hydrocoll.* **2020**, *100*, 105399.
- (27) Song, H.; Ismagilov, R. F. Millisecond Kinetics on a Microfluidic Chip Using Nanoliters of Reagents, *J. Am. Chem. Soc.* **2003**, *125* (47), 14613-14619.
- (28) Graziano, R.; Preziosi, V.; Uva, D.; Tomaiuolo, G.; Mohebbi, B.; Claussen, J.; Guido, S. The microstructure of Carbopol in water under static and flow conditions and its effect on the yield stress, *J. Colloid Interface Sci.* **2021**, *582*, 1067-1074.
- (29) Nikolaeva, T.; den Adel, R.; Velichko, E.; Bouwman, W. G.; Hermida-Merino, D.; Van As, H.; Voda, A.; van Duynhoven, J. P. M. Networks of micronized fat crystals grown under static conditions, *Food Funct.* **2018**, *9* (4), 2102-2111.
- (30) Acevedo, N. C.; Block, J. M.; Marangoni, A. G. Critical laminar shear-temperature effects on the nano- and mesoscale structure of a model fat and its relationship to oil binding and rheological properties, *Faraday Discuss.* **2012**, *158*, 171-194.
- (31) Maleky, F.; Smith, A. K.; Marangoni, A. Laminar Shear Effects on Crystalline Alignments and Nanostructure of a Triacylglycerol Crystal Network, *Cryst. Growth Des.* **2011**, *11* (6), 2335-2345.
- (32) Gregersen, S. B.; Miller, R. L.; Hammershøj, M.; Andersen, M. D.; Wiking, L. Texture and microstructure of cocoa butter replacers: Influence of composition and cooling rate, *Food Struct.* **2015**, *4*, 2-15.
- (33) Bouzid, M.; Trulsson, M.; Claudin, P.; Clément, E.; Andreotti, B. Nonlocal Rheology of Granular Flows across Yield Conditions, *Phys. Rev. Lett.* **2013**, *111* (23), 238301.
- (34) Mandal, S.; Nicolas, M.; Pouliquen, O. Rheology of Cohesive Granular Media: Shear Banding, Hysteresis, and Nonlocal Effects, *Phys. Rev. X* **2021**, *11* (2), 021017.
- (35) van de Laar, T.; Schroën, K.; Sprakel, J. Cooperativity and segregation in confined flows of soft binary glasses, *Phys. Rev. E* **2015**, *92* (2), 022308.
- (36) Vilotte, A.; Bodiguel, H.; Ako, K.; Gunes, D. Z.; Schmitt, C.; de Loubens, C. Kinetic and structural characterization of whey protein aggregation in a millifluidic continuous process, *Food Hydrocoll.* **2021**, *110*, 106137.
- (37) Tian, B.; Wang, Z.; de Campo, L.; Gilbert, E. P.; Dalglish, R. M.; Velichko, E.; van der Goot, A. J.; Bouwman, W. G. Small angle neutron scattering quantifies the hierarchical structure in fibrous calcium caseinate, *Food Hydrocoll.* **2020**, *106*, 105912.
- (38) Angelico, R.; Gentile, L.; Ranieri, G. A.; Oliviero Rossi, C. Flow-induced structures observed in a viscoelastic reverse wormlike micellar system by magnetic resonance imaging and NMR velocimetry, *RSC Adv.* **2016**, *6* (40), 33339-33347.
- (39) Masselon, C.; Colin, A.; Olmsted, P. D. Influence of boundary conditions and confinement on nonlocal effects in flows of wormlike micellar systems, *Phys. Rev. E* **2010**, *81* (2), 021502.
- (40) Trebbin, M.; Steinhauser, D.; Perlich, J.; Buffet, A.; Roth, S. V.; Zimmermann, W.; Thiele, J.; Förster, S. Anisotropic particles align perpendicular to the flow direction in narrow microchannels, *Proc. Natl. Acad. Sci. U.S.A.* **2013**, *110* (17), 6706-6711.
- (41) Tijssen, K. C. H.; van Weerdenburg, B. J. A.; Zhang, H.; Janssen, J. W. G.; Feiters, M. C.; van Benthum, P. J. M.; Kentgens, A. P. M. Monitoring Heterogeneously Catalyzed Hydrogenation Reactions at Elevated Pressures Using In-Line Flow NMR, *Anal. Chem.* **2019**, *91* (20), 12636-12643.

4.5. Supplementary information

4.5.1. Platform design: radii of capillaries

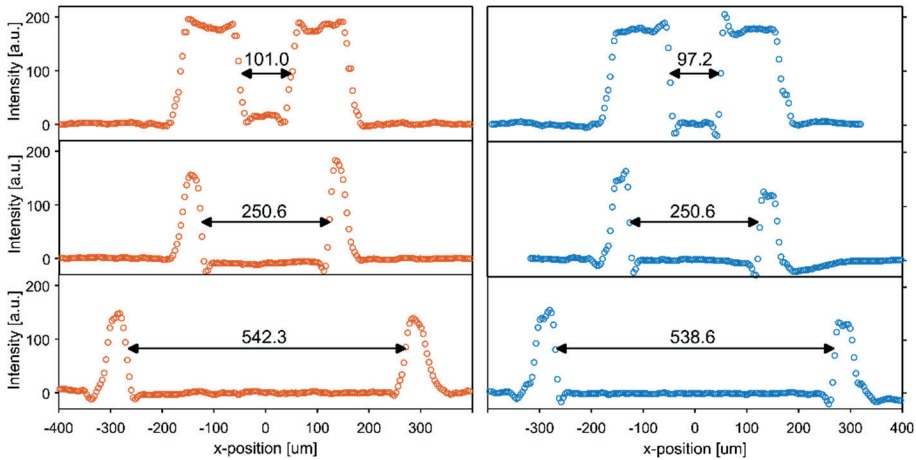


Figure S4.1: Intensity profiles vs the position in the x -direction, extracted from 2D axial μ CT scans of all capillaries with hydrophilic (left column) or hydrophobic walls (right column). The diameters of the capillaries are marked within each profile in units of μm , as measured with Avizo software, using the ruler function. The error associated with the measurement is $3.7 \mu\text{m}$ for all profiles and corresponds to the pixel size.

4.5.2. Validation of the capillary flow-MRI platform with silicone oil

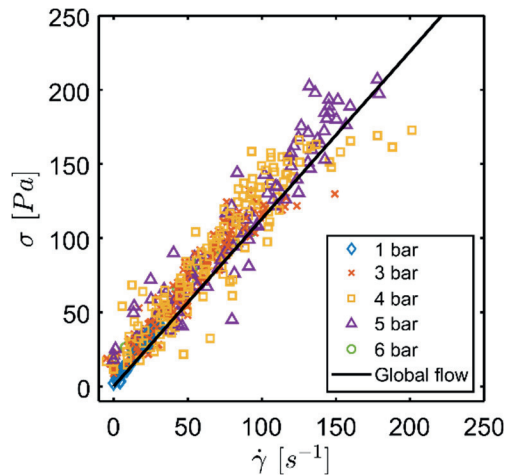


Figure S4.2: Local flow curves of silicone oil calculated from the measured velocity profiles (symbols) in capillaries with diameters ranging from 100 to 540 μm , across all tested P_{app} values. The solid line shows the global flow behavior measured with a rheometer.

4.5.3. Confined flow of 0.5 wt% Carbopol and 15 wt% FCD

To establish the necessary condition where the size of the confinement is within 2 orders of magnitude of the microstructure size, we determined the polymer blob size in 0.5 wt% Carbopol and the crystal aggregate size in the 15 wt% FCD. The micrographs of both samples, together with the associated calculated autocorrelation function, fitted with an exponential decay (Eq. 4.1) are shown in Fig. S4.3. The parameters obtained from fitting, together with the calculated sizes of the microstructure are summarized in Table S4.1.

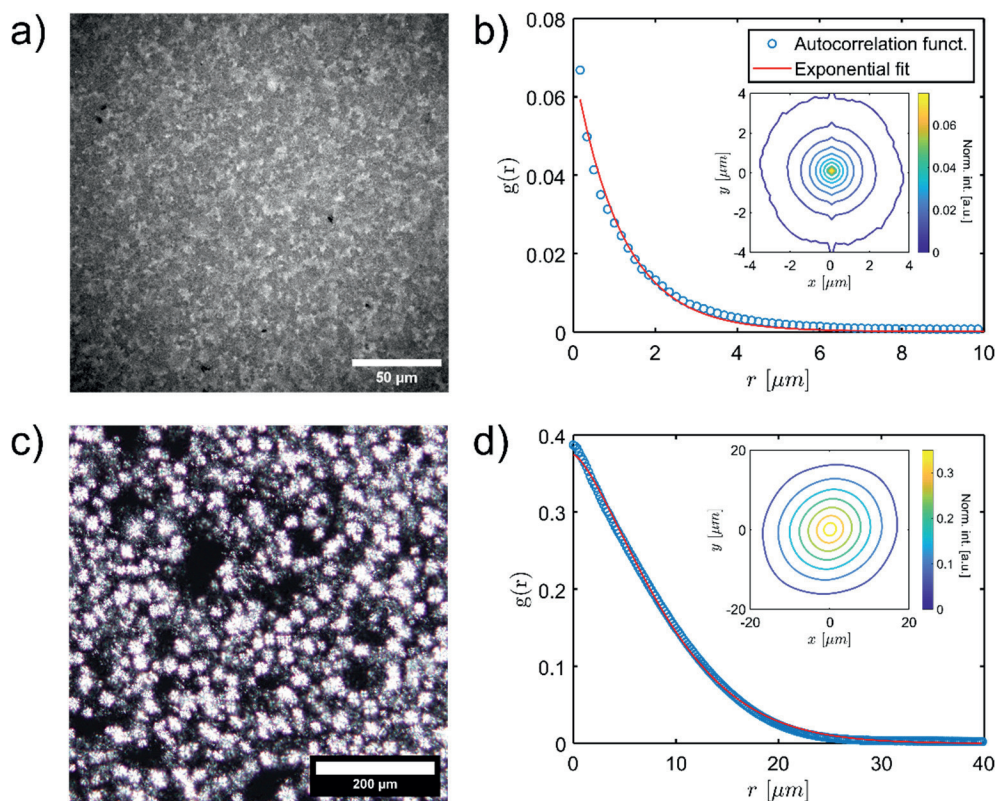


Figure S4.3: Micrographs of a) 0.5 wt% Carbopol and c) 15 wt% FCD, used in the calculation of the respective autocorrelation functions shown in b) and d). The open symbols in the latter plots represent the radial average of the full 2D function shown in the inset and the solid line is the fit of the exponential decay function described with Eq. 4.1.

Table S4.1: Parameters obtained from fitting of the 1D autocorrelation functions of 0.5% Carbopol and 15 wt% FCD with Eq. 4.1 with their respective fitting errors. The parameter α was set manually and was not a fitting parameter.

Sample	g_0	r_0	g_∞	α	$d (2 \cdot r_0)$
0.5 wt % Carbopol	$0.07 \pm 5 \times 10^{-4}$	1.17 ± 0.01	$(1.2 \pm 0.3) \times 10^{-4}$	1.0	2.34 ± 0.02
15 wt% FCD	$0.37 \pm 4 \times 10^{-4}$	10.53 ± 0.01	$(-3.6 \pm 0.4) \times 10^{-4}$	1.5	21.06 ± 0.02

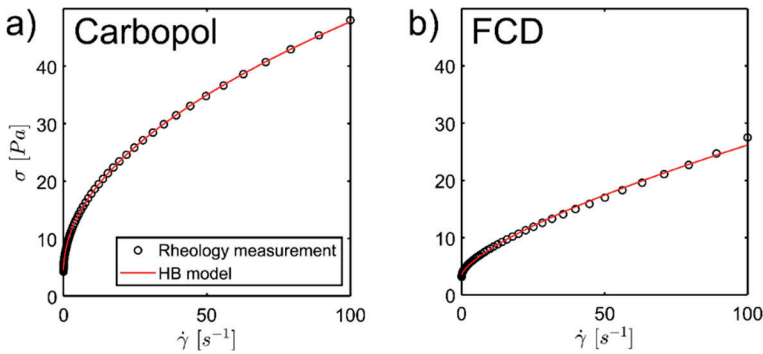


Figure S4.4: Global flow curves (open circles) fitted with the HB model (solid line) of a) 0.5 wt% Carbopol, and b) 15 wt% FCD, described, respectively, by the equations of the form $4.07 + 4.4\dot{\gamma}^{0.5}$ and $3.46 + 0.9\dot{\gamma}^{0.7}$.

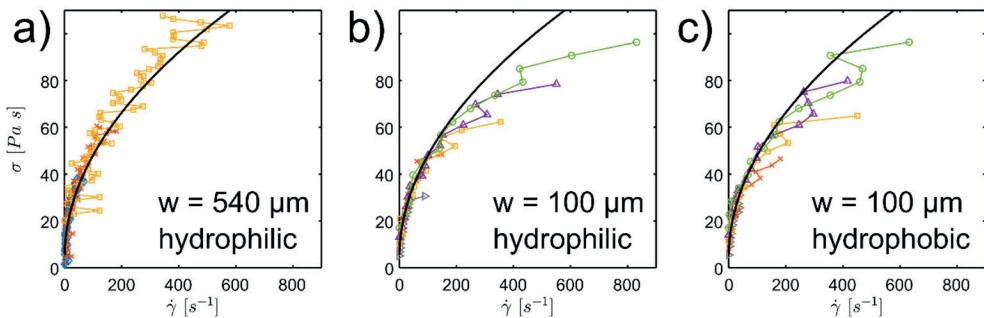
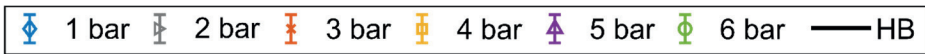


Figure S4.5: Global flow curve (solid line) of 0.5 wt% Carbopol compared with the local flow curves calculated from the 1H MRI velocity profiles measured in a) 540 μm hydrophilic capillary, b) 100 μm hydrophilic capillary, and c) 100 μm hydrophobic capillary.

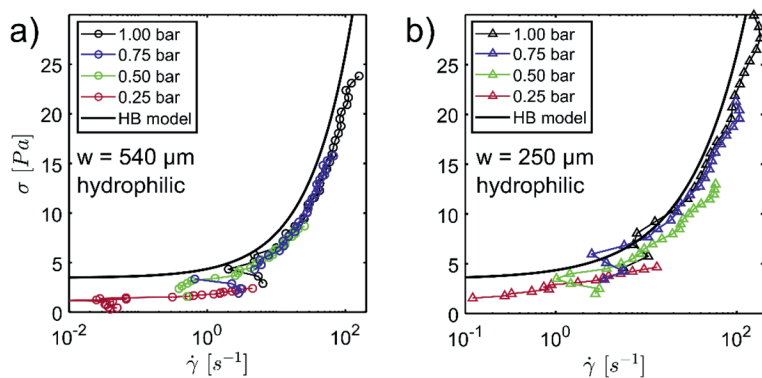


Figure S4.6 Global flow curve (solid line) of 15 wt% FCD compared with the local flow curves calculated from the ^1H MRI velocity profiles measured in a) $540\ \mu\text{m}$ hydrophilic capillary, and b) $250\ \mu\text{m}$ hydrophilic capillary.

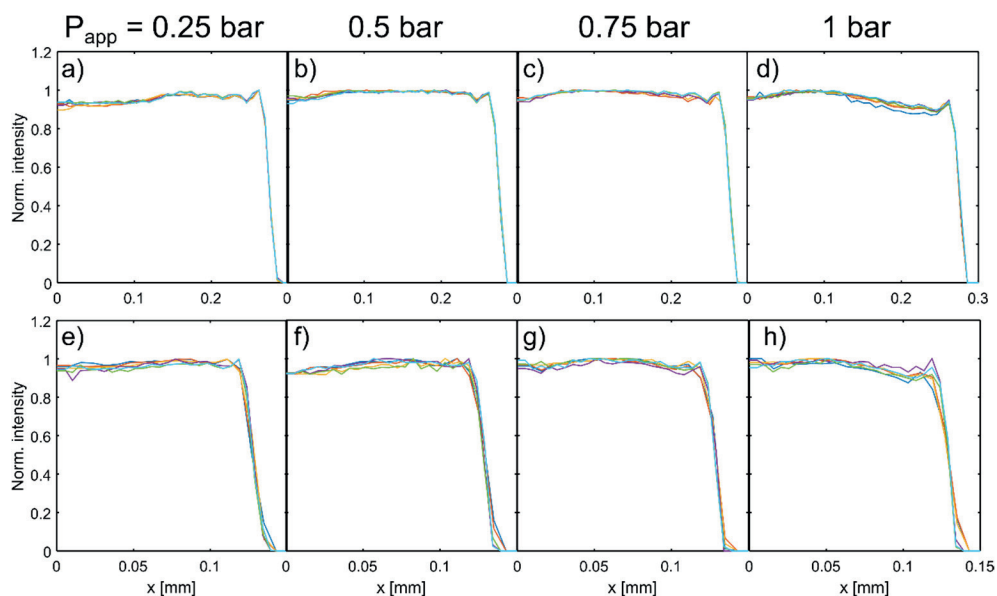


Figure S4.7. Radial averages of the 2D density images obtained from the velocimetry measurements of the 15 wt% FCD in a $540\ \mu\text{m}$ capillary (top row) and $250\ \mu\text{m}$ capillary (bottom row) under the applied pressures of 0.25 bar (a and e), 0.5 bar (b and f), 0.75 bar (c and g) and 1 bar (d and h). Lines of different colors represent the subsequent repeats.

CHAPTER

5

Herschel-Bulkley flow of micronized fat crystal dispersions: effect of shear history

Chapter in preparation as:

Milc, K. W.; Dijksman, J. A.; den Adel, R.; van Duynhoven, J. P. M.; Terenzi, C. *Herschel-Bulkley flow of micronized fat crystal dispersions: effect of shear history.*

Abstract

Micronized fat crystal (MFC) dispersions are a novel ingredient enabling manufacturing of fat-based products in a more reproducible manner. However, reliable predictions of rheological properties of MFC dispersions, particularly during flow in sub-mm confinements, are still challenging, owing to the sensitivity of the microstructure to shear history. With the aim to elucidate the flow-induced microstructural changes, and ultimately aid flow predictions we have studied the local flow behavior of 15% MFC dispersions, as a function of pre-shear duration, using a microcapillary flow-Magnetic Resonance Imaging (MRI) platform. The acquired 2D velocity maps in a 250 μm capillary, revealed that pre-shear times of up to ~ 6 h and the concomitant recrystallization and aggregation of the nanoplatelets result in dispersions flowing up to 5 times faster and exhibiting higher wall slip in comparison to the non-pre-sheared dispersions. The spatial resolution of 10 $\mu\text{m}/\text{pixel}$ of the velocimetric data enabled calculations of local flow curves and quantification of the true rheological properties, inaccessible with global rheology. In contrast to melt-cool fat crystal dispersions (FCDs), no cooperativity effects could be observed for MFC dispersions, which can be attributed to the non-fractality of their networks. We foresee these findings will allow for a more informed design of processing routes of fat-based products as shear history can be employed to manipulate flow behavior and microstructural properties.

5.1. Introduction

Fat crystal dispersions (FCDs) are the starting material in the production of important commercial products such as margarine and chocolate.¹⁻³ The stability and sensorial quality of these fat-based foods is determined by the stability and morphology of the fat crystal network.^{4,5} Yet, the control over this multiscale structure is notoriously challenging, owing to the fact that in the standard melt-cool processing methods, crystallization and network formation occur simultaneously.^{1,6-8} In the view of this challenge, recently a novel and more reproducible approach to manufacturing of FCDs has been introduced, based on micronized fat crystals (MFCs).⁹ In this approach the crystallization and network formation steps are decoupled, by first spraying the fat blend to form crystalline nanoplatelets,¹⁰ which are subsequently dispersed in an oil continuous phase. As the dispersion ages, the nanoplatelets form a hierarchical structure composed of μm -sized aggregates,¹¹ connected via a weak-link network, which is believed to dictate the strength of the material.^{12,13} Although the process offers improved control over the structural morphology, the resulting MFC dispersions are still sensitive to factors such as oil composition and shear/temperature processing conditions.^{14,15} As a consequence, predictions of flow and rheological properties of MFC dispersions remain challenging, limiting the efficiency of production processes and compromising final product quality and stability. Moreover, as the introduction of MFCs in the production of fat-based products happened only in the past few years, up to date, scarce experimental data exists to aid a rational product design process.

The several existing studies on MFCs aimed at describing the underlying microstructural changes in response to shear or variable temperature treatment. Thus far, factors identified as those determining the rheological properties are the multiscale structural rearrangements including nanoplatelet alignment, recrystallization, aggregation, and network formation and degradation.^{14,15} Moreover, networks formed in the MFC dispersions have been described as non-fractal, in contrast to typically fractal networks of the melt-cool FCDs.^{14,16,17}

However, all aforementioned studies investigated the flow of MFC dispersions only in mm-sized confinements, a condition which is not representative of many steps in manufacturing of fat-continuous products, such as emulsification or extrusion, and consumer use, such as spreading of pastes. In such sub-mm confinements, flow of MFC dispersions with aggregate sizes within two orders of magnitude of the flow gap size can be subject to flow instabilities such as cooperativity effects,^{18,19} the presence

of which has already been demonstrated in melt-cool FCDs.⁸ As cooperativity effects result in significant flow enhancement and spatial viscosity variations, their presence must be accounted for in the prediction and modelling of confined flow and processing conditions of the dispersions.

In this study, we thus set out to elucidate the flow-microstructure relationship of 15 wt% MFC dispersions flowing in a microcapillary flow-Magnetic Resonance Imaging (MRI) platform, as a function of pre-shear conditions. Using Raman imaging and small-angle X-ray diffraction (SAXD) we study changes in the multi length scale structure of the 15 wt% MFC dispersions, at the μm and nm scale, respectively, in response to shear treatment. We find that under shear the μm -scale network of the sample weakens because of recrystallization and aggregation of the crystalline nanoplatelets. This results in samples with lower yield stress and more fluid-like properties. Furthermore, the local flow information reveals an evolution of the samples' rheological properties from strongly thixotropic to simple Herschel-Bulkley (HB) flow behavior.

5.2. Materials and methods

The experimental steps described in this section are schematically visualised in Fig. 5.1.

5.2.1. Stock 15 wt% MFC dispersion preparation

MFC powder was prepared by spraying a fat blend dissolved in supercritical CO_2 through a narrow nozzle.⁹ The composition of the fat blend was previously described by Nikolaeva *et al.*¹⁴ The powder was dispersed in a commercially available sunflower (SF) oil to give a 15 wt% dispersion by mixing the two components at 600 rpm for 50 min, at 12 °C (Fig. 5.1a). To inhibit fat recrystallization and the resulting increase in nanoplatelet thickness via Ostwald ripening,^{15,20} weighing of the powder was performed in a 5 °C room while the oil and the glassware were chilled prior to usage. Additionally, to avoid the presence of air bubbles in the stock sample, the dispersion was prepared under vacuum. The obtained material was stored at 5 °C (Fig. 5.1b), and all the experiments were performed within 3 months.

5.2.2. Quantification of average crystal nanoplatelet thickness (ACNT)

A batch of fresh 15 wt% MFC dispersion was subjected to a continuous shear, $\dot{\gamma}_{app} = 5 \text{ s}^{-1}$ for 5 h, during which samples for ACNT quantification were collected every 10 min for the first 1 h and every 30 min for the remaining 4 h (Fig. 5.1c).

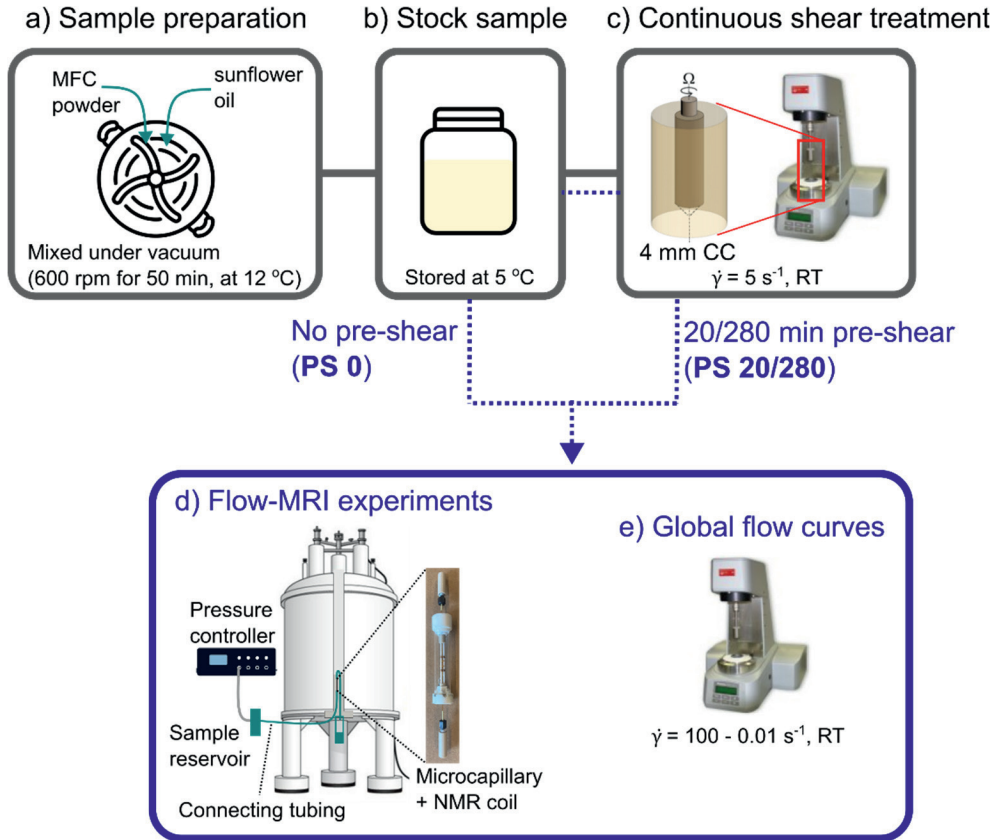


Figure 5.1: Schematic representation of the experimental workflow for the 15 wt% MFC dispersion. The process begins with the preparation of the stock MFC dispersion (a, b). An aliquot of the stock dispersion is then subjected to a continuous shear treatment (c). For the non-pre-sheared (PS0) and pre-sheared (PS20 and PS280) 15 wt% MFC dispersions, local capillary velocity profiles and global flow curves are obtained by MRI (d) and rotational rheology (e), respectively.

The SAXD measurements were performed at 5 °C using the Bruker D8 Discover X-ray powder diffractometer with GADDS (General Area Detector Diffraction System) in a θ/θ configuration and an $1\mu\text{S}$ microfocus X-ray source (CuK α radiation, $\lambda \frac{1}{4} 0.154 \text{ nm}$). SAXD data were collected in the range $1^\circ < 2\theta < 10^\circ$. The beam cross section at the sample position was about 1 mm and the distance between detector and sample was 32.5 cm. Finally, the ACNT values were obtained from the first-order diffraction peak originating from triglyceride 2L layers using the Scherrer equation.²¹

5.2.3. Quantification of mean crystal nanoplatelet aggregate size

A batch of fresh 15 wt% MFC dispersion was subjected to a continuous shear, $\dot{\gamma}_{app} = 5 \text{ s}^{-1}$ for 5 h, during which samples were collected every 10 min for the first 1 h and every 1 h for the remaining 4 h (Fig. 5.1c). The hyperspectral Raman images were measured with a WITec confocal Raman (Alpha 300R+) microscope equipped with a Zeiss upright microscope with a 532 nm laser at 25.0 mW, using a 20×/0.5 objective. The Raman spectrometer was coupled to a cooled (−60 °C) EMCCD detector. The measurements were performed at 4 °C, using a cooled stage. The obtained Raman spectra were in the range of 100 – 3800 cm^{-1} . An integration time of 0.05 s was used for imaging a 100 × 100 μm area with a resolution of 1 μm . The raw data were subjected to standard corrections, namely the cosmic ray removal and background subtraction in the WITec Project FIVE 5.2 software after which the true component analysis was performed using the Raman spectra of the pure components to obtain the spatial distribution of solid fat and liquid oil in all the samples. Subsequently, the mean aggregate size was obtained from the Intensity Correlation Spectroscopy approach, as described in detail by Géraud et al.²² The 2D autocorrelation functions of the Raman images were calculated and radially averaged. The resulting exponential decay was fitted with the following equation:

$$g(r) = g_0 \exp\left(-\left(\frac{r}{r_0}\right)^\alpha\right) + g_\infty, \quad (5.1)$$

where r_0 is the correlation length, an equivalent of particle radius, g_0 is the peak intensity and g_∞ is the background intensity.

5.2.4. Pre-shear treatment

With the aim to study the flow-microstructure relationship, three samples were subjected to various durations of controlled pre-shear, prior to flow-MRI and global flow curve measurements. Sample **PS0** (pre-shear 0 min) was not pre-sheared, while samples **PS20** and **PS280** were pre-sheared for 20 and 280 min, respectively. The pre-shear was done by applying a constant shear rate of $\dot{\gamma}_{app} = 5 \text{ s}^{-1}$ in a Couette cell (CC) made of polyether ether ketone (PEEK), with a gap of 4 mm.

5.2.5. Rheology

The continuous pre-shear treatment (Fig. 5.1c), and acquisition of global flow curves (Fig. 5.1e) were performed using an Anton Paar (MCR 301) rheometer. The former measurement was performed using a custom PEEK CC geometry, with the radius of

the cup, $r_o = 11$ mm and radius and length of the bob respectively, $r_i = 7$ mm and $H = 44$ mm. The sample was exposed to an applied shear rate, $\dot{\gamma}_{app} = 5$ s⁻¹ and the stress exerted on the walls of the bob was measured for 5 h averaging each point over 5 s. The latter measurement was performed in a standard, stainless steel CC with the radius of the cup, $r_o = 8.25$ mm, and the radius of the bob, $r_i = 5.25$ mm. Sandpaper was glued to the surface of both bob and cup to prevent slip. Prior to the start of the acquisition of the global flow curves each sample was pre-sheared for 3 min at 30 s⁻¹ and, thereafter, exposed to stress measurements under a shear rate sweep from 100 s⁻¹ to 0.01 s⁻¹ for the down-sweep branch and directly after from 0.01 s⁻¹ to 100 s⁻¹ for the upsweep branch. A total of 20 points per decade in shear rate were recorded, averaging each stress value over 5 s.

5.2.6. Flow-MRI

¹H MRI velocimetry measurements along the flow direction were performed using an in-house developed microcapillary flow-MRI platform (Fig. 5.1d), inserted in a wide-bore Avance NEO Bruker spectrometer operating at 14 T. Excitation and detection of the ¹H signal was performed with a saddle r.f. coil with an inner diameter of 1.2 mm, in the Micro-5 microimaging gradient system (Bruker BioSpin) with maximum gradient intensity of 3 T m⁻¹ along all three directions. For the experiments, the fluid of interest is placed in the reservoir and the target pressure is applied by the pressure controller (Elveflow) in the range 0–8 bar. The sample flows in the connecting tubing (diameter, $w = 0.9$ mm; BGB Analytik) and through the connected glass microcapillary ($w = 0.25$ mm, length, $L = 14.5 \pm 0.2$ cm; BGB Analytik), positioned inside the saddle coil. The measurements were carried out at a constant temperature of 20 °C which is set by the temperature of the cooling water of the triple-axis MRI gradients.

MRI velocimetry measurements were performed using a 2D Pulsed Field Gradient Spin Echo (PFG-SE) sequence,²³ within a 3 mm thick slice in the flow direction. The field-of-view (FOV) in the read and phase directions was 0.6 x 0.6 mm², and by correspondingly acquiring 64 x 64 pixels, isotropic spatial resolution of 10 μm could be obtained. Since SF oil in the MFC dispersions yields resolved ¹H NMR signals at 14 T, to avoid chemical shift artefacts, a 90° chemically-selective, low-power, saturation pulse was used in all flow-MRI measurements with a bandwidth of 1 kHz and frequency offset of 2.46 kHz.²⁴ 2D ¹H MRI maps of velocities in the flow direction were acquired with the echo time $T_E = 11$ ms and repetition time $T_R = 2$ s. The duration of the velocity-encoding gradient pulses, and their inter-pulse spacing, were $\delta = 1$ ms and $\Delta = 4$ ms, respectively. Using a number of scans $NS = 2$, the total experiment time

per velocity map was 4 min. For each sample, three consecutive velocity maps were acquired per P_{app} value.

For the data analysis, 2D velocity maps were radially averaged to yield 1D velocity profiles. The averaging was performed in MATLAB, with the pixel values binned based on their distance from the center of the capillary. The number of bins was set to 64. As a result, the spatial resolution of the 1D profiles is twice that of the original 2D maps.

5.2.7. Local flow curves

Local flow curves of the three 15 wt% MFC dispersions were obtained by calculating the local shear rates, $\dot{\gamma}(x)$, from the slopes, $\partial V_x / \partial x$, of the velocity profiles, where x is the position in the radial direction of the capillary. The local stresses were calculated as $\sigma(x) = \Delta P x / 2L$, where ΔP is the pressure drop between the inlet and outlet of the capillary, measured with pressure sensors. The sensors were connected to the inlet and outlet of the capillary with an intermediate tubing ($w = 0.9$ mm and $L = 10$ cm). ΔP was measured in a separate experiment using a setup located outside the MRI spectrometer, identical to that used for flow-MRI measurements.

5.3. Results and discussion

5.3.1. Evolution of multiscale network structure during shear

We first measured the global flow behavior of the 15 wt% MFC dispersion in a mm-sized gap, and concomitantly recorded the changes in ACNT and the mean aggregate size.

As can be seen from Fig. 5.2a, for the first few minutes a rapid decrease in stress is observed, as the sample abruptly transitions from solid-like to liquid-like, flowing regime. This observation contrasts with the results of Nikolaeva *et al.*,¹⁴ where the yield stress of fresh MFC dispersions at the start-up of shear was close to zero, signifying primarily liquid-like properties. The authors ascribed the initial absence of yield stress to fully dispersed and non-networked crystal nanoplatelets within the sample. Here, however, the initial high stress clearly demonstrates the presence of a transient network. We attribute the differences in the initial sample properties to the different storing conditions of the stock sample. The here used storage temperature

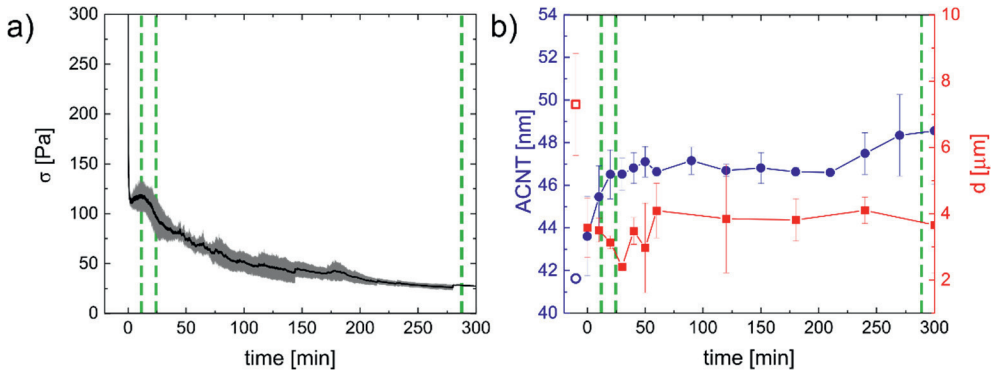


Figure 5.2: a) Stress response of the 15 wt% MFC dispersion under continuous shear at $\dot{\gamma} = 5 \text{ s}^{-1}$ for 5 h in a 4 mm CC at RT. The gray shaded area represents the experimental error within 7 repeats. Plot in b) shows the shear-induced microstructural changes, namely the ACNT and the average crystal aggregate diameter, d , with the empty symbols representing the measurements on a stock sample. The error bars show the deviation between 2 repeats. Green dashed lines mark the time points at which local velocimetry flow-MRI and global flow curve measurements were performed.

of 4 °C, as opposed to -20 °C used in the study of Nikolaeva *et al.*,¹⁴ was insufficient to prevent the formation of a weak network, resulting in the initial transient, solid-like sample properties. Curiously, however, the difference in the initial sample properties did not influence its flow behavior, likely because the used chilled storage conditions prevented recrystallization and enabled retaining thin nanoplatelets. In agreement with the results previously observed for MFC dispersions,^{14,15} we observe a weak-link network formation during the first ~ 20 min of shear at 5 s^{-1} , as visible by an increase in stress. This period coincides with a rapid nanoplatelet recrystallization and a decrease of mean aggregate size to $(2.4 \pm 0.1) \mu\text{m}$ (Fig. 5.2 and Fig. S5.1 in section 5.5). For the remaining shear time, stress undergoes a constant decrease and the sample loses strength due weakening of the network as a result of further recrystallization and aggregation of crystal nanoplatelets.

We also recorded the ACNT and d for a sample at 4 °C, taken directly from the stock 15 wt% MFC dispersion, *i.e.* one that has not experienced any temperature changes or shear as a result of experimental preparation (empty symbols in Fig. 5.2b). By comparing these datapoints to those recorded right before shear start-up, at $t = 0$ min, it can be seen that recrystallization and a big part of the initial destruction of the crystal nanoplatelet aggregates happens as a result of sample handling, *e.g.*,

transfer between flow geometries, and warming of the sample to RT, the condition under which all experiments were performed.

5.3.2. Global vs. local flow behavior

In this section we study the global, non-confined, and local, confined flow behavior of 15 wt% MFC dispersions with distinct structural properties: a non-pre-sheared sample (**PS0**), with thin crystal nanoplatelets forming a space-filling network, a sample pre-sheared for 20 min (**PS20**), with thicker nanoplatelets and an evolving network, and a sample pre-sheared for 280 min (**PS280**), with thick nanoplatelets and equilibrated, weak-link aggregate network. The microstructurally distinct samples **PS0**, **PS20**, **PS280** are indicated with green dashed lines in Figure 5.2. The global flow curves of all samples are presented in Figure 5.3. We found that the flow behavior of all three samples is well described by the HB model of the form $\sigma_y + K\dot{\gamma}^n$, where σ_y is the yield stress, K is a proportionality constant with the units of $\text{Pa s}^{1/n}$ and n is a dimensionless power law index.²⁵ The fitting parameters are summarized in Table 5.1.

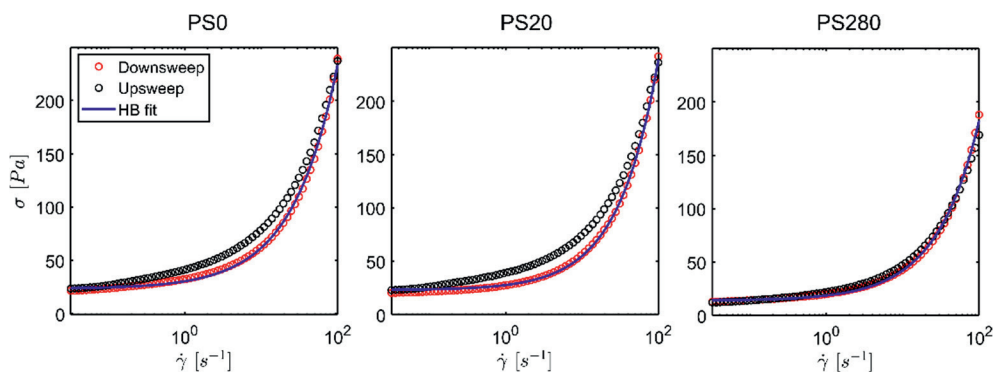


Figure 5.3: Global flow curves of the 15 wt% MFC dispersions subjected to increasing duration of pre-shear, acquired by sweeping the shear rates from high to low (red symbols), and immediately thereafter from low to high (black symbols). The down sweep curve was fitted with the HB model (solid line).

Table 5.1: Parameters obtained from fitting the global flow curves of the 15 wt% MFC samples using the HB model.

	σ_y [Pa]	K [$\text{Pa s}^{1/n}$]	n
PS0	23.4 ± 0.3	7.0 ± 0.2	0.74 ± 0.01
PS20	21.6 ± 0.2	5.2 ± 0.1	0.81 ± 0.01
PS280	14.6 ± 0.3	4.4 ± 0.1	0.79 ± 0.01

Notably, the values of both parameters, σ_y and K decrease by a factor of 1.6 on going from sample **PS0** to **PS280**. This decrease reveals weakening of the network as a result of pre-shear treatment, in agreement with the continuous shear experiments. Notably, the minor or absent hysteresis in the global flow curves along with the good agreement with the HB model suggest a simple HB flow behavior for all three samples.

With the aim to gain insight into the local flow behavior we used microcapillary flow-MRI and studied how the microstructural changes shown in Fig. 5.2b affect flow in sub-mm confined flow regime. We note that, aside from the controlled amount of pre-shear, in flow-MRI measurements the sample experiences additional shear while flowing in the connecting tubing before it reaches the microcapillary where the signal is recorded (Fig. 5.1d). To account for this additional shear, we have estimated the strain accumulated in each sample during the flow in the tubing (Table S5.1 in the SI), which could be translated to additional few minutes of the controlled pre-shear, as reflected in the positions of the green dashed lines in Fig. 5.2. The obtained mean velocity profiles for the three samples are presented in Fig. 5.4a – c. The results clearly demonstrate that longer pre-shear times yield faster flowing samples, at equal pressures. The increase in velocities is caused by weakening of the fat network during the pre-shear period, and is in agreement with the global stress measurements presented in the previous section. Additionally, the obtained velocity profiles reveal that longer pre-shear times result in samples which are more prone to slippage at the smooth glass walls, as visible from the non-zero fluid velocity at the capillary walls for samples **PS20** and **PS280**. The increase in wall slip is likely due to shear-induced increase in the mean size of the microstructure. Aside from the fluid-wall interaction, the local flow measurements reveal that both pre-sheared samples (**PS20** and **PS280**) exhibit flow profiles typical for HB fluids, namely, with plug flow in the center, where stress is below the yield stress of the sample, and shear increasing with stress towards the walls.^{19,26} On the other hand, sample **PS0** shows a markedly distinct behavior, forming shear bands at the outer walls (see inset in Fig. 5.4a), whose thickness increases with decreasing pressures. We note that in contrast to a typical non-flowing band forming in regions where the stress falls below the yield stress of the sample, the non-flowing bands observed here form in the highest stress region of the capillary.²⁷⁻²⁹ Formation of similar bands in high stress regions of a CC geometry was also observed by Andrade *et al.*³⁰ for waxy oil suspensions. However, the authors did not pursue the microstructural origin of such effect.

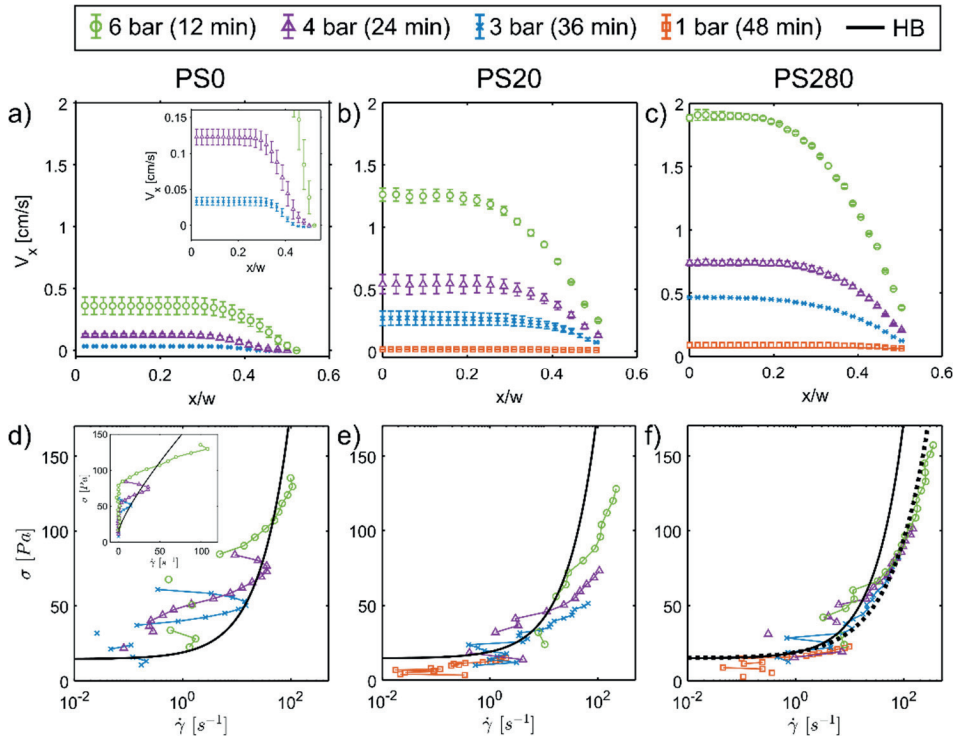


Figure 5.4: Top: ^1H flow-MRI velocity profiles plotted against the normalized position x/w , and bottom: local (symbols) and global (solid lines) flow curves of samples **PS0** (a and d), **PS20** (b and e) and **PS280** (c and f). The pressures were applied consecutively as indicated in the legend. The error bars in plots a – c originate from fluctuations of flow in time, over the measurement timeframe of 12 min. Solid lines in plots d – f were calculated using the parameters σ_y , K and n obtained from fits of the measured global flow curves with the HB model. The dotted line in f is the HB curve with the parameter n adjusted from 0.7 to 0.8.

To further explore the rheological properties of the three samples, we analyzed the local flow curves and compared them with the respective global HB fits (Fig. 5.4d – f). Unsurprisingly, the local flow curves of sample **PS0** strongly deviate from the simple HB flow behavior suggested by the global measurements, due to the presence of the high-stress shear bands. For samples **PS20** and **PS280**, the analysis of the local flow curves reveals a collapse onto a master curve only for the latter, indicating simple HB flow behavior.²⁴ In contrast, for sample **PS20** a time-dependent flow behavior is observed under each pressure, and can be modelled by separate HB equations (Fig. S5.2 in section 5.5.2). The obtained decreasing σ_y values with

decreasing pressures (Table 5.2), and correspondingly longer shear times suggest a time and shear-history dependent flow properties typical for thixotropic fluids.

Table 5.2: Decrease of σ_y of sample **PS20** with shearing time. The constant error in the applied pressures is an average fluctuation of the pump during an experiment.

Time [min]	$P_{app} \pm 0.01$ [bar]	σ_y [Pa]
12	6.00	32 ± 7
24	4.00	19 ± 6
36	3.00	8 ± 4
48	1.00	6 ± 1

The thixotropic behavior of sample **PS20** is further evident from the evolution of maximum velocities, V_{max} , in individual velocity profiles acquired under each pressure (Fig. 5.5). For sample **PS20** V_{max} decreases with time under each pressure, while for sample **PS280** flow remains constant except at 1 bar, where plug flow develops after 4 min due to close proximity to yield stress. Finally, we note that the local flow curves of sample **PS280**, despite a small deviation from the global flow curve, can be fitted with the same HB parameters and power law index, n around 0.7-0.8. This possibly originates from a difference in wall slip conditions in global vs. local flow measurements. Interestingly, the good agreement between the global and local flow measurements of sample **PS280** marks the absence of flow cooperativity

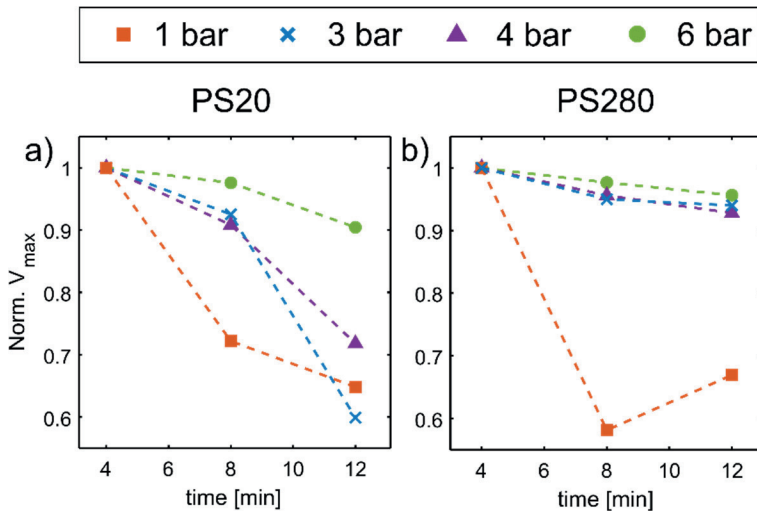


Figure 5.5: Plots of the maximum velocities, V_{max} present in the three, consecutively acquired velocity maps for samples **PS20** and **PS280**. The V_{max} values were normalized to the highest value within one applied pressure.

effects.¹⁸ This stands in contrast with the cooperative flow behavior of FCDs that were prepared by melt-cooling, thus consisting of fractal networks of aggregates, which are approximately 7 times larger than the aggregates found in 15 wt% MFC dispersions.⁸ We attribute the absence of cooperativity effects in the 15 wt% MFC dispersions to their non-fractal nature and much smaller aggregate sizes, compared to the FCDs.

5.3.3. Structural underpinning of the confined local flow behavior

Having studied the micro- and nanostructure as a function of shear time, in this section we propose a mechanism to explain the dynamic response of the multiscale structure to translational flow in the microcapillaries. The structural hypothesis is schematically presented in Fig. 5.6, and is based on the observed bulk rheological properties and spatial profile, magnitude and time-stability of the MRI velocities. Firstly, we hypothesise that the existence of shear bands observed in the flow of sample **PS0** originates from the coexistence of two microstructurally distinct phases,

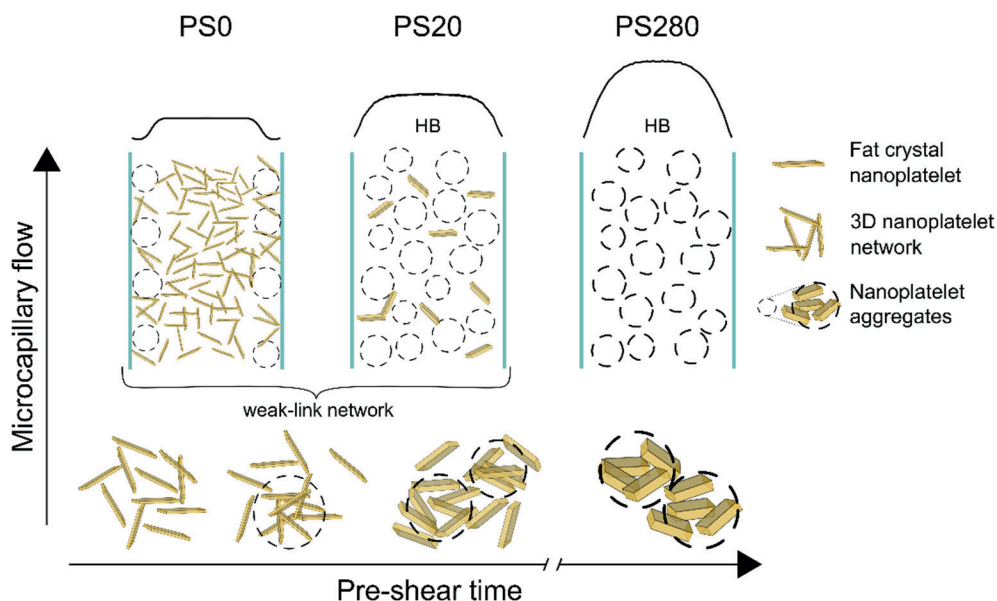


Figure 5.6: Schematic depiction of fat crystal nanoplatelets recrystallization, network formation and aggregation upon increasing the pre-shear time (horizontal axis) and the resulting flow behavior as observed by microcapillary flow-MRI (vertical axis). The yellow rectangles of increasing thickness represent the crystal nanoplatelets undergoing shear-enhanced Ostwald ripening and the dashed circles represent nanoplatelet aggregates. Between the aggregates a weak-link network composed of thin platelets is depicted.

resulting from subtle differences in the shear history of the material flowing close to the walls and in the center of the tubing. High shear at the walls causes an increased recrystallization rate and results in the formation of a weak-link aggregate network in proximity to the walls. The presence of the network results in an increased σ_y and thus formation of a static band. In contrast, in the central region of the capillary the nanoplatelets are exposed to much lower shear, and thus remain thin and form a non-aggregated, space-filling network, displaying plug flow. Secondly, we ascribe the observed time-dependent flow behavior of sample **PS20** to the presence of the weak-link network between the aggregated nanoplatelets. The network weakens during flow, resulting in the observed loss of yield stress with shear time. Finally, in sample **PS280** thick platelets form aggregates in the absence of the weak-link network, destroyed during an extensive pre-shear period. Due to the absence of the network the sample behaves as a simple HB fluid.

5.4. Conclusions

We have studied the sub-mm confined flow of 15 wt% MFC dispersions, exposed to various durations of pre-shear ranging from null to ~ 5 h. The combined global rheology and flow-MRI measurements revealed that the weak-link aggregate network, responsible for the sample's yield stress properties, weakens as a result of increasing pre-shear time, which results in fluidized, faster flowing samples. With SAXD and hyperspectral Raman measurements we have confirmed the shear induced evolution of the multiscale structure, namely nanoplatelet recrystallization and aggregation. As a result of these structural changes we have observed a gradual shift of the fundamental rheological properties, as a function of increasing the pre-shear time, from non-HB to simple HB flow behavior via a thixotropic intermediate. With the unique insight into the local flow behavior of the optically-opaque MFC dispersions offered by flow-MRI, we have observed the formation of an uncommon type of shear banding in a non-pre-sheared sample. We propose that the shear bands result from a coexistence of aggregated, networked platelets in the high shear regions in proximity to the walls and thin platelets, forming a space-filling network in the low-shear regions in the center of the capillary. We foresee that the here presented approach of combining MRI velocimetry with capillary flow can be exploited to assess the impact of shear in variable flow gap sizes. We believe that this will enable a better understanding of the underlying multiscale structural dynamics and hence a more accurate process design of fat-based products. Ongoing and future

work will involve studies of diffusion under flow in an attempt to probe for the flow-induced alignment of the crystalline nanoplatelets.

Author Contributions

Conceptualization: K. W. M., C. T., J. A. D. and J. P. M. v. D.; experimental measurements and data analysis: K. W. M., R. d. A.; validation: K. W. M.; formal analysis: K. W. M.; writing — original draft preparation: K. W. M.; writing — review and editing: C. T., J. A. D. and J. P. M. v. D.; visualization: K. W. M.; supervision: C. T., J. P. M. v. D., J. A. D.

Acknowledgements

We acknowledge Upfield (Wageningen, The Netherlands) for kindly providing the MFC powders. This project was supported by the uNMR-NL Grid: A distributed, state-of-the-art Magnetic Resonance facility for the Netherlands (NWO grant 184.035.002). We thank John Philippi for his expert technical support and Frank Vergeldt for fruitful discussions on MRI velocimetry. Karin Schroën is thanked for fruitful discussions on phenomena in microfluidics flow.

References

- (1) Acevedo, N. C.; Block, J. M.; Marangoni, A. G. Critical laminar shear-temperature effects on the nano- and mesoscale structure of a model fat and its relationship to oil binding and rheological properties *Faraday Discuss.* **2012**, *158*, 171-194.
- (2) Marangoni, A. G.; Acevedo, N.; Maleky, F.; Co, E.; Peyronel, F.; Mazzanti, G.; Quinn, B.; Pink, D. Structure and functionality of edible fats *Soft Matter* **2012**, *8* (5), 1275-1300.
- (3) Marangoni, A. G.; van Duynhoven, J. P. M.; Acevedo, N. C.; Nicholson, R. A.; Patel, A. R. Advances in our understanding of the structure and functionality of edible fats and fat mimetics *Soft Matter* **2020**, *16* (2), 289-306.
- (4) Ramel, P. R. R.; Peyronel, F.; Marangoni, A. G. Characterization of the nanoscale structure of milk fat *Food Chem.* **2016**, *203*, 224-230.
- (5) Campos, R.; Ollivon, M.; Marangoni, A. G. Molecular Composition Dynamics and Structure of Cocoa Butter *Cryst. Growth Des.* **2010**, *10* (1), 205-217.
- (6) Gregersen, S. B.; Miller, R. L.; Hammershøj, M.; Andersen, M. D.; Wiking, L. Texture and microstructure of cocoa butter replacers: Influence of composition and cooling rate *Food Struct.* **2015**, *4*, 2-15.
- (7) Maleky, F.; Smith, A. K.; Marangoni, A. Laminar Shear Effects on Crystalline Alignments and Nanostructure of a Triacylglycerol Crystal Network *Cryst. Growth Des.* **2011**, *11* (6), 2335-2345.
- (8) Milc, K. W.; Dijkman, J. A.; van Duynhoven, J. P. M.; Terenzi, C. Quantifying cooperative flow of fat crystal dispersions *Soft Matter* **2022**, *18* (14), 2782-2789.
- (9) Münüklü, P.; Jansens, P. J. Particle formation of an edible fat (rapeseed 70) using the supercritical melt micronization (ScMM) process *J. Supercrit. Fluids* **2007**, *40* (3), 433-442.
- (10) Acevedo, N. C.; Marangoni, A. G. Characterization of the Nanoscale in Triacylglycerol Crystal Networks *Cryst. Growth Des.* **2010**, *10* (8), 3327-3333.

- (11) Martens, K. J. A.; van Dalen, G.; Heussen, P. C. M.; Voda, M. A.; Nikolaeva, T.; van Duynhoven, J. P. M. Quantitative Structural Analysis of Fat Crystal Networks by Means of Raman Confocal Imaging *J. Am. Oil Chem. Soc.* **2018**, *95* (3), 259-265.
- (12) Awad, T. S.; Rogers, M. A.; Marangoni, A. G. Scaling Behavior of the Elastic Modulus in Colloidal Networks of Fat Crystals *J. Phys. Chem. B* **2004**, *108* (1), 171-179.
- (13) Acevedo, N. C.; Marangoni, A. G. Nanostructured Fat Crystal Systems *Annu. Rev. Food Sci. Technol.* **2015**, *6* (1), 71-96.
- (14) Nikolaeva, T.; den Adel, R.; van der Sman, R.; Martens, K. J. A.; Van As, H.; Voda, A.; van Duynhoven, J. P. M. Manipulation of Recrystallization and Network Formation of Oil-Dispersed Micronized Fat Crystals *Langmuir* **2019**, *35* (6), 2221-2229.
- (15) Nikolaeva, T.; den Adel, R.; Velichko, E.; Bouwman, W. G.; Hermida-Merino, D.; Van As, H.; Voda, A.; van Duynhoven, J. P. M. Networks of micronized fat crystals grown under static conditions *Food Funct.* **2018**, *9* (4), 2102-2111.
- (16) Narine, S. S.; Marangoni, A. G. Fractal nature of fat crystal networks *Phys. Rev. E* **1999**, *59* (2), 1908-1920.
- (17) Narine, S. S.; Marangoni, A. G. Mechanical and structural model of fractal networks of fat crystals at low deformations *Phys. Rev. E* **1999**, *60* (6), 6991-7000.
- (18) Goyon, J.; Colin, A.; Ovarlez, G.; Ajdari, A.; Bocquet, L. Spatial cooperativity in soft glassy flows *Nature* **2008**, *454*, 84-87.
- (19) Goyon, J.; Colin, A.; Bocquet, L. How does a soft glassy material flow: finite size effects, non local rheology, and flow cooperativity *Soft Matter* **2010**, *6* (12), 2668-2678.
- (20) Johansson, D.; Bergenståhl, B. Sintering of fat crystal networks in oil during post-crystallization processes *J. Am. Oil Chem. Soc.* **1995**, *72* (8), 911-920.
- (21) den Adel, R.; van Malssen, K.; van Duynhoven, J. P. M.; Mykhaylyk, O. O.; Voda, A. Fat Crystallite Thickness Distribution Based on SAXD Peak Shape Analysis *Eur. J. Lipid Sci. Technol.* **2018**, *120* (9), 1800222.
- (22) Géraud, B.; Jørgensen, L.; Ybert, C.; Delanoë-Ayari, H.; Barentin, C. Structural and cooperative length scales in polymer gels *Eur. Phys. J. E* **2017**, *40* (5), 1-10.
- (23) Callaghan, P. T. Rheo-NMR and velocity imaging *Curr. Opin. Colloid Interface Sci.* **2006**, *11* (1), 13-18.
- (24) Nikolaeva, T.; Vergeldt, F. J.; Serial, R.; Dijkman, J. A.; Venema, P.; Voda, A.; van Duynhoven, J. P. M.; Van As, H. High Field MicroMRI Velocimetric Measurement of Quantitative Local Flow Curves *Anal. Chem.* **2020**, *92* (6), 4193-4200.
- (25) Herschel, W. H.; Bulkley, R. Konsistenzmessungen von Gummi-Benzollösungen *Kolloid-Zeitschrift* **1926**, *39* (4), 291-300.
- (26) Isa, L.; Besseling, R.; Poon, W. C. K. Shear Zones and Wall Slip in the Capillary Flow of Concentrated Colloidal Suspensions *Phys. Rev. Lett.* **2007**, *98* (19), 198305.
- (27) Ovarlez, G.; Rodts, S.; Ragouilliaux, A.; Coussot, P.; Goyon, J.; Colin, A. Wide-gap Couette flows of dense emulsions: Local concentration measurements, and comparison between macroscopic and local constitutive law measurements through magnetic resonance imaging *Phys. Rev. E* **2008**, *78* (3), 036307.
- (28) Raynaud, J. S.; Moucheront, P.; Baudez, J. C.; Bertrand, F.; Guilbaud, J. P.; Coussot, P. Direct determination by nuclear magnetic resonance of the thixotropic and yielding behavior of suspensions *J. Rheol.* **2002**, *46* (3), 709-732.
- (29) Hollingsworth, K. G.; Johns, M. L. Rheo-nuclear magnetic resonance of emulsion systems *J. Rheol.* **2004**, *48* (4), 787-803.
- (30) Andrade, D. E. V.; Coussot, P. Brittle solid collapse to simple liquid for a waxy suspension *Soft Matter* **2019**, *15* (43), 8766-8777.

5.5. Supporting information

5.5.1. Quantification of the mean aggregate size.

In Fig. S5.1 we present the images of solid fat distribution in 15 wt% MFC dispersions subjected to increasing shear durations, acquired via hyperspectral Raman imaging. The analysis of the radially averaged 2D autocorrelation functions enabled obtaining estimates of the mean crystal nanoplatelets aggregate sizes. Interestingly, in samples sheared for 20 – 60 min we have observed a degree of structural directionality, visible in the Raman images and the respective 2D autocorrelation functions.

5.5.2. Local flow behavior of 15 wt% MFC dispersions

Samples subjected to flow-MRI experiments experience shear while flowing in the connecting tubing, prior to reaching the capillary, where the velocity profiles are measured. With the aim to account for this additional shear treatment in samples **PS0**, **PS20**, and **PS280**, we have estimated the strain that each sample accumulates during flow in the tubing, as $\gamma = t \cdot \bar{\dot{\gamma}}_{tube}$ where γ is the strain, t is the time it takes for the sample to reach the capillary and $\bar{\dot{\gamma}}_{tube}$ is the average shear rate in the tube. Both t and $\bar{\dot{\gamma}}_{tube}$ were calculated using the average velocities measured in the capillaries, \bar{v}_{cap} at $P_{app} = 6$ bar, according to $t = \bar{v}_{cap} / l_{tube}$ and $\bar{\dot{\gamma}}_{tube} = \bar{v}_{cap} / r_{tube}$, where l_{tube} and r_{tube} is the length and radius of the tube, equal to 215 cm and 0.9 mm, respectively. Finally, we have calculated the equivalent additional pre-shear time, t_{eq} , one would have to apply at $\dot{\gamma} = 5 \text{ s}^{-1}$ to accumulate the same amount of strain. The results of the calculations are summarized in Table S5.1.

Table S5.1. Summary of the calculations of the strain accumulated by the sample, during flow in the connecting tubing of the flow-MRI platform, and equivalent additional pre-shear time.

	\bar{v}_{tube} [cm/s]	$\bar{\dot{\gamma}}_{tube}$ [s^{-1}]	Flow time [min]	γ [%] $\times 10^3$	t_{eq} [min]
PS0	0.3	7	12	504	16
PS20	0.9	22	4	528	17
PS280	1.3	33	3	594	20

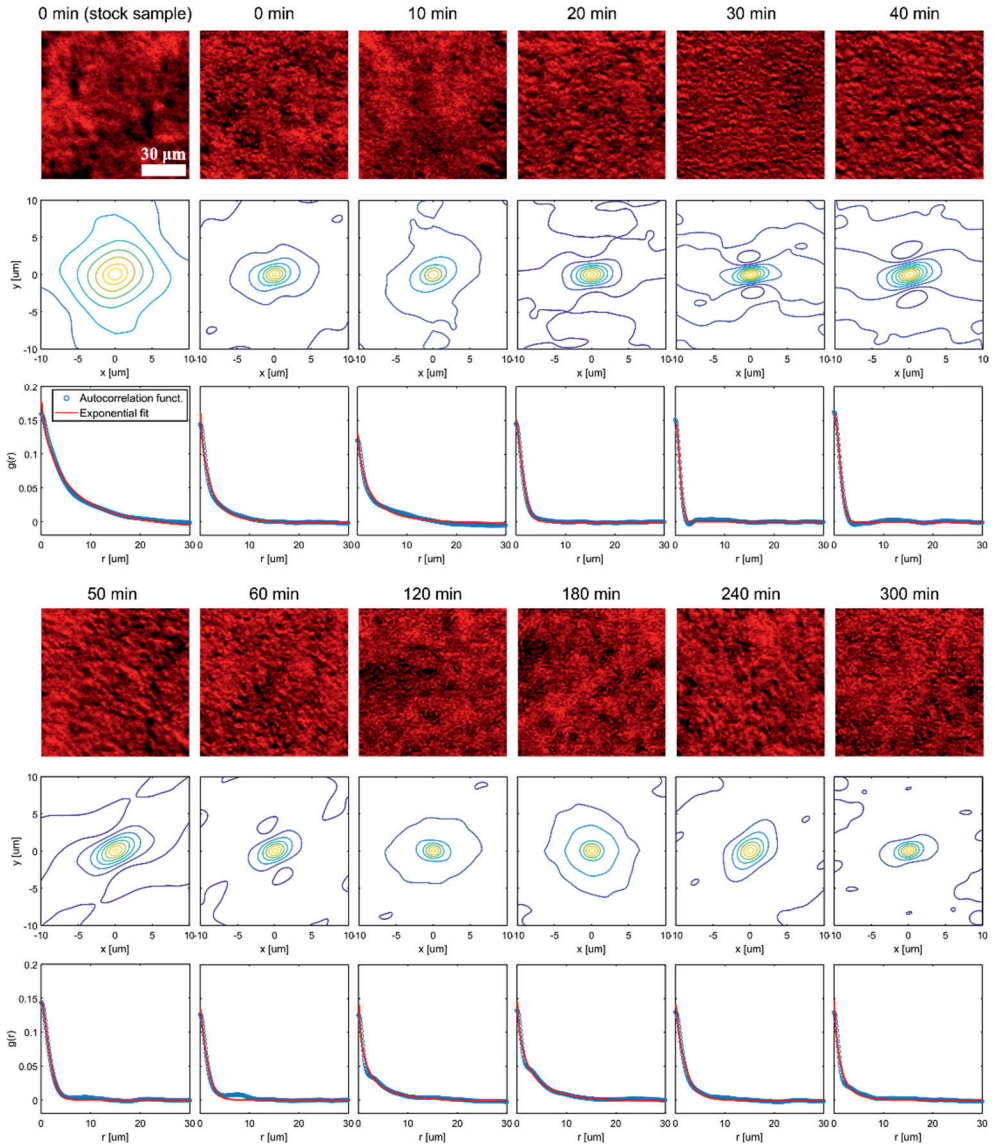


Figure S5.1. Raman images of the 15% MFC dispersions as a function of shear time, as indicated above the images. Below each image a corresponding calculated 2D autocorrelation function and its radial average, fitted with Eq. 5.1 are shown.

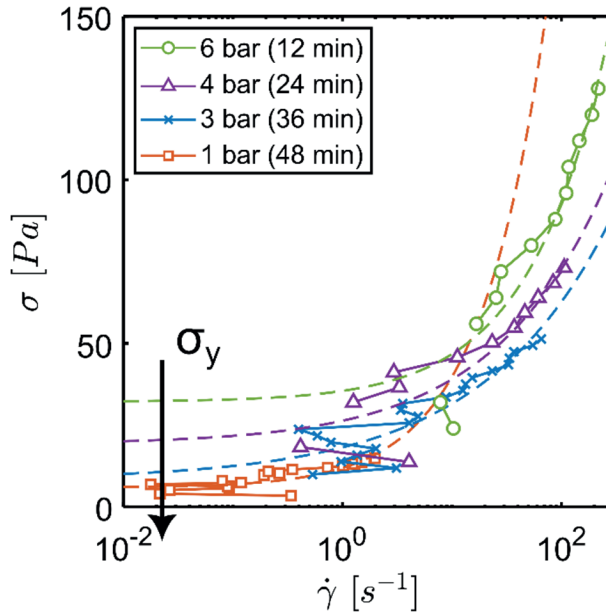


Figure S5.2. Local flow curves of sample **PS20**, calculated from the 1H MRI velocity profiles, individually fitted with the HB model (dashed lines) with the aim to quantify the evolution of the yield stress as a function of time.

CHAPTER

6

General discussion



6.1. Main findings and conclusions

The first goal of this thesis work was to develop MRI velocimetry platforms for unlocking the experimental characterization of sub-mm flow of complex fluids under a range of flow conditions. Secondly, the aim was to experimentally and theoretically characterize cooperativity effects, governing strongly confined flow of soft, particulate fluids. Both aims were motivated by the necessity to characterize and improve our understanding of the mechanisms governing flow of complex fluids in strong confinements. Such in-depth understanding of strongly confined flow is a prerequisite for applications ranging from soft matter studies of complex fluids using microfluidics to extrusion of protein dispersions in 3D food printing.^{1,2}

To this aim, in **Chapter 2**, a 500 μm gap CC geometry was developed with 10-fold improved mechanical stability of the rotating bob, enabling the acquisition of velocity profiles with MRI resolution up to $\sim 10 \mu\text{m}/\text{pixel}$. A water circuit integrated in the CC for temperature control in the range 15 – 45 °C made it possible to study the effects of, *e.g.*, crystallization or gelation on flow properties. The importance of such studies is emphasized by the recent developments of temperature-controlled CCs for rheo-NMR³ and rheo-Small-Angle-Scattering techniques.⁵ The capabilities of the CC were demonstrated in a case study of strongly confined flow of a 27 wt% FCD, a common precursor in food manufacturing. The developed CC allowed for an easier identification of intrinsic flow instabilities than the commercially available mm-sized CCs. In the new in-house developed CC, due to the narrow stress distribution, curvature in the velocity profiles can be readily ascribed to thixotropic properties or cooperativity effects, while in the mm-sized gap CC these effects are entangled with the effects of wide stress distribution. The temperature control capability makes it possible to identify instability in the flow of the FCD sample at 30 °C, absent at 15 °C. The time-dependent flow behavior thus likely originated from recrystallization of fat platelets into larger aggregates, triggered by the elevated temperature. The sub-mm rotational rheo-MRI platform opened the possibility to quantify cooperativity effects in real-life complex fluids, including food precursors and emulsions, as model systems for paints and cosmetics.

In **Chapter 3**, the advantages of sub-mm rotational rheo-MRI platform were exploited in a detailed investigation of the sub-mm flow of 27 wt% FCDs as a function of the microstructure size, controlled by the crystallization rate. FCDs with an average aggregate size, d below 10% of the gap size, w , were found to exhibit significant

velocity enhancement and position-dependent viscosities, originating from flow cooperativity. The high spatial resolution of the velocimetry data, achieved with the mechanically stable bob, allowed for accurate quantification of cooperativity lengths, ξ . Importantly, the obtained ξ values followed a trend predicted by the KEP model, diverging at the fluids' yield stress, σ_y , measured by classical rheology.⁶ The 27 wt% FCD sample obtained with slowest explored crystallization rates, with d approaching 50% of w , did not exhibit flow cooperativity and was found to flow according to a simple HB model.

The challenge in the mutual alignment of the centers of the cup and the bob, accentuated by the length of the drive shaft in the rotational rheo-MRI setup, limits the available flow gap size to 500 μm for a CC geometry. Hence, to be able to study cooperativity under even stronger confinement and in fluids with $d < 10 \mu\text{m}$, in **Chapter 4**, a microcapillary rheo-MRI platform was developed. The platform is based on cylindrical glass capillaries as the flow geometry, which enables easy control over the gap size down to $\sim 50 \mu\text{m}$, and allows for chemical modification of the walls, to alter fluid-wall interactions. The platform was used to study cooperativity effects in 0.5 wt% Carbopol with $d \approx 2 \mu\text{m}$, and in 15 wt% FCDs as a function of the flow confinement degree, d/w . In the 15 wt% FCDs the number of particles participating in cooperative rearrangements was found to increase with increasing P_{app} , in contrast to 0.5 wt% Carbopol where a constant ξ , independent of flow conditions was found. Additionally, in 15 wt% FCDs ξ was found to decrease with decreasing w . The developed platform thus broadened the range of fluids for which cooperative flow can be studied, extending the range of possible particle sizes and accessible particle-wall interactions. Additionally, the platform opened the possibility to characterize flow-induced aggregation or alignment of particles.

In **Chapter 5**, the microcapillary rheo-MRI platform was used to study sub-mm confined flow of MFC dispersions, a novel ingredient in production of fat-based products and an alternative to traditionally manufactured melt-cool FCDs. Rheological properties of the 15 wt% MFC dispersions were characterized in strong confinement as a function of shear history. The study revealed that the pre-shear time can be used to control the flow properties of the 15 wt% MFC dispersions, which evolve from non-HB for non-pre-sheared samples, to simple HB for extensively pre-sheared samples, via a thixotropic intermediate. Additionally, in contrast to traditionally manufactured FCDs, no cooperativity effects were identified in the 15

wt% MFC dispersions, which was ascribed to the non-fractal nature of the crystal aggregates in the latter fluid.

The remaining part of this chapter is divided into two sections. Firstly, in section 6.2 the two developed rotational and microcapillary flow-MRI platforms are mutually compared in terms of the attainable experimental capabilities, such as the available spatial resolution and applicability to samples depending on their viscosity and thixotropy. Section 6.2.3 contains perspectives for technical improvements and extensions of the experimental capabilities of the two platforms. In section 6.3, results concerning cooperative flow of fluids investigated throughout this thesis work are compiled, and the observed trends in relation to the properties of the microstructure and of the geometry are discussed. These results are compared with cooperativity effects reported in the literature for various fluids, with the aim to draw general conclusions on factors governing flow cooperativity. In section 6.3.2 alternative approaches to modeling of flow cooperativity are explored as an outlook for more accurate quantification of ξ . This includes a comparison of modelling confined flow with a stress-dependent and independent ξ parameter, and an attempt to concomitantly account for cooperativity effects and thixotropy in a flow geometry with a non-uniform stress distribution. Finally, potential perspectives for future research are proposed regarding further elucidation of the dependence of cooperativity on flow conditions and on the physico-chemical properties of the involved fluid.

6.2. Considerations of the achieved technical developments

During this thesis work, two flow-MRI setups were developed, validated, and applied: a temperature-controlled, 500 μm gap CC for rotational rheo-MRI measurements and a microcapillary rheo-MRI platform with capillaries of diameters 100 – 540 μm . Both setups make it possible to study flow of complex fluids in well-controlled, sub-mm confinement conditions with spatial resolution down to $\sim 10 \mu\text{m}/\text{pixel}$. However, the different flow geometries and flow driving conditions may render one flow platform more suitable and applicable for certain studies over the other. With the aim to facilitate future experimental design, in the following section a comparison of key characteristics of the flow setups is provided, together with the respective implications on the experimental capabilities.

6.2.1. Experimental capabilities of the flow-MRI setups

One of the most important general considerations in choosing between the rotational or microcapillary rheo-MRI is their possible use in magnets of different field strengths and/or bore sizes. The microcapillary rheo-MRI platform has an obvious advantage, as the length of the connecting tubing or the length of the microcapillaries can be easily scaled. The setup can thus be easily adapted for measurements at low to ultra-high field. In contrast, the sizes of the constituent parts of the rotational rheo-MRI setup are typically designed for a specific NMR spectrometer, with their adaptation to magnets with different field strengths requiring costly adjustments of the drive shaft lengths and dimensions of the CC or the CP geometries.

Secondly, many of the differences in experimental capabilities between the flow-MRI platforms originate from the employed flow geometry. Specifically, the size of the CC or the microcapillary and the resulting filling factor in the active volume of the coil conjointly dictate the dimensionality of the velocimetry data that can be acquired, given the necessity of high spatial and temporal resolution. Although the CC and the CP geometries have the benefit of being directly comparable with classical rheological measurements, they may not be ideally suited for flow MRI measurements. As shown in Figs. 6.1a and 6.1b, in a rotational rheo-MRI setup the volume within the r.f. coil is primarily taken up by the CC itself, with the sample occupying merely 5% of the active volume. In addition, as the radius of the CC is kept relatively large to avoid curvature effects, the resulting large FOV typically makes the acquisition of 2D velocity maps, with sufficient spatial resolution, and using standard signal acquisition strategies, too time-consuming. Hence, in almost all rotational rheo-MRI studies only 1D flow profiles are measured, with approaches such as compressed sensing facilitating the acquisition of 2D measurements.⁷ Finally, to approximate flow in a planar CC, the slice thickness in which a 1D profile is acquired is kept at ~ 1 mm, with all the factors resulting in the effective measured signal originating from $< 1\%$ of the volume within the coil (Fig. 6.1c). This invariably requires long signal averaging times to achieve sufficient signal-to-noise ratio (SNR), in turn decreasing the temporal resolution of the measurements. For a CP similar limitations as for a CC are encountered. In contrast, the microcapillary geometry lends itself much better to flow-MRI measurements, with the sample occupying close to 100% of the volume of the flow geometry. In the 1.2 mm r.f. coil used in this work, the signal originates from up to 20% of the active volume, yielding an improved filling

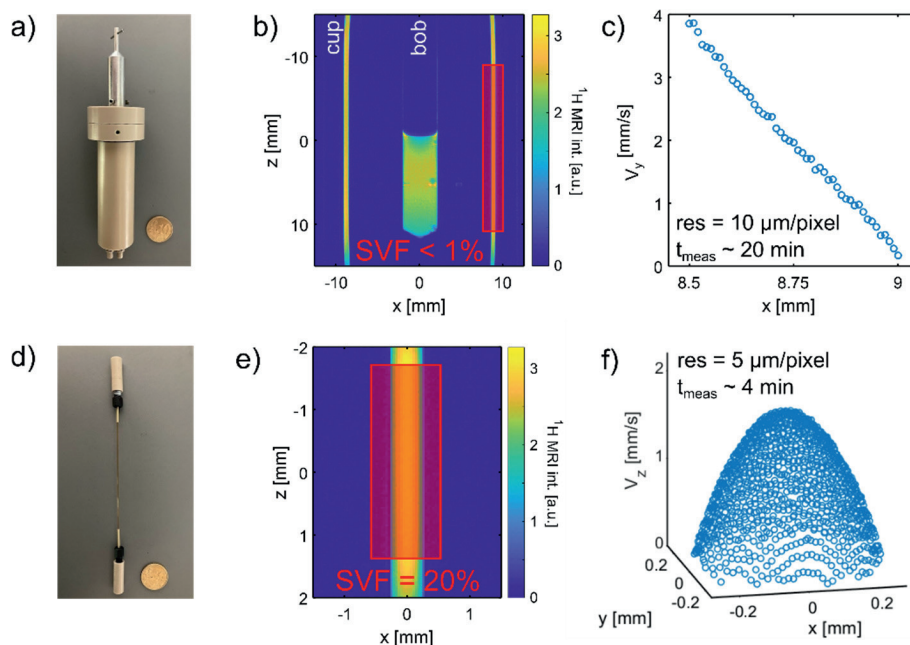


Figure 6.1: Comparison of MRI velocimetry measurements in rotational (top) and translational (bottom) flow-MRI platforms. In a) and d) photographs of the CC and the microcapillary are shown, with a gap size of $500\ \mu\text{m}$. b) and e) depict ^1H MRI RARE images of the respective flow geometries, filled with sunflower oil, with red rectangles representing slices excited during flow measurements. Sample volume fractions (SVF) measured during a typical experiment within each geometry are indicated within each image. c) and f) show a 1D velocity profile and a 2D velocity map acquired with the respective platform, with accessible resolution and experiment time indicated.

factor as compared to the rotational rheo-MRI setup (Figs. 6.1d and 6.1e). Furthermore, the small radius of the capillaries makes it easier to acquire 2D velocity maps, with sufficient SNR and temporal resolution of a few minutes, as sub-mm FOV values can be used (Fig. 6.1f). Notably, the filling factor and sensitivity within both experimental setups can be improved by adopting appropriate r.f. coils, as discussed in the perspectives section. As can be seen, the microcapillary rheo-MRI setup has many advantages over rotational rheo-MRI, including its access to smaller gap sizes or higher MRI sensitivity. Yet, rotational rheo-MRI may be more suitable for studies of samples with high viscosity, or thixotropic properties, rendering the two flow-MRI setups complementary to one another.

6.2.2. Flow-MRI platform and sample's rheology

Flow studies of highly viscous fluids are generally challenging, as flow instabilities such as wall slip are often encountered. For determining the local flow behavior of such samples, the rotational rheo-MRI setup is better suited, as the fluid is inserted directly into the CC where the signal is detected. Conversely, for the microcapillary rheo-MRI platform, the sample has to be pumped through the length of the connecting tubing before it reaches the capillary within the MRI sensitive region. This may take up to even few hours and typically requires the exposure of the sample, the connectors, and the capillary to high pressure drops. Secondly, as complex fluids are often prone to aggregation, the use of microcapillary rheo-MRI may suffer from clogging at the narrow constriction at the entrance of the capillary. When it comes to samples with thixotropic properties, the optimal setup choice depends on the scientific question to be answered. The rotational rheo-MRI setup performs well for time-dependent flow studies of a fixed portion of a fluid, as the same sample volume can be continuously sheared while recording the velocimetry data. This can provide insight into flow-induced network destruction or rejuvenation.^{8,9} In microcapillary rheo-MRI the sample passing through the microcapillary is continuously refreshed, thus, each measurement is done on a different portion of the sample with the same shear history. In other words, in the latter setup, the flow time during the flow-MRI experiment and shear history are decoupled, a property utilized in the study of flow of MFC dispersions as a function of pre-shear time in **Chapter 5**.

The characteristics of both setups are summarized in Table 6.1. In addition to the aforementioned properties, the values for minimum necessary sample volume, and minimum d values for strong confinement conditions are indicated. The relatively high volumes necessary for microcapillary rheo-MRI originate from the open circuit flow conditions.

Table 6.1: Comparison of properties of the developed flow-MRI platforms. The given viscosities are as measured at high shear rates where η approaches a constant, $\dot{\gamma}$ -independent value. Sample volume fractions (SVFs) are calculated by dividing the volume of the sample in the excited slice by the total volume of the r.f. coil.

	Rotational rheo-MRI	Microcapillary rheo-MRI
Adaptability to other magnets and bore sizes	Limited by drive shaft length and size of the CC/CP	Limited by proximity of the pump to the capillary
Measured SVFs	< 1%	20%
Max. sample viscosity	~ 100 Pa s	~ 10 Pa s
Thixotropic samples	Study of flow evolution in time	Flow time and shear history decoupled
Minimum sample volume	0.6 mL	~ 10 mL (flow rate dependent)
Minimum d with strong confinement condition	~ 10 μm	< 1 μm

6.2.3. Perspectives for expanding the capabilities of the setups

The MRI sensitivity of both flow setups can be improved by adjusting the type of r.f. coils used for signal excitation and detection. For rotational rheo-MRI, a surface coil can be employed to improve the filling factor of the sample within the active region, in comparison to the typically used volume coils. For microcapillary rheo-MRI, the temporal resolution and, thus, the sensitivity of the measurements can be improved with stripline resonators.^{10,11} Such approach also ensures closer proximity of the sample to the detector, regardless of the capillary diameter and, thus, offers the possibility to study flow in $w < 100 \mu\text{m}$. Notably, striplines are already widely utilized in spectroscopic NMR techniques, but currently still under development for imaging experiments.

An additional development that would broaden the applicability of both techniques is an expansion of the range of temperatures accessible within the rotational rheo-MRI and an introduction of temperature control in the microcapillary rheo-MRI

platform. The former can be achieved by utilizing glues able to withstand temperatures $> 45\text{ }^{\circ}\text{C}$ for the construction of the 3D printed CC. For the latter, the current setup of the platform, with the connecting tubing housed within the body of the probe precludes the regular sample temperature control used in NMR. A readily available solution is to regulate the temperature of the sample in the reservoir. To avoid heat loss, the distance between the reservoir and the microcapillary must be kept minimal, and a layer of isolation around the connecting tubing can be introduced. If more precise temperature control is required, a water jacket running along the whole length of the tubing could be considered, at the cost of simplicity of the experimental setup.

6.3. Strongly confined flow of complex fluids

6.3.1. Factors governing flow cooperativity

The past two decades have seen many experimental and theoretical efforts in the field of strongly confined flow of complex fluids, which has undoubtedly helped to advance the understanding of cooperativity.^{4,6,12-16} However, the extent or the presence of these effects cannot yet be fully predicted, as we lack sufficient understanding of what the determining factors are. In this section, ξ values reported in the literature are collated with those quantified during this thesis project, in a search of general trends, to aid predictions of presence and extent of cooperativity.

In Table 6.2, ξ values reported in the literature on flow cooperativity are summarized, together with values quantified for FCDs in this thesis work. Additionally, chosen sample properties and experimental conditions are listed, along with classification of whether a variation in the chosen parameter influenced the values of ξ . Firstly, it can be noticed that cooperativity effects in flow of emulsions, microgels, mustard seeds, polystyrene bead suspensions and foams were found to be independent of the flow driving conditions and properties of the confining geometry. The extent of cooperativity and the resulting ξ values were influenced only by changing the sample properties, such as concentration or d . The opposite was found for milk gels, cellulose dispersions and FCDs, where the extent of cooperativity was dependent on shear rate, $\dot{\gamma}$, or the pressure drop, ΔP , but not always on sample properties. Notably, the emerging classification of fluids in terms of ξ -determining factors reflects their flow behavior as non-thixotropic or thixotropic YSFs, respectively.

Table 6.2: Comparison of ξ values reported for different particulate fluids in the literature or quantified throughout this thesis work. Chosen experimental conditions are listed, including the volume fraction, ϕ , the wt% concentration, C , d , polydispersity, w , and the influence of the experimental parameters on ξ .

Cooperative fluid	ϕ [%]	C [wt%]	d [μm]	Polydisp. [%]	w [μm]	ξ [μm]	ξ found independent of:	ξ found dependent on:
Silicone oil-in-water emulsions ^{4,13,17}	70 – 85	-	3.2 – 6.5	38 – 20	85 – 250	4 – 30	Surface roughness, w , ΔP	Oil vol. fraction, polydispersity, d
	80	-	5	21	30 – 50	4.5	$\dot{\gamma}$, w	-
	75	-	3	-	750	61.2	$\dot{\gamma}$	-
Microgels ^{4,18}	-	0.25 – 1	3.4 – 2.4	11.8 – 4.2	116	7.3 – 11.7	ΔP	C
	-	1.6	0.22	-	750	147	Surface interaction, $\dot{\gamma}$	-
Mustard seeds ¹⁹	-	-	1.2×10^3	-	2×10^4	4×10^3	$\dot{\gamma}$	-
Polystyrene bead suspension ¹⁹	0.59	-	40	-	1×10^4	5.2×10^3	$\dot{\gamma}$	Particle migration

Foams ²⁰					20%					$\dot{\gamma}$	-
Milk gels ²¹	-	12			-	~15	800	8.5 x 10 ⁴	6.6 x 10 ³	-	$\dot{\gamma}$
Cellulose dispersions ^{8,22}	-	0.3			-	~40	800	800	56 - 149		
FCDs ²³	-	27			43	30	500	500	54 - 308	<i>C</i>	$\dot{\gamma}$, crystallization rate
						50			81 - 164		
						220			0		
						20	250	250	25 - 52		
		15			40		540				

The plot in Fig. 6.2 of ξ/d vs. d/w aids in visualizing the second observation, namely that in most studied materials cooperative domains span clusters of $\sim 1 - 15$ particles. It thus follows that the number of particles involved in cooperative plastic rearrangements seems to be independent of the materials' microstructural properties. Exceptions were found in a microgel and the polystyrene bead suspension where cooperative clusters as large as 700 particles were quantified (red box in Fig. 6.2).⁴

From Fig. 6.2 it can also be seen that in most studies cooperativity effects were quantified under conditions of $d/w > 0.01$, in good agreement with the established threshold value between confined and non-confined flow.¹² However, it is not known how the extent of cooperativity changes as the d/w parameter is varied. During this thesis work, flow was studied under varying flow confinement degree in two ways. In **Chapter 3**, cooperativity effects were studied under fixed w , but variable d as a result of varying the crystallization rate and temperature. The obtained d/w was ranging between 0.06 and 0.44. In **Chapter 4**, the implementation of the microcapillary rheo-MRI platform enabled regulating the d/w in the range 0.04 –

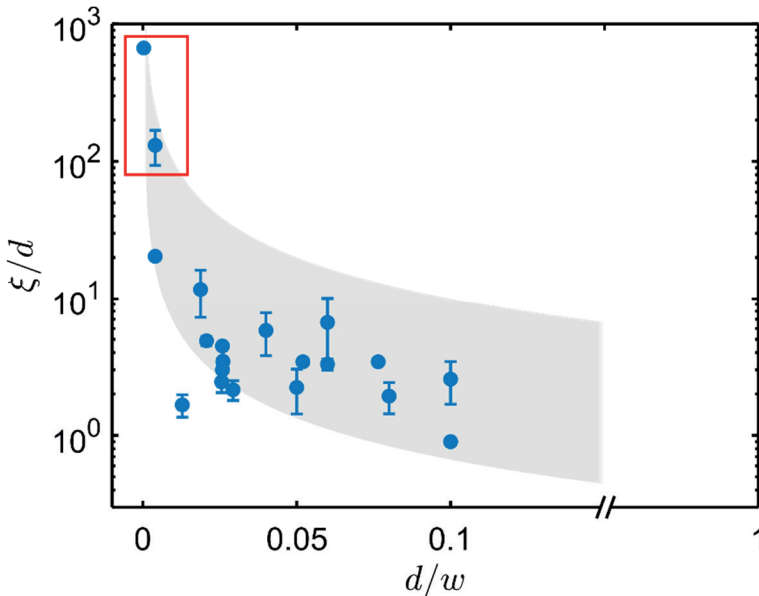


Figure 6.2: Dependence of ξ/d on d/w based on the studies reviewed in Table 6.2. Error bars originate from respective identified variations in ξ , caused by parameters listed in the last column of Table 6.2. The shaded band spans values between $1/d$ and $1/15d$. Red box indicates exceptionally high values of ξ in a microgel and the polystyrene bead suspension.⁴

0.08 by changing w , while keeping the parameter d fixed. The presence of flow cooperativity was detected in almost all experiments, confirming the fact that strong confinement is indeed one of the triggering factors. Additionally, in **Chapter 3**, a decrease in the mean quantified ξ values was observed upon increasing the microstructure size. In agreement with this finding, in **Chapter 4**, increasing d/w by decreasing the size of the microcapillary caused a decrease in ξ values. These observations were made on FCDs, but the same trend was also observed in Carbopol microgels.²⁴

Finally, Fig. 6.2 illustrates that the highest d/w explored in most studies is ~ 0.1 , with the flow regime at high flow confinement degree remaining mainly unexplored. In **Chapter 3**, no cooperativity effects in 27 wt% FCDs could be quantified for the extreme confinement condition of $d/w = 0.44$. However, to generalize this observation, studies where d/w is systematically varied beyond the value of 0.1 are needed. Notably, however, it must be considered that as w approaches the value of d , the current understanding of flow in YSFs as a series of elastic and plastic rearrangements may be incorrect, as flow transitions towards shear of individual particles.

6.3.2. Perspectives in quantification of flow cooperativity

This section contains an outlook with regards to prediction and more accurate quantification of cooperativity effects in model and real-life complex fluids. Potential shortcomings in current modelling approaches are explored, namely an assumption of a constant ξ even in geometries with non-uniform stress fields, and an oversimplification of thixotropic properties in YSFs.

Predicting cooperativity lengths. Being able to predict the presence and extent of cooperativity effects would enable accounting for spatially-dependent viscosities and flow enhancement under a range of experimental or processing conditions. To aid this task, the analysis of ξ values reported for a range of fluids, as performed in the previous section, allows to outline a number of trends. Firstly, cooperativity effects should be expected if flow occurs at d/w within the $\sim 0.01 - 0.1$ range. Below this limit, ξ tends to infinity as the fluid transitions into flow obeying the global rheological laws. At $d/w > 0.1$, ξ tends to 0 as the mobility of particles under extreme confinement becomes reduced, as observed during this thesis project in concentrated FCDs. It is possible, however, that deformable particles, such as bubbles and droplets will respond differently to extreme flow confinement than non-

deformable fat crystal aggregates. It thus follows that generalizing such conclusion to a wider range of fluids, and pinpointing the exact value of the upper limit above which no cooperativity effects can be observed, requires further, more systematic studies of different materials in this flow regime. Secondly, regardless of the fluids' microstructure, ξ values ranging between d and $15 \cdot d$ should be expected. Finally, depending on the properties of the YSF, different experimental parameters can be used to alter the extent of cooperativity. For thixotropic fluids, ξ can be adapted by adjusting the flow driving conditions, while for simple YSFs changes in the samples' microstructure are required.

Quantification of cooperativity with constant or stress-dependent ξ . Theoretical models predict that ξ is a function of stress, diverging at the dynamical yield stress.^{6,25} In agreement with this, in **Chapter 4**, the stress distribution was found to influence the extent of cooperativity. Samples of 15 wt% FCDs flowing in a 540 μm gap microcapillary, with 100% stress variation, exhibited $\sim 35\%$ smaller ξ values than when flowing in a 500 μm gap CC, where stress varies across the gap by only 11%. This difference likely originates from the fact that in the microcapillaries, the quantified constant ξ value is an average parameter of the present range of $\xi(\sigma)$, with a distribution much broader than in the CC. It can thus be hypothesized that the accuracy of modelling the confined flow should be directly improved by adopting a definition of $\xi(\sigma)$, particularly for geometries with a wide stress distribution. Importantly, such approach also introduces spatial dependence of ξ .

The hypothesis was explored in a preliminary study, where the velocity profiles of 0.5 wt% Carbopol and 15 wt% FCD flowing in microcapillaries were fitted with the fluidity model containing ξ either as a constant or a function of σ , as defined in Bocquet *et al.*⁶ The obtained ξ values are reported in Fig. 6.3, together with plots of the residuals, calculated from the fitted velocity profiles. As expected, based on a 100% stress variation within the microcapillary, the predictions of ξ from both models are significantly different. From the adopted definition of $\xi(\sigma)$, the stress-dependent model predicts a divergence of ξ on approaching the value of σ_y of the fluid. The radial coordinate of the highest ξ values will thus depend on the relationship between σ_y and ΔP . At large ΔP values, the resulting $\sigma(x)$ within the capillary typically falls above the σ_y threshold yielding the highest ξ values in the central parts of the capillary, as is the case for 0.5 wt% Carbopol (Fig. 6.3a). If $\sigma(x)$ falls within a close proximity to σ_y , highest ξ values are found closer to the walls (Fig. 6.3b). In contrast, the stress-independent model yields ξ values independent of the axial

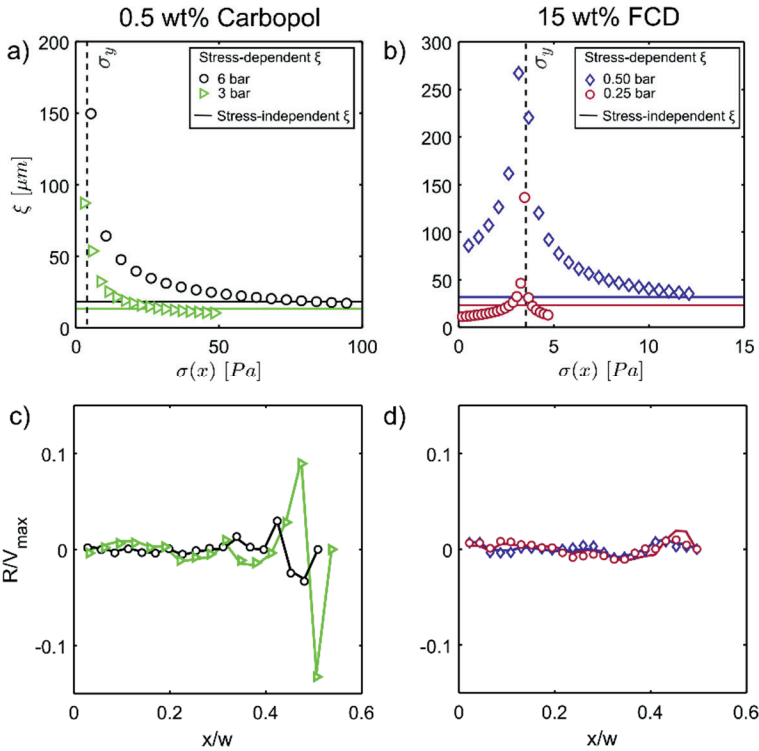


Figure 6.3: Comparison of ξ values obtained by fitting local velocimetry data with stress-dependent (symbols) and independent (solid lines) ξ definitions, for 0.5 wt% Carbopol (a) and 15 wt% FCD (b) flowing in capillaries with respective diameters of 100 μm and 250 μm . Plots in c and d report residuals obtained from fitting of both models to the data.

position. Curiously, however, the results from both models are in good agreement at the walls of the capillary, regardless of the sample, or the values of σ_y and ΔP . Furthermore, as can be seen from the residuals normalized by the respective maximum velocities, V_{max} , both models fit the velocity profiles equally well. According to this result, the accuracy of modelling of the velocity profiles is independent of the choice of constant or stress-dependent ξ . If, however, the aim of a study is to characterize the cooperativity lengths within the fluid flowing in a geometry with stress inhomogeneity, a model with $\xi(\sigma)$ should be used.

Flow cooperativity and thixotropy. The current approach to quantify cooperativity effects is based on the evaluation of cooperative flow relative to the bulk, non-confined flow behavior. As a consequence, the accuracy of the quantified ξ values relies on the correct knowledge of bulk flow properties. However, the determination

of the latter is often challenging even for simple YSFs.²⁶ Hence, flow of many real-life, thixotropic YSFs is commonly approximated with a HB model. The advantage of such approach is that the model is easily incorporated into the framework of the fluidity model. However, a complete omission of thixotropic properties may result in inaccurate or even incorrect ξ values. An inclusion of a thixotropic model as a definition of the bulk fluidity, f_{bulk} , was pioneered by Serial *et al.*,^{21,22} where the authors could conjointly account for cooperativity effects and the sample's thixotropic properties. The geometry used in that study was a commercially available CP with $\theta = 7^\circ$ with a uniform stress across the flow gap. This latter property is, however, not representative of many real-life situations where the sample flows through geometries with a wide stress distribution. Hence, the next important step in modelling of cooperativity effects should be to account for flow cooperativity, thixotropy and stress distribution within the geometry.

As a preliminary exploration of this idea, flow cooperativity was quantified in two 27 wt% FCDs, flowing in a 500 μm gap CC, incorporating the definition of f_{bulk} according to the HB or the λ -model. As introduced in **Chapter 1**, the latter is one of the simplest models to capture the time-dependent flow behavior of a thixotropic sample. As can be seen from the global flow curves of both dispersions, crystallized at two different cooling rates, the hysteresis between the down- and up-sweep branches testifies to the presence of thixotropy (Figs. 6.4a and 6.4d). The bulk flow properties can be thus described by fitting the downsweep branch with the λ -model which gives the information about the critical shear rate, $\dot{\gamma}_c$, and the corresponding critical stress, σ_c , below which the sample does not flow uniformly. On the other hand, the bulk flow can be approximated with a simple HB model which gives the value of σ_y . Subsequently, the local flow behavior can be predicted, according to the chosen global flow model, as done in Figs. 6.4b and 6.4e for $\dot{\gamma}_{app} = 10 \text{ s}^{-1}$. As can be seen, at 10 s^{-1} the experimentally measured velocities significantly exceed those predicted by both models, which was also the case for all other tested $\dot{\gamma}_{app}$ values. Fitting the experimental velocity profiles with the fluidity model and both definitions of f_{bulk} results in ξ values as plotted in Figs. 6.4c and 6.4f. According to the definitions of σ_y and σ_c , for stresses below these values no flow should occur, regardless of the assumed global flow model. It thus follows that the observed flow is entirely dictated by cooperative rearrangements, resulting in identical ξ values obtained in both approaches. In conditions where the present stresses exceed the σ_y , but not σ_c , the results of both models start to deviate from each other. In summary, for flows occurring in conditions in close proximity to critical, or threshold values, such as in

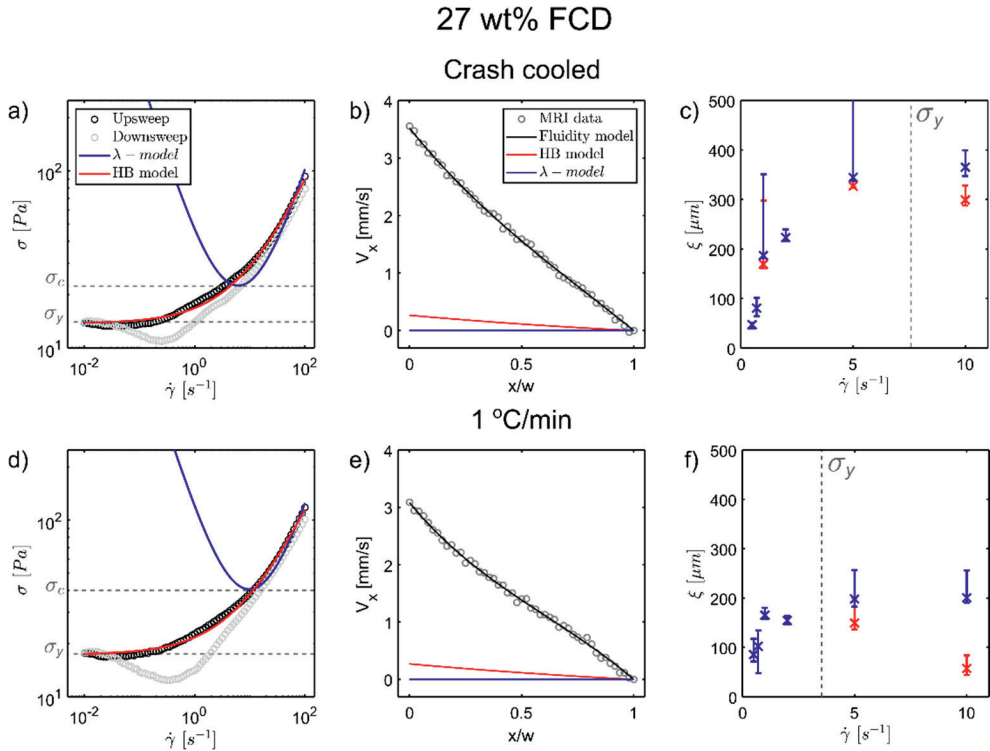


Figure 6.4: Global flow curves (a and d) of 27 wt% FCDs crystallized by crash cooling (top) or at 1 °C/min (bottom), acquired by sweeping $\dot{\gamma}$ from high to low values, followed by sweep from low to high values. The downsweep branch is fitted with a λ -model (blue) and a HB model (red). In c and f, a comparison of ξ values for respective FCDs is shown, obtained by fitting a fluidity model to spatially-resolved velocity profiles (b and e) with the definition of f_{bulk} obtained from the λ - or a HB model of the global flow data.

the vicinity of σ_y , the accuracy of the obtained ξ is dictated by the uncertainty with which the bulk flow of the sample can be described. For such cases, it is thus very important to account for the time dependence of flow.

6.4. What's next?

6.4.1. Potential future research into flow cooperativity

Given the versatility of the developed MRI velocimetry setups, a plethora of factors potentially influencing flow cooperativity can be explored in a wide range of fluids. Firstly, it would be of interest, from the fundamental standpoint and for industrial applications, to investigate the influence of temperature on cooperativity effects in

both Brownian and non-Brownian fluids. In the latter, variations in temperature will probably not influence the propagation of stress, and thus cooperativity, directly, but might indirectly influence microstructural changes. Secondly, it would be relevant to study the effects of molecular-level interactions on cooperativity. Examples of interesting questions to answer here include: How does cooperativity depend on the viscosity of the continuous medium? Is flow cooperativity dependent on friction between the particles, and if so, can it be tuned by modifying, *e.g.*, surfactants in emulsions or fractality and polymorphic forms in FCDs? Finally, another relevant direction to pursue would be an investigation of cooperativity effects in suspensions of anisotropic particles, where potentially ξ could assume a tensorial form, and be dependent on a possible flow-induced alignment.

6.4.2. Towards probing flow-induced alignment

Cooperativity of plastic rearrangements is only one of the many effects that can dictate the flow of soft structured materials in strong confinements. Another important phenomenon is flow-induced alignment, which can occur in dispersions of anisotropic particles. The latter include fat dispersions with sheet-like crystalline nanoplatelets, or elongated structures present in liquid crystals and wormlike micelles. In such fluids, the non-aligned and aligned phases will have different flow properties and, thus, must be adequately characterized for accurate flow modelling.²⁷⁻³¹ Flow-induced alignment can be probed by measuring molecular self-diffusion, a method widely used for determining microstructural features in soft, structured materials and other complex matrices.^{32,33} With MRI, self-diffusion coefficients, D , can be measured in a spatially-resolved fashion using a single or double PFG-SE.³⁴⁻³⁶ Importantly, the double PFG-SE enables quantification of solely the stochastic motion of molecules, even in the presence of deterministic motion during flow. By measuring D in two directions, namely parallel and perpendicular to main flow direction, it is possible to establish the preferential diffusion direction, and to gain insight into the presence of local alignment, as schematically shown in Fig. 6.5.

However, flow in strong confinement exhibits phenomena that can significantly challenge the correct determination of diffusion coefficients. Firstly, in microcapillaries flow cannot always be described as purely laminar, despite typically satisfying the condition of Reynolds number values, $Re \ll 2000$. The presence of a percolation network or transient local concentration gradients will induce small velocity fluctuations in the axial direction, as schematically shown in Figs. 6.6a and

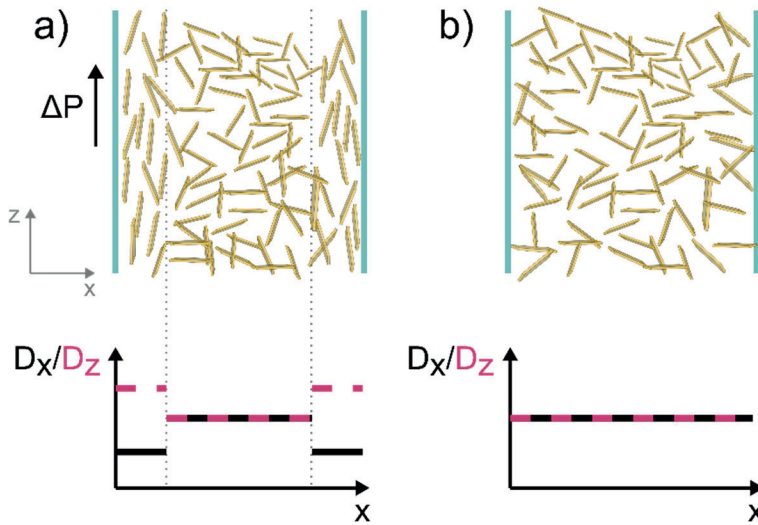


Figure 6.5: a) Top: dispersion with anisotropic particles flowing along z under a pressure drop, ΔP . Bottom: the effect that flow-induced alignment of anisotropic particles has on the diffusion coefficients along and perpendicular to flow direction, D_z and D_x , respectively. Dotted vertical lines mark the alignment regions in high stress areas of the microcapillary. In b) under static conditions no alignment exists (top) and diffusion is isotropic, i.e. $D_x = D_z$ (bottom).

6.6b, respectively.^{15,37,38} Secondly, under microcapillary flow the diffusing molecules sample streamlines of different velocities resulting in enhanced effective self-diffusion, D_{eff} , an effect known as Taylor dispersion (Fig. 6.6c).³⁹⁻⁴¹ The result of all three described phenomena is that the measured D_{eff} values exceed the true D values even by several orders of magnitude, masking the sought-after effect of alignment on diffusion. Such result was in fact observed during this thesis work in a preliminary study of expected alignment of thin crystalline nanoplatelets in MFC dispersions flowing in a 250 μm capillary. The obtained values of D_{eff} perpendicular to the main flow direction exceeded those of a static sample up to 9-fold at the walls and 3-fold in the center of the capillary. The effect likely originated from a combination of the presence of a weak-link network inducing axial flow and Taylor dispersion in the axial direction.⁴²

This evidences that validating a methodology to extract microstructural information from MRI diffusion measurements under flow constitutes a challenging task. In this respect, small- or wide-angle X-ray diffraction or scattering techniques,^{5,43} combined with the microcapillary flow setup may provide a more straightforward approach to retrieve information on flow-induced alignment.

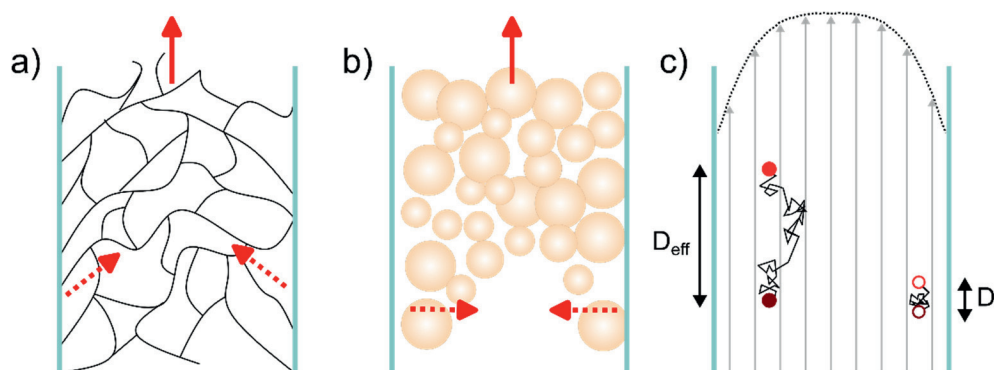


Figure 6.6: Schematic representation of the effect that a percolation network (a) and particle concentration gradient (b) can have on the flow in a microcapillary, with the solid arrows representing the principal flow direction and the dotted arrows representing the secondary, fluctuating velocity component in the axial direction. In c) an effect of Taylor dispersion on diffusion is schematically represented, with the dark and bright red circles representing the initial and final positions, respectively.

6.4.3. Beyond flow cooperativity

The two flow-MRI platforms developed throughout this thesis work were primarily aimed at studying flow cooperativity, but the key technical achievements open possibilities to a wide range of confined flow studies. For instance, the temperature-control circuit within the sub-mm gap CC enables studies of flow as a function of microstructure-forming processes important in food industry, including crystallization, melting, or gelation under shear. The scalable gap size and modifiable wall properties of the microcapillaries allow for studies of entrance and exit effects during food or organ 3D printing or polymer and fiber extrusion.^{1,44,45} The acquired flow-MRI information can be complemented by the aforementioned coupling of the microcapillary setup to scattering methods, such as SAXS and SANS, to obtain direct insight into the microstructural underpinning of the flow behavior.^{5,46} Both methods, however, have pre-requisites with regards to the properties of the microcapillaries. Whereas glass capillaries can be used in SAXS,²⁷ for SANS it is necessary to fabricate them from quartz.⁴⁷

Furthermore, the microcapillary rheo-MRI technique can be exploited in a much broader context, including in medical research and applications, such as engineering of biocompatible and biomimetic materials,⁴⁸ or vascular *in-vitro* models⁴⁹, as well as in the production and studies of smart materials, such as bi-component fibres⁵⁰, or aramids.⁵¹

Finally, the sensitivity of the microcapillary rheo-MRI measurements can be boosted by the combination of the flow-MRI platform with ultra-high field NMR spectrometers, and/or with the use of cryoprobes, enabling reaching even higher temporal resolutions in velocimetry measurements and accessing spectroscopic measurements with high chemical resolution.

References

- (1) Sun, J.; Zhou, W.; Huang, D. In *Reference Module in Food Science*, Smithers, G. W.; Elsevier, 2018, pp 1-9.
- (2) Macosko, C. W. *Rheology: Principles, Measurements and Applications*, 1st ed.; John Wiley & Sons, 1994.
- (3) Laryea, E.; Schuhardt, N.; Guthausen, G.; Oerther, T.; Kind, M. Construction of a temperature controlled rheo-NMR measuring cell – Influence of fluid dynamics on PMMA-polymerization kinetics, *Microporous Mesoporous Mater.* **2018**, *269*, 65-70.
- (4) Seth, J. R.; Locatelli-Champagne, C.; Monti, F.; Bonnacaze, R. T.; Cloitre, M. How do soft particle glasses yield and flow near solid surfaces?, *Soft Matter* **2012**, *8* (1), 140-148.
- (5) Velichko, E.; Tian, B.; Nikolaeva, T.; Koning, J.; van Duynhoven, J. P. M.; Bouwman, W. G. A versatile shear cell for investigation of structure of food materials under shear, *Colloids Surf. A: Physicochem. Eng.* **2019**, *566*, 21-28.
- (6) Bocquet, L.; Colin, A.; Ajdari, A. Kinetic Theory of Plastic Flow in Soft Glassy Materials, *Phys. Rev. Lett.* **2009**, *103* (3), 036001.
- (7) Gladden, L. F.; Sederman, A. J. Recent advances in Flow MRI, *J. Mag. Reson.* **2013**, *229*, 2-11.
- (8) de Kort, D. W.; Veen, S. J.; Van As, H.; Bonn, D.; Velikov, K. P.; van Duynhoven, J. P. M. Yielding and flow of cellulose microfibril dispersions in the presence of a charged polymer, *Soft Matter* **2016**, *12* (21), 4739-4744.
- (9) Nikolaeva, T.; den Adel, R.; Velichko, E.; Bouwman, W. G.; Hermida-Merino, D.; Van As, H.; Voda, A.; van Duynhoven, J. P. M. Networks of micronized fat crystals grown under static conditions, *Food Funct.* **2018**, *9* (4), 2102-2111.
- (10) Tijssen, K. C. H.; Bart, J.; Tiggelaar, R. M.; Janssen, J. W. G.; Kentgens, A. P. M.; van Bentum, P. J. M. Spatially resolved spectroscopy using tapered stripline NMR, *J. Mag. Reson.* **2016**, *263*, 136-146.
- (11) Tijssen, K. C. H.; van Weerdenburg, B. J. A.; Zhang, H.; Janssen, J. W. G.; Feiters, M. C.; van Bentum, P. J. M.; Kentgens, A. P. M. Monitoring Heterogeneously Catalyzed Hydrogenation Reactions at Elevated Pressures Using In-Line Flow NMR, *Anal. Chem.* **2019**, *91* (20), 12636-12643.
- (12) Goyon, J.; Colin, A.; Ovarlez, G.; Ajdari, A.; Bocquet, L. Spatial cooperativity in soft glassy flows, *Nature* **2008**, *454*, 84-87.
- (13) Goyon, J.; Colin, A.; Bocquet, L. How does a soft glassy material flow: finite size effects, non local rheology, and flow cooperativity, *Soft Matter* **2010**, *6* (12), 2668-2678.
- (14) Nicolas, A.; Barrat, J.-L. Spatial Cooperativity in Microchannel Flows of Soft Jammed Materials: A Mesoscopic Approach, *Phys. Rev. Lett.* **2013**, *110* (13), 138304.
- (15) van de Laar, T.; Schroën, K.; Sprakel, J. Cooperativity and segregation in confined flows of soft binary glasses, *Phys. Rev. E* **2015**, *92* (2), 022308.
- (16) Derzi, L.; Filippi, D.; Mistura, G.; Pierno, M.; Lulli, M.; Sbragaglia, M.; Bernaschi, M.; Garstecki, P. Fluidization and wall slip of soft glassy materials by controlled surface roughness, *Phys. Rev. E* **2017**, *95* (5), 052602.
- (17) Paredes, J.; Shahidzadeh, N.; Bonn, D. Wall slip and fluidity in emulsion flow, *Phys. Rev. E* **2015**, *92* (4), 042313.
- (18) Geraud, B.; Bocquet, L.; Barentin, C. Confined flows of a polymer microgel, *Eur. Phys. J. E* **2013**, *36* (3), 1-13.

- (19) de Cagny, H.; Fall, A.; Denn, M. M.; Bonn, D. Local rheology of suspensions and dry granular materials, *J. Rheol.* **2015**, *59* (4), 957-969.
- (20) Katgert, G.; Tighe, B. P.; Möbius, M. E.; van Hecke, M. Couette flow of two-dimensional foams, *Europhys. Lett.* **2010**, *90* (5), 54002.
- (21) Serial, M. R.; Bonn, D.; Huppertz, T.; Dijkstra, J. A.; van der Gucht, J.; van Duynhoven, J. P. M.; Terenzi, C. Nonlocal effects in the shear banding of a thixotropic yield stress fluid, *Phys. Rev. Fluids* **2021**, *6* (11), 113301.
- (22) Serial, M. R.; Velichko, E.; Nikolaeva, T.; den Adel, R.; Terenzi, C.; Bouwman, W. G.; van Duynhoven, J. P. M. High-pressure homogenized citrus fiber cellulose dispersions: Structural characterization and flow behavior, *Food Struct.* **2021**, *30*, 100237.
- (23) Milc, K. W.; Dijkstra, J. A.; van Duynhoven, J. P. M.; Terenzi, C. Quantifying cooperative flow of fat crystal dispersions, *Soft Matter* **2022**, *18* (14), 2782-2789.
- (24) Géraud, B.; Jørgensen, L.; Ybert, C.; Delanoë-Ayari, H.; Barentin, C. Structural and cooperative length scales in polymer gels, *Eur. Phys. J. E* **2017**, *40* (5), 1-10.
- (25) Kamrin, K.; Koval, G. Nonlocal Constitutive Relation for Steady Granular Flow, *Phys. Rev. Lett.* **2012**, *108* (17), 178301.
- (26) Bonn, D.; Denn, M. M.; Berthier, L.; Divoux, T.; Manneville, S. Yield stress materials in soft condensed matter, *Rev. Mod. Phys.* **2017**, *89* (3), 035005.
- (27) Vilotte, A.; Bodiguel, H.; Ako, K.; Gunes, D. Z.; Schmitt, C.; de Loubens, C. Kinetic and structural characterization of whey protein aggregation in a millifluidic continuous process, *Food Hydrocoll.* **2021**, *110*, 106137.
- (28) Tian, B.; Wang, Z.; de Campo, L.; Gilbert, E. P.; Dalgliesh, R. M.; Velichko, E.; van der Goot, A. J.; Bouwman, W. G. Small angle neutron scattering quantifies the hierarchical structure in fibrous calcium caseinate, *Food Hydrocoll.* **2020**, *106*, 105912.
- (29) Angelico, R.; Gentile, L.; Ranieri, G. A.; Oliviero Rossi, C. Flow-induced structures observed in a viscoelastic reverse wormlike micellar system by magnetic resonance imaging and NMR velocimetry, *RSC Adv.* **2016**, *6* (40), 33339-33347.
- (30) Masselon, C.; Colin, A.; Olmsted, P. D. Influence of boundary conditions and confinement on nonlocal effects in flows of wormlike micellar systems, *Phys. Rev. E* **2010**, *81* (2), 021502.
- (31) Trebbin, M.; Steinhauser, D.; Perlich, J.; Buffet, A.; Roth, S. V.; Zimmermann, W.; Thiele, J.; Förster, S. Anisotropic particles align perpendicular to the flow direction in narrow microchannels, *Proc. Natl. Acad. Sci. U.S.A.* **2013**, *110* (17), 6706-6711.
- (32) Karlsons, K.; de Kort, D. W.; Sederman, A. J.; Mantle, M. D.; Freeman, J. J.; Appel, M.; Gladden, L. F. Characterizing pore-scale structure-flow correlations in sedimentary rocks using magnetic resonance imaging, *Phys. Rev. E* **2021**, *103* (2), 023104.
- (33) Hoehn-Berlage, M.; Eis, M.; Schmitz, B. Regional and directional anisotropy of apparent diffusion coefficient in rat brain, *NMR Biomed.* **1999**, *12* (1), 45-50.
- (34) Callaghan, P. T. Rheo-NMR: nuclear magnetic resonance and the rheology of complex fluids, *Rep. Prog. Phys.* **1999**, *62* (4), 599-670.
- (35) Lutti, A.; Callaghan, P. T. Measurement of diffusion in the presence of shear flow, *J. Mag. Reson.* **2006**, *180* (1), 83-92.
- (36) Stejskal, E. O. Use of Spin Echoes in a Pulsed Magnetic-Field Gradient to Study Anisotropic, Restricted Diffusion and Flow, *J. Chem. Phys.* **1965**, *43* (10), 3597-3603.
- (37) Schroën, K.; van Dinther, A.; Stockmann, R. Particle migration in laminar shear fields: A new basis for large scale separation technology?, *Sep. Purif. Technol.* **2017**, *174*, 372-388.
- (38) van Dinther, A. M. C.; Schroën, C. G. P. H.; Imhof, A.; Vollebregt, H. M.; Boom, R. M. Flow-induced particle migration in microchannels for improved microfiltration processes, *Microfluid. Nanofluidics* **2013**, *15* (4), 451-465.
- (39) Taylor, G. I. Dispersion of soluble matter in solvent flowing slowly through a tube, *Proc. R. Soc. London, Ser. A* **1997**, *219* (1137), 186-203.

- (40) Codd, S. L.; Manz, B.; Seymour, J. D.; Callaghan, P. T. Taylor dispersion and molecular displacements in Poiseuille flow, *Phys. Rev. E* **1999**, *60* (4), R3491-R3494.
- (41) Seymour, J. D.; Codd, S. L.; Kimmich, R. Peclet number dependent superdiffusive hydrodynamic dispersion in a site percolation porous media measured by NMR, *Microporous Mesoporous Mater.* **2018**, *269*, 56-59.
- (42) Callaghan, P. T.; Codd, S. L.; Seymour, J. D. Spatial coherence phenomena arising from translational spin motion in gradient spin echo experiments, *Concepts Magn. Reson.* **1999**, *11* (4), 181-202.
- (43) Nikolaeva, T.; den Adel, R.; van der Sman, R.; Martens, K. J. A.; Van As, H.; Voda, A.; van Duynhoven, J. P. M. Manipulation of Recrystallization and Network Formation of Oil-Dispersed Micronized Fat Crystals, *Langmuir* **2019**, *35* (6), 2221-2229.
- (44) Liu, Z.; Zhang, M.; Bhandari, B.; Wang, Y. 3D printing: Printing precision and application in food sector, *Trends Food Sci. Technol.* **2017**, *69*, 83-94.
- (45) Liu, F.; Wang, X. Synthetic Polymers for Organ 3D Printing, *Polymers* **2020**, *12* (8).
- (46) Pink, D. A.; Peyronel, F.; Quinn, B.; Singh, P.; Marangoni, A. G. Condensation versus diffusion. A spatial-scale-independent theory of aggregate structures in edible oils: applications to model systems and commercial shortenings studied via rheology and USAXS, *J. Phys. D: Appl. Phys.* **2015**, *48* (38), 384003.
- (47) Douth, J.; Gilbert, E. P. Characterisation of large scale structures in starch granules via small-angle neutron and X-ray scattering, *Carbohydr. Polym.* **2013**, *91* (1), 444-451.
- (48) Del Bakhshayesh, A. R.; Asadi, N.; Alihemmati, A.; Tayefi Nasrabadi, H.; Montaseri, A.; Davaran, S.; Saghati, S.; Akbarzadeh, A.; Abedelahi, A. An overview of advanced biocompatible and biomimetic materials for creation of replacement structures in the musculoskeletal systems: focusing on cartilage tissue engineering, *J. Biol. Eng.* **2019**, *13* (1), 85.
- (49) Cochrane, A.; Albers, H. J.; Passier, R.; Mummery, C. L.; van den Berg, A.; Orlova, V. V.; van der Meer, A. D. Advanced in vitro models of vascular biology: Human induced pluripotent stem cells and organ-on-chip technology, *Adv. Drug Deliv. Rev.* **2019**, *140*, 68-77.
- (50) Chien, A.-T.; Gulgunje, P. V.; Chae, H. G.; Joshi, A. S.; Moon, J.; Feng, B.; Peterson, G. P.; Kumar, S. Functional polymer-polymer/carbon nanotube bi-component fibers, *Polymer* **2013**, *54* (22), 6210-6217.
- (51) Fink, J. K. In *High Performance Polymers*, Fink, J. K.; William Andrew Publishing, 2014, pp 301-320.

CHAPTER

7

Summary

The understanding and ability to reliably predict the flow behavior of complex fluids can determine the efficiency of food production processes, success of novel techniques such as 3D printing and many more. However, flow of the involved soft structured particulate fluids is intrinsically prone to instabilities, rendering flow predictions challenging. This challenge is magnified if flow occurs under strongly-confined conditions, *i.e.*, when the flow gap size exceeds the average microstructure size by a factor of $\leq 10^2$. Under these conditions flow is governed by cooperativity effects, where plastic rearrangements of the particles are spatially correlated, leading to suppression of yield stress, enhanced velocities and inhomogeneous viscosities. For most industrially-relevant fluids, such as emulsions or fiber dispersions, with particle sizes in the range sub- μm to tens of μm , flow becomes cooperative in sub-mm confinements. Despite a profound effect of cooperativity on flow, these effects are not well understood, nor are the factors that determine their extent, making them impossible to account for in production processes and product design.

To study and understand flow cooperativity, velocimetric techniques are required with the following criteria: (i) ability to access spatially-resolved flow information, (ii) ability to provide local flow information with spatial resolution of $> 10\%$ of the flow gap size, and (iii) availability of flow geometries with gap sizes scalable within sub-mm range. The up-to-date available techniques which fulfill the criteria (i) – (iii), such as Particle Imaging Velocimetry, require optical transparency of the fluid, which precludes studies of most of industrially-relevant, optically-opaque fluids. Rheo-MRI velocimetry is a promising alternative which does not suffer from this limitation, and additionally offers the possibility of acquiring chemically-resolved information on the fluid. However, so far only flow geometries with mm-sized gaps have been available. Thus, it was the aim of this thesis to develop rheo-MRI velocimetry platforms with flow geometries scalable in the sub-mm range, and utilize them to study flow cooperativity of complex fluids.

To this aim, in **Chapter 2** a 500 μm gap CC for rotational rheo-MRI was developed. The CC was equipped with a water circuit for temperature control in the range 15 – 40 °C. One of the targeted improvements was the notorious off-axis wobble of the rotating bob, successfully achieving a mechanical stability within $\sim 7 \mu\text{m}$. This made it possible to acquire artefact-free 1D velocity profiles with spatial resolution of 10 $\mu\text{m}/\text{pixel}$, and measurements under uni-directional shear conditions. The developed CC enabled studies of strongly-confined local flow behavior of optically-opaque 27

wt% FCDs, a common food precursor in production of fat-based products. In this preliminary study, spatially-dependent viscosities were observed at low shear rates and room temperature, likely triggered by cooperativity effects. Velocimetry measurements at 30 °C revealed the presence of time-dependent shear-banding, absent at 15 °C and, thus, likely caused by recrystallization and aggregation of the dispersed crystalline platelets.

The strongly-confined flow of 27 wt% FCDs was further studied in **Chapter 3**, as a function of the microstructure size and the colloidal network properties, controlled by the crystallization rate. The flow of the 27 wt% FCD with the largest crystal aggregates of $\sim 200 \mu\text{m}$ was found to be independent of the gap size and was well described by the classical rheological HB model. The absence of cooperativity effects was ascribed to the limited inter-particle interactions, caused by extreme confinement. On the other hand, the 27 wt% FCDs with aggregate sizes in the range 30 – 50 μm were found to exhibit cooperativity-induced velocity enhancement and spatially-dependent viscosities. A proposed numerical approach based on the concept of fluidity provided cooperativity lengths, ξ , yielding values ranging between 50 and 300 μm , respectively corresponding to clusters of $\sim 1 - 11$ aggregates. Importantly, the study revealed a decreasing trend of mean ξ values with increasing degree of flow confinement.

Due to the challenging alignment of the centers of the bob and the cup within the CC, and relatively low SNR within the rotational rheo-MRI configuration, the minimum attainable gap size is limited to $\sim 500 \mu\text{m}$. Thus, in **Chapter 4**, a microcapillary rheo-MRI platform was developed with (i) gap size easily scalable down to $\sim 50 \mu\text{m}$ and (ii) modifiable wall properties. These features can be explored for studies of cooperativity, respectively (i) in confinements $< 500 \mu\text{m}$ and in dispersions with particle sizes $< 10 \mu\text{m}$, and (ii) under tunable particle-wall interactions. With the microcapillary rheo-MRI platform 2D velocity maps can be acquired, with spatial and temporal resolution of 5 $\mu\text{m}/\text{pixel}$ and $\sim 5 \text{ min}/\text{scan}$, respectively. The developed platform was exploited in studies of flow cooperativity in 0.5 wt% Carbopol, with small particle size of $\sim 2 \mu\text{m}$, and in 15 wt% FCDs as a function of the flow confinement degree. 0.5 wt% Carbopol was found to exhibit pressure independent cooperativity effects spanning on average ~ 6 polymer blobs in a 100 μm confinement. In 15 wt% FCDs cooperative clusters were found to extend over 1 – 10 aggregates, with the ξ values dependent on the applied pressure and degree of flow confinement.

In the industrial setting, the FCDs studied in **Chapters 2 – 4** are typically produced by melt-cool routes to obtain the desired microstructure. This approach has, however, proved hard to control due to concomitant crystallization and aggregation of the crystalline nanoplatelets. MFC dispersions are a novel and more reproducible alternative to FCDs in the production of fat-based foods, where the two structure forming stages are decoupled. However, their flow properties and the associated multi length scale structural changes are not yet well understood. Thus, in **Chapter 5** the relationship between the microstructure and the flow properties of 15 wt% MFC dispersions was studied. Using hyperspectral Raman imaging and SAXD the shear-induced aggregation and recrystallization was demonstrated. These microstructural changes were then found to be at the basis of the strongly confined local flow behavior, as measured with the microcapillary rheo-MRI platform. The velocimetry measurements revealed the evolution of the fundamental rheological flow properties ranging from strongly non-HB towards simple-HB flow behavior, via a thixotropic intermediate as a result of the shear-induced disappearance of the weak-link network. The 15 wt% MFC dispersions exhibited no cooperativity effects in the tested 250 μm confinement, ascribed to the non-fractal nature and small particle sizes of $\sim 3 \mu\text{m}$.

Chapter 6 contains the general discussion of (i) the technical developments and (ii) the flow cooperativity effects studied and quantified throughout the thesis work. In (i) the developed flow-MRI platforms were compared with respect to their experimental capabilities and suitability to studies of fluids with high viscosity and thixotropic properties (section 6.2). In (ii) the ξ values quantified in the flow of FCDs during this thesis work were compiled with values found in other fluids, as reported in the literature (section 6.3). This overview comparison showed that typically for simple HB fluids, cooperativity effects depend on the microstructural properties of the sample while for thixotropic HB fluids the extent of cooperativity depends on the experimental conditions, such as applied pressure, shear or geometry. Both sections are concluded with perspectives for further technical improvements and more accurate quantification of flow cooperativity, respectively. Finally, an outlook towards further cooperativity studies is proposed, and other potential applications of the developed flow-MRI platforms are described.

Podsumowanie

Głównym tematem mojej pracy doktorskiej było badanie przepływu płynów nienewtonowskich przez złożone geometrie takie jak rury, rurki lub dysze. Kiedy myślimy o płynach często przychodzą nam na myśl płyny z życia codziennego, takie jak woda, miód lub alkohol. Są to tak zwane płyny proste/Newtonowskie, których zachowanie podczas płynięcia jest już dobrze zrozumiane i dosyć łatwe do przewidzenia. Płynami są również substancje takie jak krem, majonez lub jogurt. Są to płyny złożone/nienewtonowskie, których przepływ jest dużo trudniejszy do zrozumienia i przewidzenia. Ta cecha znacznie komplikuje procesy obecne przy produkcji kosmetyków lub żywności, takie jak na przykład wyciskanie produktów do opakowań. Przepływ płynów złożonych jest również spotykany w nowatorskich technologiach, takich jak drukowanie spożywcze lub biodruk 3D. W tym wypadku, wiedza o zachowaniu płynu używanego do druku umożliwia użycie odpowiedniego ciśnienia i temperatury, co jest niezbędne do uzyskania stabilnego produktu końcowego.

Ale co właściwie jest powodem tego, że przewidzenie w jaki sposób płyny złożone zachowują się podczas płynięcia jest tak skomplikowane? Jest za to odpowiedzialna mikrostruktura, którą płyny złożone często posiadają. Z jednej strony, mikrostruktura odpowiada za znane nam, makroskopowe, zachowanie się substancji. Przykładowo, w majonezie, mikrostruktura uformowana jest przez skoncentrowane kropelki oleju zawieszane w wodzie. Oddziaływania pomiędzy kroplami zapewniają, że kleks majonezu nie rozlewa się na boki, ale zachowuje nadany kształt. Jednak z drugiej strony, obecność mikrostruktury powoduje niestabilność podczas płynięcia. Na przykład, pomimo równomiernie przyłożonego ciśnienia, płyn w różnych częściach rury będzie miał różną lepkość, co, jeśli nie zostanie wzięte pod uwagę, może prowadzić do zablokowania przepływu.

Mój projekt skupiony był głównie na studiowaniu przepływu płynów złożonych przez otwory o przekrojach poniżej jednego milimetra, tak zwanego przepływu ograniczonego. Takie warunki odzwierciedlają te obecne przykładowo w druku 3D lub przy powlekanii obiektów warstwami farby ochronnej. Podczas przepływu ograniczonego zachowanie elementów mikrostruktury, przykładowo wspomnianych kropelek, jest względnie nietypowe w porównaniu do przepływu nieograniczonego. Normalnie, kiedy wprawiamy płyn w ruch, kropelki poruszają się względem siebie i otoczenia. W przepływie ograniczonym, poruszanie się kropelek w jednym miejscu, np.

przy ściankach rury, powoduje ruch kropeł w innym miejscu, np. w jej części środkowej (rysunek 1.2). Taki przepływ nazywamy kooperacyjnym, przez to że ruch elementów mikrostruktury w jednym miejscu powoduje ruch, a zatem płynie płynu w innym miejscu. Przepływ kooperacyjny został odkryty niedawno, i jest nadal mało zrozumiany, pomimo że w praktyce powoduje, że płyny stają się mniej lepkie: płyną dużo szybciej niż się przewiduje i w niejednorodny sposób.

Do tej pory badania nad przepływem kooperacyjnym były możliwe tylko w układach doświadczalnych z użyciem mikroskopu. Takie podejście jednak wymaga, żeby badane płyny były przezroczyste, a jak wiemy z podanych wyżej przykładów, większość płynów złożonych, spotykanych w życiu codziennym, nie jest. Rezonans Magnetyczny (RM), technika najbardziej znana w zastosowaniu medycznym, umożliwia zobrazowanie przepływu płynów bez względu na to, czy są one przezroczyste, czy nie, więc stanowi znakomite narzędzie do badania przepływu kooperacyjnego. Jest jednak jeden techniczny problem. Obecnie, używając RM, nie ma możliwości badania przepływu w otworach o przekroju mniejszym niż 1 mm, co jest warunkiem niezbędnym do zaobserwowania zjawiska kooperacji. Tak więc, celami mojego projektu było (1) stworzenie układu doświadczalnego, który umożliwi badanie przepływu płynów za pomocą RM w otworach poniżej 1 mm oraz (2) użycie rozwiniętych układów doświadczalnych do badania przepływu kooperacyjnego w różnych substancjach.

Oba te cele zostały osiągnięte, a wyniki są przedstawione w rozdziałach 2 – 5, co schematycznie obrazuje rysunek 1.7. Rozdziały 2 i 4 przedstawiają dwa techniczne rozwiązania do badania przepływu ograniczonego przy pomocy RM (cel 1). W rozdziale 2, rozwinęliśmy tak zwaną komorę Couette (rysunek 2.1), gdzie przepływ płynu może być badany w otworze o rozmiarze 0.5 milimetra. Ponadto, komora ta daje możliwość kontroli temperatury badanego płynu w zakresie 15 – 45 °C. Komora może być użyta jako część istniejącego już układu doświadczalnego, reo-RM (rysunek 1.4). Teoretycznie, stanowi to osiągnięcie celu pierwszego, jednakże mankamentem takiego rozwiązania jest to, że otworu w komorze nie da się łatwo przystosować do danego eksperymentu. Tak więc, w rozdziale 4 rozwinęliśmy drugi układ doświadczalny: kapilarny RM (rysunek 4.1), gdzie badany płyn przepływa przez, jak sugeruje nazwa, kapilary. W porównaniu do komory Couette, takie rozwiązanie jest dużo bardziej elastyczne, ponieważ przekrój kapilar można łatwo dostosować do danego eksperymentu, a przepływ można badać nawet w bardzo małych otworach o przekroju rzędu 50 mikrometrów. Opracowane układy doświadczalne umożliwiły

badania nad sposobem płynięcia tzw. zawiesiny kryształów tłuszczu (ang: fat crystal dispersions, FCD, rysunek 3.1), co stanowiło drugi cel projektu. FCD używane są w przemyśle żywnościowym do produkcji np. masła roślinnego lub czekolady (rysunek 1.6b), więc zrozumienie jak zachowują się podczas płynięcia jest bardzo ważne przy wytwarzaniu tych produktów. W rozdziale 3, używając układu reo-RM odkryliśmy, że FCD wykazują cechy przepływu kooperacyjnego, którego wielkość zależy od wielkości grudek kryształków tłuszczu. W rozdziale 4 i 5, przy użyciu kapilarnego RM zbadaliśmy płynięcie FCD w jeszcze mniejszych otworach i zgodnie z tym, co zaobserwowaliśmy w rozdziale 3, wykazaliśmy obecność kooperacji. Ponadto, odkryliśmy, że w FCD efekty kooperacji maleją wraz z malejącym otworem przepływu.

Podsumowując, układy doświadczalne opracowane podczas mojego projektu pozwolą na dalsze badania nad przepływem kooperacyjnym w szerokim zakresie płynów, zarówno przezroczystych jak i nieprzezroczystych. Ponadto, wykazane kooperacyjne zachowanie FCD może być teraz wzięte pod uwagę przy ustalaniu warunków ciśnienia i temperatury podczas produkcji żywności.

Acknowledgements

In this section, I would like to express my huge gratitude to everyone who helped me to get to the point where I sometimes doubted myself would be able to get to: the end of the PhD. One thing I for sure learnt throughout the journey of the past 4 years is that it definitely takes a village to raise a doctor.

First of all, to my supervisors: thank you for all the time and energy that you have invested in my project and my development. **Camilla**, thank you for teaching me so much, about MR and about research, as well as for your exceptional attention to detail, thanks to which all my presentations were always top-notch. Thank you for making time to discuss science and non-science related topics. **Joshua**, thank you for all your soft matter support, your openness and your availability to discuss problems and solutions. I also have to thank you here for your punderful contributions to our meetings and emails. Your jokes brightened and loosened up any serious meeting. Lastly, **John**, thank you for guiding me through this process, for giving me the freedom to explore how to be an independent researcher, and for your trust. I have always enjoyed discussing science with you, and I have been inspired by the enthusiasm you show towards the work of your PhD students.

My time in BIP has also been accompanied by great office and groupmates, ever since I started. **Wouter** and **Raquel**, huge thanks to you both for forming the original, little NMR family. We not only survived, but also had some fun together during the times of corona. Additionally, Raquel, I am so grateful to you for all the mental and physical help you gave with the wobbles of the beginning of my PhD. **Mattia**, you were the best yoga student I've ever had. Thanks for all the dinners, bike rides, and games we played together. **Koen**, you were the greatest Nerf gun shooter and a role model for any PhD student. **Ahmad**, thank for being my first housemate in Wageningen. However, I will never forgive you for smashing my dice. **Rob**, it was always a pleasure to talk to you about hiking and yoga. **Netty**, thank you for making my start at BIP so smooth. **Tanya**, **Henk**, and **Donny**, thank you for great NMR and non-NMR related conversations. **Christo**, thank you for the organization of many nice lab activities. **Sasan**, thank you for introducing me to the real Turkish food.

During the years the group evolved, but days in office 3039 and in the coffee corner were never boring. **Ritje**, you have seen me through it all. Together, we celebrated the PhD related highs, and made sure the lows did not feel quite as low. Thank you for being my PhD sister, a wonderful paranymph, and a friend. **Sam**, thank you for all the walks around the building, filled with chats about work, music, guitars, and mandolins. **Dmytro**, **Maaïke**, and **Bariş**, thank you for the after-the-NMR-group-

meetings coffee breaks, and small uitjes. **Frank**, your in-depth NMR knowledge was absolutely priceless. Thank you for always being available to discuss NMR related matter, and for never making me feel like I was asking stupid questions. **John** (Philippi), thank you for all your technical support and expertise which were indispensable for the aims I had set out to complete in my project. **Yanzhang**, thank you for valuable tips on NMR measurements and jobs. To my desk neighbors, **Cleo** and **Keshav**, thanks for your ever present (forced) positivity. **Benjamin**, I really enjoyed all our conversations about doing a PhD, and other topics. Good luck with your next adventure, I hope the kiwi never gets you! **Peter** (Bos), thank you for awakening the running spirit of BIP. **Mariska, Suyeon, Tinko, Dana, Sonja, Abbas, Emilie, and Johannes**, I really enjoyed being a part of Patatje met Spin with you (and others)! **David, Lily, Martijn** (Gobes), and **Francesco**, thank you for making the participation in WeDay(s) so awesome and fun. I do think we need to practice the sausage jumping a bit more. **Lennart**, thank you for making each and every lunch break entertaining. I hope you never end up at HR. **Ian** and **Cor**, thank you for making sure that the lab runs smoothly. **Arjen**, thank you so much for all your help with the microscopy experiments. **Brenda**, thank you for always being very helpful and quick in answering any questions I had. **Jarne**, thanks for making sure we always have lunch on time. You can have my desk after I leave. **Annelies**, thank you for all the chats. I really enjoyed teaching and looking for flowers in de Veluwe with you. **Jeremy** and **Herbert**, thank you for always asking me nice questions during the BIP colloquia.

Big thanks to **Jasper** and all the colleagues from PCC for always making me feel welcome in the social events, group meetings, and in the lab. Special thanks to **Preeti, Akankshya, Zohreh, and Richard**, for making sure during the Dijkman group meetings that my knowledge in soft matter and rheology would not deteriorate. **Tom**, thank you for your help in preparation for this defense, and for your friendliness. **Remco** and **Raoul**, thank you for always being ready to help with any technical problems I came across in the rheology lab. **Julian** and **Riccardo**, thank you for all the climbing together.

I also would like to express my gratitude to all the people that contributed to my project and/or helped with the experiments. **Thomas** and **Dieter**, thank you for the great and informative meetings that we had during the four years. Your expert input was always very insightful and valued. **Gert-Jan** thank you for all our conversations in the NMR lab, I am very happy I could learn a few things from you. **Ruud** and **Peter** (de Groot), very big thank you for your friendly help with the preparation and characterization of my samples, even though it often came at times when you were

busy. **Julia**, it was always a nice surprise to bump into you in MAGNEFY. You were always ready to help with your expert NMR knowledge.

The journey of this PhD would have never started if it wasn't for the NMR methodology group in Manchester. **Laura, Ali, Ralph, Gareth** and **Mathias**, thank you for introducing me to the world of NMR.

The next portion of gratitude goes to my friends. **Vincent**, thank you for valuing my pseudo-scientific opinion on NMR related matter, I greatly enjoyed looking at and discussing your beautiful spectra. Also, thank you for your non-scientific input in my life. I'm looking forward to more via ferratas, MTBH, and whatever else comes. To the members of the Corona Squad. I could not imagine spending my free time of the four years of the PhD better than with you guys. You have kept me sane, I love you all. **Ludo, Ketan, Charlotte, Becky, Elien, Chandan, Corrie, Filip, Bea, Domi, Jody**, and **Mites**, thank you from the bottom of my heart for all the camping, cycling, partying, skiing, eating, non-wadlooping, sledging, and all other crazy activities. I look forward to all our future adventures together. Finally, **Martijn** (van Galen), apart from all the things mentioned above, I am so grateful you were always there for me. To celebrate success, to support me, to talk things through, come up with ideas, talk about experiments, science, and much, much more. **Joeri** and **Rolinde**, you both taught me what it means to truly share a home with somebody. From the first dinner you cooked for me, I've greatly appreciated your presence in my life. Moving into the G7 household was most likely the best decision I've made in the past couple of years. **Brend, Jan, Heleen, Clara, Anouk, Kylie, Katha**, and, of course, **Lloyd**, thank you so much for co-creating a home. I always know that after a hard day in the lab or elsewhere I can come home to a loving and fun atmosphere. **Ron**, thank you for your friendship, housemateship, hikership, paronymphship and all the other ships.

Na końcu chciałabym podziękować najważniejszym ludziom w moim życiu. **Mamo, tato**, bez was nic z tego by się nie wydarzyło. To, że tutaj zaszłam jest w ogromnej części waszą zasługą, i było możliwe dzięki waszej pomocy. Jestem wam na zawsze wdzięczna, że pomimo tego, że czasami nie zgadzacie się z moimi decyzjami, to zawsze mnie wspieracie i zawsze mogę na was liczyć. **Kuba**, dziękuję ci za to, że lubisz spędzać ze mną czas, i że możemy się razem dobrze bawić pomimo różnicy wieku. Jestem bardzo dumna z tego, na jakiego człowieka wyrastasz. Zawsze mnie zdumiewa twoja ciekawość świata, więc nigdy nie przestawaj zadawać mi pytań. Dziękuję też reszcie rodziny oraz przyjaciółom, za to, że zawsze mnie wspieracie, pomimo tego że mieszkam tak daleko od was.

Klaudia

About the author

Klaudia Milc was born on the 12th of May, 1995 in Kraków, Poland. She completed her education up until high school in Kraków. Subsequently, she moved to Manchester, UK to follow an integrated MSc program at the University of Manchester in Medicinal Chemistry. After completing an internship year at the Cancer Research Institute in Manchester, and a MSc thesis project, she earned a MChem degree (*cum laude*). Her MSc thesis project concerned the study of ^1H - ^1H residual dipolar couplings with selective NMR techniques, at the NMR methodology group, under the supervision of Dr. Laura Castañar, Dr. Mohammadali Foroozandeh, and Dr. Ralph Adams.



In August 2019, Klaudia moved to the Netherlands to start her PhD project at the laboratory of Biophysics at Wageningen University. Under the supervision of Dr. Camilla Terenzi, Dr. Joshua Dijkman and Prof. Dr. John van Duynhoven she studied the flow of complex fluids in sub-mm confinements with rheo-MRI. The results of the project are presented in this dissertation.

List of publications

Milc, K. W.; Serial, M. R.; Philippi, J.; Dijkstra, J. A.; van Duynhoven, J. P. M.; Terenzi, C. Validation of temperature-controlled rheo-MRI measurements in a submillimeter-gap Couette geometry, *Magn. Reson. Chem.* **2022**, *60* (7), 606-614.

Milc, K. W.; Dijkstra, J. A.; van Duynhoven, J. P. M.; Terenzi, C. Quantifying cooperative flow of fat crystal dispersions, *Soft Matter* **2022**, *18* (14), 2782-2789.

Milc, K. W.; Oerther, T.; Dijkstra, J. A.; van Duynhoven, J. P. M.; Terenzi, C. Capillary flow-MRI: quantifying micron-scale cooperativity in complex dispersions, *Anal. Chem.* **2023**, *95* (41), 15162-15170.

Overview of completed training activities

Discipline specific activities	Organizing institute	Year
Rheology: The do's and don'ts	VLAG	2019
Microfluidics course	J.M. Burgerscentrum	2021
MRFood workshop	University of Aarhus	2021
NMR-DG	Dow Terneuzen	2019
NMR-DG	TU Delft	2021
NMR-DG	Shell, Amsterdam	2022
Dutch biophysics	NWO	2020
Physics @Veldhoven	NWO	2021
Annual European Rheology Conference	ESR	2021
MRFood workshop	University of Aarhus	2021
MRFood	University of Aarhus	2022
New Frontiers in Liquid Matter	CECAM	2022
Euomar	Utrecht University	2022
General courses		
VLAG PhD week	VLAG	2019
Scientific writing	WGS,	2020
Programming in Python	Casimir graduate school, Delft	2021
Teaching lab practicals	Education Support Centre, WUR	2022
Career perspectives	WGS	2023
Optionals		
Preparation of research proposal	BIP	2019
Weekly group meetings	BIP	2019-2023
Weekly group meetings	PCC	2019-2023
BioNanoPhysX club	VLAG	2022-2023

Colophon

Research presented in this thesis was performed at the Laboratory of Biophysics, Wageningen University & Research, The Netherlands, and at Physical Chemistry and Soft Matter, Wageningen University & Research, The Netherlands. This work received financial support from Bruker BioSpin GmbH, Ettlingen, Germany.

Financial support from the Laboratory of Biophysics, Wageningen University, for printing this thesis is gratefully acknowledged.

Cover design by Lucile Michels and the author.

Printed by ProefschriftMaken.nl on FSC-certified paper.

Klaudia Milc, 2023

